Theoretical Study on Relationship between Open-Shell Electronic State and Electron Conductivity of Single Molecules and Their Aggregates toward Applications to Molecular Devices

Naoka AMAMIZU

MARCH 2025

Theoretical Study on Relationship between Open-Shell Electronic State and Electron Conductivity of Single Molecules and Their Aggregates toward Applications to Molecular Devices

A dissertation submitted to
THE GRADUATE SCHOOL OF ENGINEERING SCIENCE
OSAKA UNIVERSITY
in partial fulfillment of the requirements for the degree of
DOCTOR OF PHILOSOPHY IN SCIENCE

BY

Naoka AMAMIZU

MARCH 2025

Abstract

In this dissertation work, relationships between open-shell electronic states and electron conductivities of single molecules and their aggregates is investigated through simulations based on quantum chemical theory and condensed matter physics theory toward applications to molecular devices. The dissertation is composed of four parts. In Part I, the theoretical foundation of quantum chemical calculations, focusing on density functional theory methods for periodic systems with localized spins is introduced. In addition, the theory of quantum transport, electron conductivity in single molecule is explained, and the calculation methods for magnetic interactions and an advanced method for optimizing molecular structures with corrected spin states are also described. In Part II, single-molecule electron conductivities of open-shell single molecules are examined, and relationships between the electron conductivities, molecular structures and spin states are investigated aiming to establish design guidelines for single-molecule transistors. In Part III, molecular parallel circuit models composed of two single-molecule components are considered as the first step of the aggregates of the single-molecule components. By clarifying the relationship between structure, electronic states, and electron conductivity, a guideline for quantum interference control utilizing open-shell characters is established. In Part IV, as an investigation of more aggregation of the single molecules, crystalline materials with periodic structures are focused. A relationship between spin states and electron conductivity is clarified by using first-principles band calculations. As a result of these studies, this dissertation elucidates the relationship between spin-state control enabled by open-shell electronic states and electron conductivity, spanning from single molecules to their aggregates. Therefore, this dissertation provides design guidelines for single-molecule components utilizing open-shell electronic states and offers fundamental insights into theoretical and material design guidelines for molecular devices leveraging open-shell properties.

Preface

With the advancement of semiconductor miniaturization technology reaching the molecular scale, molecular electronics, which utilizes individual molecules as electronic components, has garnered increasing attention. While proposals for single-molecule components and molecular devices are being made, fundamental laws similar to Ohm's law have not been established in molecular electronics. Consequently, a systematic design approach, spanning from single-molecule components to molecular circuits and ultimately to molecular devices, has not been fully developed to clarify these fundamental principles. In such molecular-scale electronic conduction, quantum effects emerge, making it essential to understand the system based on the quantum chemical theory. Therefore, from the perspective of theoretical chemistry, it is desirable to elucidate the electron conduction mechanisms in molecular devices, propose design guidelines, and establish principles for functional control.

In this dissertation, I aimed to establish guidelines for designing and controlling the electron conductivity of single molecules and their aggregates for applications in molecular devices. As a functional indicator, I focused on open-shell electronic states. The open-shell electronic states have been reported to influence a molecule's magnetism and electron conductivity, making it possible to design functional molecules based on the open-shell electronic states. Therefore, I investigated relationships between the open-shell electronic states and electron conductivity, from single molecules to their aggregates, toward applications in molecular devices. This dissertation works will provide the fundamental insights into theoretical and material design guidelines for molecular devices leveraging open-shell properties.

This dissertation study was carried out under the supervision of Prof. Dr. Masayoshi Nakano, Prof. Dr. Norikazu Nishiyama and Prof. Dr. Yasutaka Kitagawa at Division of Chemical Engineering. Department of Materials Engineering Science, Graduate School of Engineering Science, Osaka University from April 2019 to March 2025. I dedicate this dissertation to late Prof. Dr. Masayoshi Nakano.

Naoka AMAMIZU
Division of Chemical Engineering Science
Department of Materials Engineering Science
Graduate School of Engineering Science, Osaka University

Contents

General Introduction

1. Open-shell systems

Open-shell nature expresses the instability of chemical bond, and is often explained by using the dissociation model of a hydrogen molecule, as shown in Fig. 1.1 [1,2]. When two hydrogen atoms are sufficiently close, they share electrons to form a covalent bond, resulting in the formation of a hydrogen molecule. In this case, the system is called a closed-shell system (Region I in Fig. 1.1). On the other hand, as the distance between the hydrogen atoms increases, the electrons gradually localize on each atom. At sufficiently long distances, the system transitions into two independent hydrogen atoms that have no chemical bond. Such a state is referred to as a pure open-shell system, which can be described as a system where localized spins exist on each atom of the molecule (Region III in Fig. 1.1). Organic radicals and transition metal complexes, which have localized spins, are typical examples of open-shell systems. For example of the open-shell system, organic diradical molecules have been attracted attention for a long time because of their unique properties and physical properties [3-5].

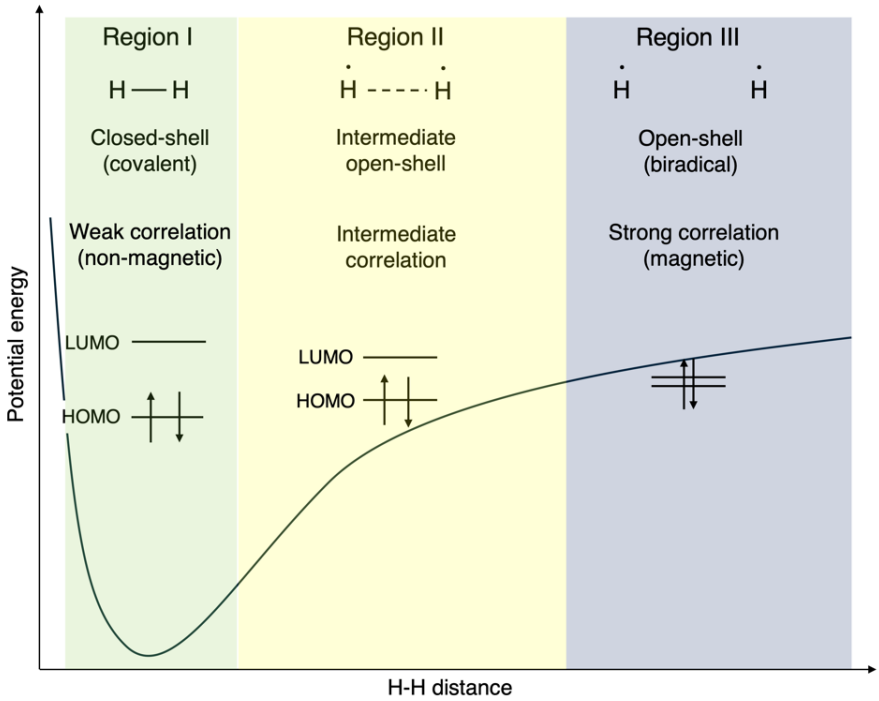

Fig. 1.1. The potential energy curve of H_2 along the H-H distance, and classification of the closed-shell and open-shell systems [2,6,7].

One of the oldest examples of organic diradical molecules is the hydrocarbon of Thiele [8] and Chichibabin [9] as shown in Fig. 1.2 (a) and (b), respectively. The open-shell nature can be explained by their resonance structure. According to Clar's six-membered ring rule, the stability of the system depends on the number of six-membered ring (benzoid) structures determined by aromatic stabilization because the aromatic stabilization energy due to the six-membered ring structure is expected to compensate for some of the destabilization energy due to π bond cleavage [10]. Therefore, in the Thiele's and Chichibabin's hydrocarbons, the open-shell diradical structures are more stable than the closed-shell quinoid structures because there are more six-membered rings in the diradical forms, and they are expected to exhibit the open-shell nature. However, since the two unpaired electrons in these hydrocarbons slightly interact, the closed-shell structures have a non-negligible contribution to their resonance structures. Thus, they are classified as intermediate open-shell molecules rather than pure open-shell molecules (Region II in Fig. 1.1).

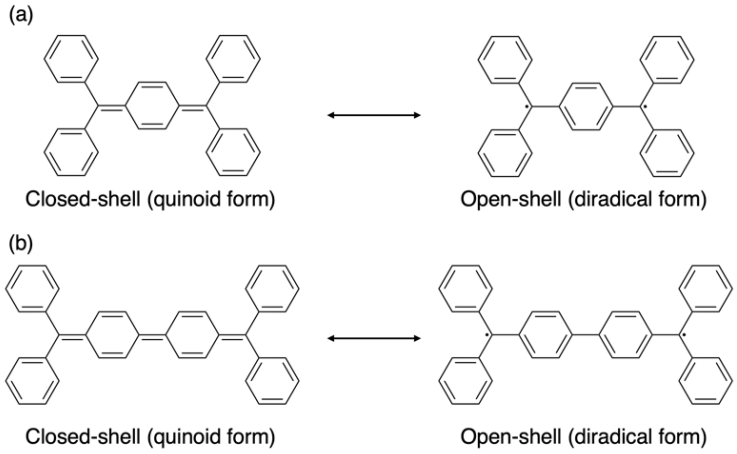

Fig. 1.2. The hydrocarbons of (a) Thiele and (b) Chichibabin. Both hydrocarbons show the closed-shell quinoid structures on the left side and the open-shell diradical structures on the right side.

In order to elucidate the nature and physical properties of diradical molecules, it is important to define a characteristic quantity of the open-shell nature within Regions I-III. As the representative feature, a diradical character was proposed by Hayes and Siu with a definition as the contribution of two-electron excited states [11]. In their definition, the value of the diradical character is 0 for closed-shell structure and 1 for open-shell structure, with values representing the open-shell states. While this parameter explicitly characterizes the open-shell nature, it has the drawback that the computational cost of the two-electron excited configuration is very high. Another parameter for evaluating diradical character is the occupation numbers of natural orbitals. The natural orbitals are defined as the eigenfunctions of the density matrix [12-14], and their occupation numbers n represent the number of

electrons occupying each orbital. The value of n is 0 or 2 for the closed-shell systems, but it falls within the range $0 < n < 2$ for the open-shell or diradical states. Therefore, it can be used as an indicator of open-shell character [15,16]. Takatsuka et al. and Head-Gordon have defined odd electrons based on the natural orbitals, which provide the number of the unpaired electrons and their spatial distributions [17,18]. Nakano et al. have proposed the multiple diradical characters based on the occupation number of the natural orbitals and the odd electrons, and clarified a relationship between the diradical characters and optical properties of the open-shell molecules [19-23]. Especially, regarding nonlinear optical materials, a correlation between the diradical characters and the second hyperpolarizability, which provides nonlinear optical response properties, has been identified [24,25]. The correlation has been revealed that the second hyperpolarizability reaches its maximum value in the region exhibiting intermediate open-shell states. In this way, research on the open-shell systems have been conducted over a long period, enabling the proposal of material design guidelines based on the open-shell properties.

In the field of condensed matter physics, the open-shell characters are also explained by electron correlation [28-28]. Usually, molecules possess a finite HOMO-LUMO gap. On the other hand, in bulk systems consisting of an infinite number of atoms, the orbitals form continuous bands, creating a band gap that is smaller than the HOMO-LUMO gap of typical molecules. As the molecular size increases, the HOMO-LUMO gap decreases, and the frontier orbitals begin to exhibit quasi-degeneracy. This trend becomes particularly pronounced in multinuclear metal complexes and metal nanoclusters, where multiple metal atoms with d-orbitals are aggregated (see Fig. 1.3) [29]. Such systems are referred to as strongly correlated systems, which result in localized electrons on metal ions and give rise to magnetism arising from various spin states [30]. In Fig. 1.1, each region is explained by the electron correlation: Region I represents the weak correlated systems, Region II denotes the intermediate correlated systems, Region III denotes the strong correlated systems.

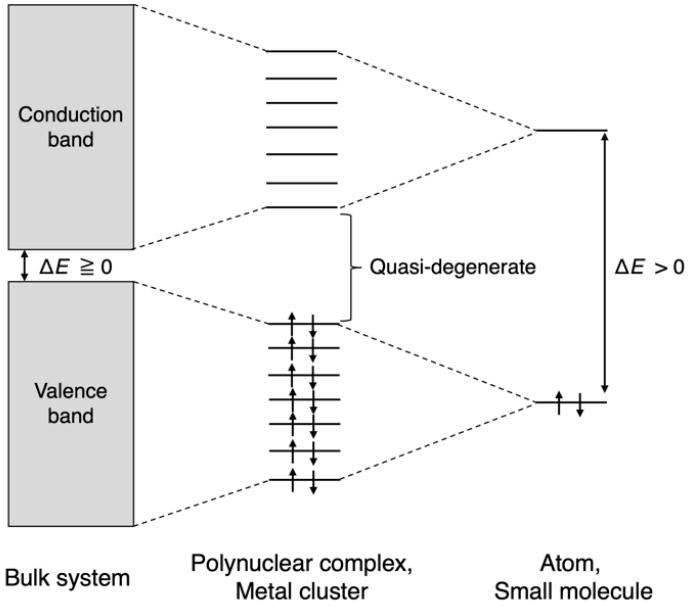

Fig. 1.3. Illustration of the electronic structures in (a) Bulk system, (b) polynuclear complex, metal cluster, (c) atom and small molecule [29].

In the viewpoint of quantum chemical calculations, the open-shell systems, especially strongly correlated systems, are highly challenging subject to calculate the electronic structure. For instance, as explained in the example of the hydrogen molecule in Fig. 1.1, the HOMO-LUMO gap is sufficiently large in the closed-shell system, and the wavefunction of the hydrogen molecule can be approximated solely by the ground state electron configuration, where two electrons occupy the bonding orbital (HOMO). In the case of the open-shell systems, the HOMO-LUMO gap competes with the Coulomb repulsion between the two electrons since the HOMO and LUMO are quasi-degenerate. It makes the contribution of the excited configuration (two electrons occupy the LUMO) non-negligible. As a result, even in the ground state, it becomes necessary to incorporate both the ground and excited configurations. Consequently, the wavefunction must be expressed as a linear combination of multiple determinants.

When the wavefunction is described using multiple Slater determinants, an accurate depiction requires a linear combination of all possible configurations. This method is called the configuration interaction (CI) method. Since it involves a vast number of configurations, however, the computational cost becomes prohibitively high, making it impractical for anything other than simple molecules. To address this, the complete active space (CAS) CI method that only the quasi-degenerate orbitals are selected for applying the CI approach, is proposed. The complete active space self-consistent field (CASSCF) method, in which the orbital coefficients of each determinant are also optimized, is often used for the practical use [31]. Thus, the electronic state calculations of strongly correlated systems are challenging to handle, especially for the theoretical calculations of metal-metal bonding and their

magnetism using CASSCF and its advanced methods such as CASPT2 proposed by Roos, Gagliardi, McGrady and so on [32-36]. On the other hand, in multinuclear metal complexes, the number of d-orbitals to be considered becomes significantly large, resulting in a substantial computational cost even with the CAS method. To address this, calculation methods using the broken-symmetry (BS) approach, which represents the system with a single determinant without strictly satisfying spin symmetry, have also been proposed [37-39]. The details of this method are explained in Part I Chapter 3. The BS method, combined with the spin contamination error, has enabled the treatment of multinuclear metal complexes at a lower computational cost. Furthermore, it has facilitated the analysis of the magnetic properties of multinuclear metal complexes [40]. In addition, in multinuclear metal complexes, it has been revealed that changes in spin states affect electrical conductivity, with the spin-excited state exhibiting higher electrical conductivity compared to the spin-ground state [41-43].

As described above, unique optical, magnetic, and electron conductive properties based on open-shell systems emerge, enabling their application to functional materials and the development of design guidelines.

2. Molecular electronics

Microfabrication technology for integrated circuits has been developed according to Moore's law proposed in 1965 [44,45]. Fig. 2.1 illustrates the year-by-year changes in the process size, an index of the miniaturization of transistors [46]. The process size has been decreasing over the past 30 years, and this miniaturization of transistors has increased integration density, which drastically improves the performance of electron devices. On the other hand, it has been suggested that the miniaturization of silicon (Si)-based devices is almost reaching its limit. Table 2.1 shows technology advancements, change in the transistor process size and gate length [47]. Since the development of the complementary metal oxide semiconductor (CMOS) technology around 1990, the introduction of high-κ films with high dielectric constants has dramatically miniaturized transistor sizes. The "International Technology Roadmap for Semiconductors (ITRS) 2015" predicted that Moore's Law would come to an end by 2021 [48], however some advancements in technology such as FinFET (a three-dimensional (3D) stacked transistor technology introduced in 2011 beyond the traditional planar technology) and extreme ultraviolet (EUV) lithography (implemented in 2019) have brought further miniaturization of process sizes. The "International Roadmap for Devices and Systems (IRDS)" released by IEEE has reported that the reduction in process size with current mainstream technologies by the FinFET is expected to saturate by 2028, leading to a transition towards new manufacturing technologies, such as 3D structures [49]. In the future, a miniaturization beyond 2nm is expected to be achieved using a technology called Gate-All-Around (GAA), which arranges conductive channel regions in the 3D structure.

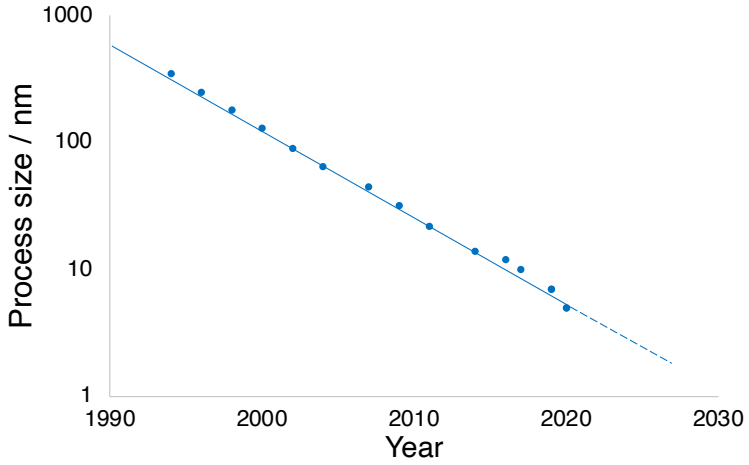

Fig. 2.1. Year-by-year changes in process size of transistors [46,47].

Table 2.1. Technological advancements and changes in transistor process size.

Year	Process size / nm	Gate length / nm	Technological advancements
1990	800	800	Early CMOS processes
1995	350	350	Improved power efficiency, early scaling effects
2000	180	180	Increased integration, introduction of Cu wiring
2004	90	50	Exploration of high-κ dielectric and metal gate technology
2007	45	35	Practical use of high-κ/metal gate technology
2011	22	25	Introduction of FinFET (3D transistor)
2014	14	20	Improved FinFET, enhanced performance, reduced power consumption
2017	10	18 ~ 20	Higher transistor density, approaching scaling limits
2019	7		Practical use of EUV (Extreme Ultraviolet) lithography
2022	5	15 ~ 18	Mainstream for high-performance chips, further integration
2024	3	10 ~ 14	Start of mass production, transition to next-gen chip technologies
Forecast	< 2	< 10	Advancement of 3D structures, adoption of GAA (Gate-All-Around)

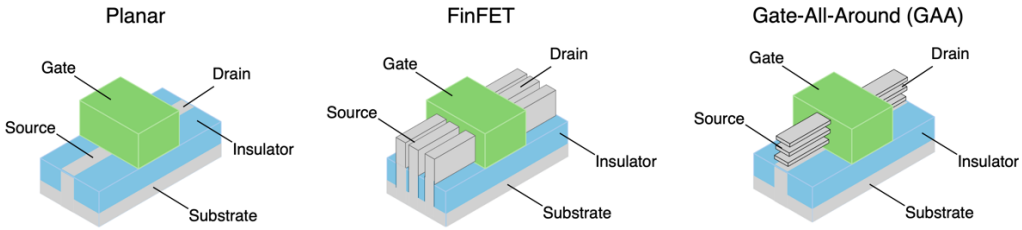

Fig. 2.2. Schematic diagram of planar, FinFET and GAA.

As the miniaturization technology for semiconductors have developed, various problems associated with the miniaturization of Si-based transistors have become difficult to ignore. For example, the miniaturized semiconductors face problems such as increased complexity in processing, variability in size and the non-uniform distribution of impurity atoms doped into the semiconductor. Additionally, as insulating films become excessively thin, tunneling currents can no longer be ignored because of leakage currents and significant energy losses. Furthermore, the lithography technologies for further miniaturization would require a light irradiation with wavelengths shorter than those of EUV (< 13.5 nm), posing another critical issue.

In the current FinFET technology, the smallest dimension has reached 5 nm. As the Si-based semiconductor miniaturization has approached the molecular scale and faced the aforementioned scaling limits, molecular electronics has attracted much attention as a new class of nanomaterials [50-55]. The molecular electronics is aimed to use functional single-molecules for the electronic components, such as wires (resistors), transistors, diodes and so on. In 1956, von Hippel was proposed the first concept of assembling electronic devices from atoms or molecules in a bottom-up approach [56]. The current attention on the molecular electronics has originated from the theoretical proposal of a single-molecule diode by Aviram and Ratner in 1974. [57]. Fig. 2.3 shows the concept of the single-molecule diode proposed by Aviram and Ratner. They considered that a connection an electron acceptor i.e. tetracyanoquinodimethane (TCNQ) and an electron donor i.e. tetrathiafulvalene (TTF) via a σ-bond through an insulating region would enable a unidirectional electron transport within the single-molecule (see Fig. 2.3 (a) and (b)). When a forward bias voltage is applied as shown in Fig. 2.3 (c), electron transfer occurs from Electrode I to TCNQ if the HOMO level of Electrode I becomes higher than the LUMO of TCNQ. Similarly, if the LUMO level of Electrode II becomes lower than the HOMO of TTF, electron transfer occurs from TTF to Electrode II. Due to this insulation, the electron transfer from TCNQ to TTF during the process becomes irreversible. On the other hand, in the case of a reverse bias voltage, as shown in Fig. 2.3 (d), due to the energy level relationship, a significantly high bias voltage is required for electron transfer from the HOMO of Electrode II to the LUMO of TTF, as well as from the HOMO of TCNQ to the LUMO of Electrode I. Therefore, it was considered that this molecule shows functionality as a rectifier, allowing electron transfer only in the direction from TCNQ to TTF under forward bias. The rectification of such an Acceptor-σ/bonds-

Donor structure was experimentally demonstrated by Geddes et al. in 1990 [58]. Even today, the asymmetric connection of acceptor and donor units remains a fundamental design guideline for single-molecule diodes [59-63].

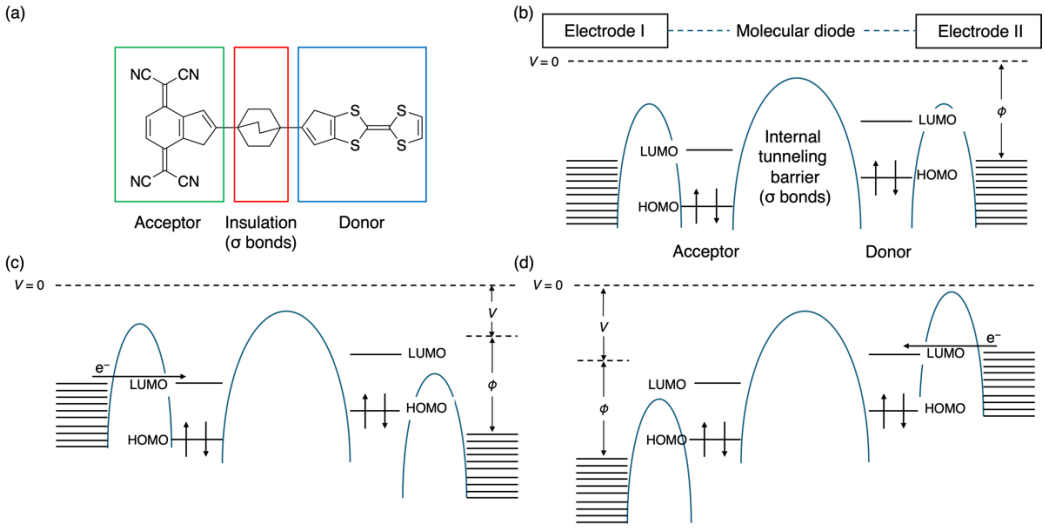

Fig. 2.3. (a) Single-molecule diode proposed by Aviram and Ratner, and schematic energy diagram of the rectification mechanism: (b) no bias , (c) forward bias from Electrode I to Electrode II and (d) Reverse bias from Electrode II to Electrode I.

After the proposal of the molecular rectifier, the scanning tunneling microscopy (STM) was developed. The development of STM has enabled the manipulation of individual atoms [64,65]. In addition, electron transport theories and computational methods for the nanoscale materials have also been developed. Fischetti and co-workers proposed a calculation method for electron transport in nanoscale semiconductors using semiclassical approximations with Monte Carlo methods [66]. Additionally, Mujica et al. formulated the electrical conduction in single molecules based on the elastic scattering Green's function method [67,68]. Until the early 1990s, the foundational methodologies of the field had been not established yet although the many research had focused on applications of the nanomaterials.

A significant breakthrough in molecular electronics was the development of single-molecule electron conductivity measurement techniques. Reed et al. proposed the mechanically controllable break junction (MC-BJ) method and measured the current-voltage characteristics of 1,4-benzene dithiol [69]. Fig. 2.4 illustrates a procedure of the MC-BJ method. First, a self-assembled monolayer (SAM) of 1,4-benzene dithiol is formed on the surface of the gold wire (Fig. 2.4 I→II) by immersing a gold wire into a tetrahydrofuran (THF) solution of 1,4-benzene dithiol. Next, the gold wire is pushed until it breaks by the pushing rod (Fig. 2.4 III). After evaporating the solvent, the rod is retracted, followed by the measurement of the current through the 1,4-benzene dithiol molecule, which bridges

the gold wire (electrodes) (Fig. 2.4 IV). By repeating the operations in Fig. 2.4 III and IV multiple times, the statistical electron conductivity of a single molecule can be determined. The MC-BJ method has enabled the measurement of the conductance of even hydrogen molecules [70]. Another method of the measurement of single-molecule electron conductivity is the scanning tunneling microscope break junction (STM-BJ) method proposed by Tao et al. [71]. In this method, the STM tip is brought into contact with the metal substrate surface to form a metallic nanojunction. Once the sufficient contact is confirmed, the tip is gradually retracted to break the junction. By adsorbing the target molecules onto the electrode surface through solution or deposition methods, the molecule bridges the nanogap during the retraction process. A voltage is then applied to measure the current through the bridged molecule (see Fig. 2.5). By repeatedly forming/breaking nanogaps and bridging molecules, the electrical conductivity of molecules can be statistically measured. This method has become the mainstream technique for single-molecule electron conductivity measurements due to its ease of repeated measurements, high reproducibility, and adaptability to a wide range of molecules. Along with the development of techniques for measuring single-molecule electrical conductivity, theoretical prediction methods have also advanced by the proposals of electron transport theories based on Green's functions combined with quantum chemical calculations (The detail is provided in Part I Chapter 2) [72-77].

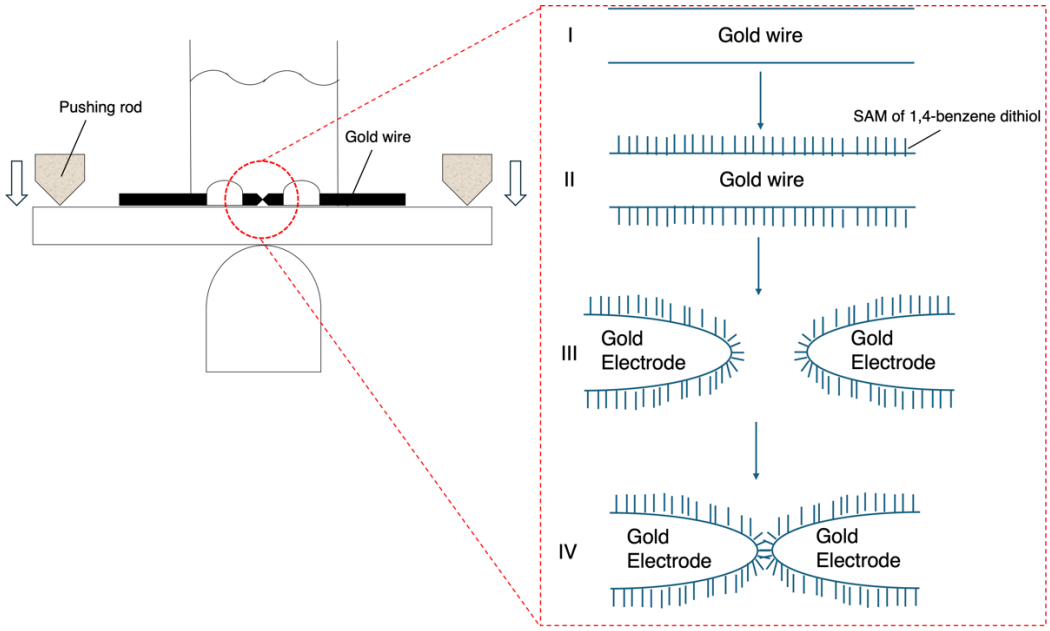

Fig. 2.4. Illustration of MC-BJ method. I: Initial state of gold wire, II: Immersing a gold wire into tetrahydrofuran (THF) solution of 1,4-benzene dithiol, and the self-assembled monolayer (SAM) of 1,4-benzene dithiol forms on the surface of the gold wire, III: Pressing the pushing rod until gold wire breaks, and IV: Relaxing the rod and bridging the molecules between the gold wire electrodes.

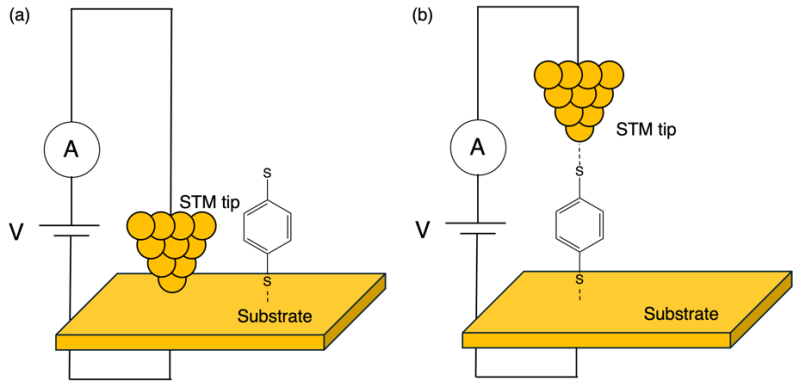

Fig. 2.5. Illustration of STM-BJ method. (a) STM tip contacts with the metal substrate, and (b) the molecule bridges between the STM tip and the substrate.

Since the techniques for measurements and calculations of single-molecule electron conductivity were developed, a variety of functional single-molecule components like the single-molecule diodes (rectifiers) have been proposed. The simplest single-molecule components are called molecular wires, which connects between individual components and serve as resistors [78-81]. Molecular wires have also been used to evaluate the fundamental properties of single-molecule devices. For example, it has been investigated that conductivity decays exponentially with molecular chain length [82]. Based on this guideline, researches have been made to design molecular wires with extremely low decay rates relative to chain length [83,84]. Single-molecule transistors or switches utilize two states with different electron conductivity, and define the high-conductivity state as ON and the low-conductivity state as OFF. The switching is generally achieved using spin state transitions [42,43,85], structural changes [86,87] and redox state changes [88] controlled by external stimuli. Moreover, single-molecule transistors utilizing gate modulation with a three-terminal configuration have also been proposed [89]. Furthermore, it becomes possible to realize logic operations by using single-molecule components [90-94]. These devices have been proposed for use as logic operation elements, utilizing the fact that the molecular structure and electronic state can vary depending on multiple external stimuli or the intensity of input signals.

For the practical application of these single-molecule components as molecular devices, the next essential step is their integration. Recently, for example, integrated single-molecule components based on self-assembled monolayers (SAMs) have been proposed and have shown a variety of functionalities [95-97]. Research toward the molecular devices has also proposed integrating hundreds to thousands of single-molecule devices on a semiconductor chip to develop applications such as biosensors that detect interactions between single-molecule devices and external molecules like gases [98]. In addition, it has suggested an application of the nonlinear electrical signals of aggregated molecules derived from molecular tunneling conduction to neuromorphic computing, because this phenomenon is similar to electrical signals of human brain [99,100].

While the molecular electronics continues to advance, design guidelines indicating which materials are best suited for single-molecule components have not to be established yet. In addition, in systems where single-molecule components are integrated, fundamental insights into the electron conduction properties when these molecules are interconnected remain largely unknown. In this way, the theoretical design and material design principles for these molecular devices remain unclear, and fundamental insights have been scarcely studied.

3. Outline of this dissertation

This dissertation is composed of four parts. Part I provides the general theory for quantum chemical calculations (Chapter 1), electron transport for single molecule (Chapter 2) and Estimation of molecular magnetism and correction of spin contamination (Chapter 3).

In Part II, the author examined to utilize the open-shell properties for single-molecule components. In particular, the author focused on the structural and spin state changes of metal complexes with open-shell electronic states and their effect on the single-molecule electron conductivity.

In Part III and IV, the author explored the aggregates of single-molecule components. In Part III, the author considered a molecular parallel circuit model composed of two single-molecule components as a simple integrated system, and the author investigated the relationship between its electronic state and electron conductivity. In Part IV, the author extended the investigation to molecular crystalline models with periodic structures and examine the relationship between spin states and electron conductivity.

This dissertation work clarifies the relationship between open-shell electronic state and electron conductivity, from single-molecule components to their aggregate models. These results will not only provide design guidelines based on open-shell electronic states in single-molecule components but also contribute to the development of advanced molecular device designs and the establishment of fundamental knowledge.

References

1. A. Szabo, N. S. Ostlund, *MODERN QUANTUM CHEMISTRY: Introduction to Advanced Electron Structure Theory*, Reprint, Dover Publications, Mineola, New York, 1996.
2. Y. Yoshioka, D. Yamaki, G. Maruta, T. Tsunesada, K. Takada, T. Noro, K. Yamaguchi, *Bull. Chem. Soc. Jpn*. **1996**, *69*, 3395.
3. L. Salem, C. Rowland, *Angew. Chem. Int. Ed.*, **1972**, *11*, 92.
4. M. Abe, Diradicals, *Chem. Rev.*, **2013**, *113*, 7011.
5. T. Stuyver, B. Chen, T. Zeng, P. Geerlings, F. D. Proft, R. Hoffmann, *Chem. Rev.*, **2019**, *119*, 11291.
6. M. Nakano, *Excitation Energies and Properties of Open-Shell Singlet Molecules*, Springer

International Publishing, Cham, 2014.
7. M. Nakano, *Top Curr Chem (Z)*, **2017**, *375*, 47.
8. J. Thiele, H. Balhorn, *Chem. Ber.*, **1904**, *37*, 1463.
9. A. E. Chichibabin, *Chem. Ber.*, **1907**, *40*, 1810.
10. E. Clar, *The Aromatic Sextet*, Wiley, New York, 1972.
11. E. F. Hayes, A. K. Q. Siu, *J. Am. Chem. Soc.* **1971**, *93*, 2090.
12. P.-O. Löwdin, *Phys. Rev.*, **1955**, *97*, 1474.
13. P.-O. Löwdin, *Phys. Rev.*, **1955**, *97*, 1490.
14. P.-O. Löwdin, *Phys. Rev.*, **1955**, *97*, 1509.
15. K. Yamaguchi, *Chem. Phys. Lett.*, **1975**, *33*, 330
16. D. Doehnert, J. Koutecky, *J. Am. Chem. Soc.*, **1980**, *102*, 1789.
17. K. Takatsuka, T. Fueno, K. Yamaguchi, *Theoret. Chim. Acta*, **1978**, *48*, 175.
18. M. Head-Gordon, *Chem. Phys. Lett.* **2003**, *372*, 508.
19. M. Nakano, R. Kishi, T. Nitta, T. Kubo, K. Nakasuji, K. Kamada, K. Ohta, B. Champagne, E. Botek, K. Yamaguchi, *J. Phys. Chem. A*, **2005**, *109*, 885.
20. M. Nakano, R. Kishi, S. Ohta, H. Takahashi, T. Kubo, K. Kamada, K. Ohta, E. Botek, B. Champagne, *Phys. Rev. Lett.*, **2007**, *99*, 033001.
21. S. Ohta, M. Nakano, T. Kubo, K. Kamada, K. Ohta, R. Kishi, N. Nakagawa, B. Champagne, E. Botek, A. Takebe, S. Umezaki, M. Nate, H. Takahashi, S. Furukawa, Y. Morita, K. Nakasuji, K. Yamaguchi, *J. Phys. Chem. A*, **2007**, *111*, 3633.
22. M. Nakano, B. Champagne, E. Botek, K. Ohta, K. Kamada, T. Kubo, *J. Chem. Phys.*, **2010**, *133*, 154302.
23. M. Nakano, T. Minami, H. Fukui, R. Kishi, Y. Shigeta, B. Champagne, *J. Chem. Phys*., **2012**, *136*, 024315.
24. M. Nakano, B. Champagne, *J. Phys. Chem. Lett.*, **2015**, *6*, 3236.
25. M. Nakano, B. Champagne, *WIREs Comput Mol Sci*, **2016**, *6*, 198.
26. B. Coqblin, in *Electron Systems: Strong Correlations*, in E*ncyclopedia of Materials: Science and Technology*, K.H. J. Buschow, R. W. Cahn, M. C. Flemings, B. Ilschner, E. J. Kramer, S. Mahajan, P. Veyssière (Ed.), Pergamon Press, Oxford, 2001, pp. 2591-2603.
27. A. S. Edelstein, *J. Magn. Mag. Matter.*, **2003**, *256*, 430.
28. C. Zhou, M. R. Hermes, D. Wu, J. J. Bao, R. Pandharkar, D. S. King, D. Zhang, T. R. Scott, A. O. Lykhin, L. Gagliardi, D. G. Truhlar. *Chem Sci.*, **2022**, *13*, 7685.
29. Y. Kitagawa, T. Saito, K. Yamaguchi, *Bull. Jpn. Soc. Coord. Chem.*, **2018**, *71,* 57.
30. J. F. Berry, in *Multiple Bonds Between Metal Atoms*, F. A. Cotton, C. A. Murillo, R. A. Walton (Ed.), Springer Science and Business Media, Inc., New York, 3rd ed., 2005, pp. 669-706.
31. B. O. Roos, P. R. Taylor, P. E. M. Siegbahn, *Chem. Phys.*, **1980**, *48*, 157.

32. K. Andersson, C.W. Bauschlicher Jr., B. J. Persson, B. O. Roos, *Chem. Phys. Lett.*, **1996**, *257*, 238.
33. L. Gagliardi, B. O. Roos, *Inorg. Chem.*, **2003**, *42*, 1599.
34. G. L. Macchia, G. L. Manni, T. K. Todorova, M. Brynda, F. Aquilante, B. O. Roos, L. Gagliardi, *Inorg. Chem.*, **2010**, *49*, 5216.
35. D. A. Pantazis, J. E. McGrady, *J. Am. Chem. Soc.*, **2006**, *128*, 4128.
36. M. Spivak, V. Arcisauskaite, X. López, J. E. McGrady, C.de Graaf, *Dalton Trans.*, **2017**, *46*, 6202.
37. K. Yamaguchi, Y. Takahara, T. Fueno, K. N. Houk, *Theor. Chim. Acta*, **1988**, *73,* 337.
38. K. Yamaguchi, M. Okumura, W. Mori, J. Maki, K. Takada, T. Noro, K. Tanaka, *Chem. Phys. Lett.*, **1993**, *210*, 201.
39. S. Yamanaka, M. Okumura, M. Nakano, K. Yamaguchi, *J. Mol. Struct. (Theochem)*, **1994**, *310,* 205.
40. Y. Kitagawa, Y. Nakanishi, T. Saito, T. Kawakami, M. Okumura, K. Yamaguchi, *Int. J. Quantum Chem.*, **2009**, *109*, 3315.
41. Y. Kitagawa, T. Matsui, Y. Nakanishi, Y. Shigeta, T. Kawakami, M. Okumura, K. Yamaguchi, *Dalton Trans.*, **2013**, *42*, 16200.
42. Y. Kitagawa, M. Asaoka, Y. Natori, K. Miyagi, R. Teramoto, T. Matsui, Y. Shigeta, M. Okumura, M. Nakano, *Polyhedron*, **2017**, *136*, 125.
43. Y. Kitagawa, H. Tada, I. Era, T. Fujii, K. Ikenaga, M. Nakano, *Molecules*, **2019**, *24*, 1956.
44. G. E. Moore, *Electronics.*, **1965**, *38*, 114.
45. G. E. Moore, *IEDM Tech. Digest.*, **1975**, *21*, 11.
46. M. T. Bohr, I. A. Young, *IEEE Comput. Soc.*, **2017**, *37*, 20.
47. IEEE International Roadmap for Devices and Systems, "*Executive Summary 2022*." Institute of Electrical and Electronics Engineers, **2022.**
48. IEEE International Technology Roadmap for Semiconductors, "*Executive Report.*" Institute of Electrical and Electronics Engineers, **2015**.
49. IEEE International Roadmap for Devices and Systems, "*More Moore.*" Institute of Electrical and Electronics Engineers, **2023.**
50. R. L. Carroll, C. B. Gorman, *Angew. Chem. Int. Ed.*, **2002**, *41*, 4378.
51. C. Joachim, J. K. Gimzewski, A. Aviram, *Nature*., **2000**, *408*, 541.
52. S. V. Aradhya, L. Venkataraman, *Nat. Nanotech.*, **2013**, *8*, 399.
53. D. Xiang, X. Wang, C. Jia, T. Lee, X. Guo, *Chem. Rev.*, **2016**, *116*, 4318.
54. T. Li, V. K. Bandari, O. G. Schmidt, *Adv. Mater.*, **2023**, *35*, 2209088.
55. K. Ariga, *Bull. Chem. Soc. Jpn.*, **2024**, *97*, uoad001.
56. A. von Hippel, *Science*, **1956**, *123*, 315.
57. A. Aviram, M. A. Ratner, *Chem. Phys. Lett.*, **1974**, *29*, 277.

58. N. J. Geddes, J. R. Sambles, D. J. Jarvis, W. G. Parker, D. J. Sandman, *Appl. Phys. Lett*., **1990**, *56*, 1916.
59. M. Elbing, R. Ochs, M. Koentopp, M. Fischer, C. von Hänisch, F. Weigend, F. Evers, H. B. Weber, M. Mayor, *Proc. Natl. Acad. Sci. U.S.A*., **2005**, *102*, 8815.
60. I. Díez-Pérez, J. Hihath, Y. Lee, L. Yu, L. Adamska, M. A. Kozhushner, I. I. Oleynik, N. Tao, *Nat. Chem.*, **2009**, *1*, 635.
61. M. Handayani, S. Gohda, D. Tanaka, T. Ogawa, *Chem. Eur. J.*, **2014**, *20*, 7655.
62. B. Capozzi, J. Xia, O. Adak, E. J. Dell, Z.-F. Liu, J. C. Taylor, J. B. Neaton, L. M. Campos, L. Venkataraman, *Nat. Nanotechnol.*, **2015**, *10*, 522.
63. M. Li, H. Fu, B. Wang, J. Cheng, W. Hu, B. Yin, P. Peng, S. Zhou, X. Gao, C. Jia, X. Guo, *J. Am. Chem. Soc.*, **2022**, *144*, 20797.
64. G. Binnig, H. Rohrer, Ch. Gerber, E. Weibel, *Phys. Rev. Lett.*, **1982**, *49*, 57.
65. D. M. Eigler, E. K. Schweize, *Nature*, **1990**, *344*, 524.
66. M. V. Fischetti, S. E. Laux, *Phys. Rev. B*, **1988**, *38*, 9721.
67. V. Mujica, M. Kemp, M. A. Ratner, *J. Chem. Phys.*, **1994**, *101*, 6849.
68. V. Mujica, M. Kemp, M. A. Ratner, *J. Chem. Phys.*, **1994**, *101*, 6856.
69. M. A. Reed, C. Zhou, C. J. Muller, T. P. Burgin, J. M. Tour, *Science*., **1997**, *278*, 252.
70. R. H. M. Smit, Y. Noat, C. Untiedt, N. D. Lang, M. C. van Hemert, J. M. van Ruitenbeek, *Nature*., **2002**, *419*, 906.
71. B. Xu, N. J. Tao, *Science*., **2003**, *301*, 1221.
72. M. D. Ventra, S. T. Pantelides, N. D. Lang, *Phys. Rev. Lett.*, **2000**, *84*, 979.
73. Y. Xue, S. Datta, M. A. Ratner, *Chem. Phys.*, **2002**, *281*, 151.
74. M. Brandbyge, J.-L. Mozos, P. Ordejón, J. Taylor, K. Stokbro, *Phys. Rev. B.*, **2002**, *65*, 165401.
75. Y. Luo, C.-K. Wang, Y. Fu, *J. Chem. Phys.*, **2002**, *117*, 10283.
76. T. Tada, M. Kondo, K. Yoshizawa, *J. Chem. Phys.*, **2004**, *121*, 8050.
77. L.-Y. Hsu, Q.-R. Huang, B.-Y. Jin, *J. Phys. Chem. C.*, **2008**, *112*, 10538.
78. R. Yamada, H. Kumazawa, T. Noutoshi, S. Tanaka, H. Tada, *Nano Lett.*, **2008**, *8*, 1237.
79. J. Sukegawa, C. Schubert, X. Zhu, H. Tsuji, D. M. Guldi, E. Nakamura, *Nat. Chem.*, **2014**, *6,* 899.
80. Y. Tanaka, Y. Kato, K. Sugimoto, R. Kawano, T. Tada, S. Fujii, M. Kiguchi, M. Akita, *Chem. Sci.*, **2021**, *12*, 4338.
81. T. Gao, C. He, C. Liu, Y. Fan, C. Zhao, C. Zhao, W. Su, Y. J. Dappe, L. Yang, *Phys. Chem. Chem. Phys.*, **2021**, *23*, 21163.
82. N. J. Tao, *Nat. Nanotech.,* **2006**, *1*, 173.
83. R. Sakamoto, S. Katagiri, H. Maeda, H. Nishihara, *Coord. Chem. Rev*., **2013**, *257*, 1493.
84. Y. Tanaka, Y. Kato, K. Sugimoto, R. Kawano, T. Tada, S. Fujii, M. Kiguchi, M. Akita, *Chem. Sci.*, **2021**, *12*, 4338.

85. E. Ruiz, *Phys. Chem. Chem. Phys.*, **2014**, *16*, 14.
86. K. Matsuda, H. Yamaguchi, T. Sakano, M. Ikeda, N. Tanifuji, M. Irie, *J. Chem. Phys. C,* **2008**, *112*, 17005.
87. C. Jia, A. Migliore, N. Xin, S. Huang, J. Wang, Q. Yang, S. Wang, H. Chen, D. Wang, B. Feng, Z. Liu, G. Zhang, D.-H. Qu, H. Tian, M. A. Ratner, H. Q. Xu, A. Nitzan, X. Guo, *Science*., **2016**, *352*, 1443.
88. J. Li, S. Pudar, H. Yu, S. Li, J. S. Moore, J. Rodríguez-López, N. E. Jackson, C. M. Schroeder, *J. Phys. Chem. C*, **2021**, *125*, 21862.
89. H. Song, Y. Kim, Y. H. Jang, H. Jeong, M. A. Reed, T. Lee, *Nature*, **2009**, *462*, 1039.
90. F. Meng, Y.-M. Hervault, Q. Shao, B. Hu, L. Norel, S. Rigaut, X. Chen, *Nat. Commun*., **2014**, *5*, 3023.
91. N. Zhang, W.-Y. Lo, A. Jose, Z. Cai, L. Li, L. Yu, *Adv. Mater.*, **2017,** 29, 1701248.
92. S. Cai, W. Deng, F. Huang, L. Chen, C. Tang, W. He, S. Long, R. Li, Z. Tan, J. Liu, J. Shi, Z. Liu, Z. Xiao, D. Zhang, W. Hong, *Angew. Chem. Int. Ed.*, **2019**, *58*, 3829.
93. W. Zhao, D. Zou, Z. Sun, Y. Xu, G. Ji, X. Li, C. Yang, *Adv. Theory Simul.*, **2020**, *3*, 2000163.
94. R. Liu, Y. Han, F. Sun, G. Khatri, J. Kwon, C. Nickle, L. Wang, C.-K. Wang, D. Thompson, Z.-L. Li, C. A. Nijhuis, E. del Barco, *Adv. Mater*., **2022**, *34*, 2202135.
95. X. Chen, M. Roemer, L. Yuan, W. Du, D. Thompson, E. del, C. A. Nijhuis, *Nat. Nanotech*., **2017**, *12*, 797.
96. Y. Han, C. Nickle, Z. Zhang, H. P. A. G. Astier, T. J. Duffin, D. Qi, Z. Wang, E. del Barco, D. Thompson, C. A. Nijhuis, *Nat. Mater.*, **2020**, *19*, 843.
97. G. D. Kong, H. Song, S. Yoon, H. Kang, R. Chang, H. J. Yoon, *Nano Lett.*, **2021**, *21*, 3162.
98. C. W. Fuller, P. S. Padayatti, H. Abderrahim, B. Merriman, et al., *Proc. Natl. Acad. Sci. U.S.A.*, **2022**, *119*, e2112812119.
99. Y. Hirano, Y. Segawa, T. Kawai, T. Matsumoto, *J. Phys. Chem. C.*, **2013**, *117*, 140.
100. H. Tanaka, M. Akai-Kasaya, A. TermehYousefi, L. Hong, L. Fu, H. Tamukoh, D. Tanaka, T. Asai, T. Ogawa, *Nat. Commun.*, **2018**, *9*, 2693.

Part I
General Theory

Chapter 1. Quantum chemical calculation

To theoretically predict the physical properties of materials, Schrödinger proposed a fundamental equation known as the Schrödinger equation. The solution to this equation, called the wavefunction, is understood to provide a complete quantum mechanical description of any system. For two-body problems such as the hydrogen atom, the Schrödinger equation can be solved exactly. However, for systems involving more than two bodies, it becomes impossible to solve the Schrödinger equation precisely. Hartree-Fock (HF) theory and density functional theory (DFT) calculation are the most familiar methods to solve the Schrödinger equation for many-body systems. In this section, the author describes the fundamentals of HF theory and DFT. In addition, the author discusses the DFT calculation for the periodic systems.

1.1 Hartree-Fock theory

Hartree-Fock (HF) theory is a representative approximation method in modern quantum chemistry. Based on the HF theory, various methods have been developed, enabling the calculation of molecular physical properties through computational approaches using appropriate methods. In this section, the key results obtained from the derivation of the HF equations are presented [1].

1.1.1 Hartree-Fock equation[2,3]

Under the Born-Oppenheimer approximation, the Hamiltonian of a molecule consisting of M fixed atomic nuclei and N electrons is expressed as follows

$$\widehat{H} = -\sum_{i=1}^{N}\frac{1}{2}\Delta_i - \sum_{i,A=1}^{N,M}\frac{Z_A}{r_{iA}} + \sum_{i>j}^{N}\frac{1}{r_{ij}}, \tag{1.1}$$

where the first term represents the kinetic energy of the electrons, the second term is the Coulomb attraction between the electron and nuclei, and the third term is the Coulomb repulsion between the electrons.

The wavefunction Ψ is approximated as an antisymmetrized product of normalized N spin orbitals $\chi_i(\boldsymbol{x})$. Each spin orbital is a product of a special orbital $\phi_k(\boldsymbol{r})$ and a spin function $\sigma(s) = \alpha(s)$ or $\beta(s)$. This antisymmetrized wavefunction is called Slater determinant [4] and is given by

$$\Psi_0(\boldsymbol{x}_1, \cdots, \boldsymbol{x}_N) = \frac{1}{\sqrt{N!}}\begin{vmatrix} \chi_1(\boldsymbol{x}_1) & \cdots & \chi_N(\boldsymbol{x}_1) \\ \vdots & \ddots & \vdots \\ \chi_1(\boldsymbol{x}_N) & \cdots & \chi_N(\boldsymbol{x}_N) \end{vmatrix}. \tag{1.2}$$

The HF method is a computational approach that determines the orthonormal spin orbitals $\chi_i(\boldsymbol{x})$ that minimize the system's energy based on the Slater determinant. According to the variational principle, the optimal spin orbitals are those that minimize the electronic energy:

$$E_0 = \langle \Psi_0 | \widehat{H} | \Psi_0 \rangle = \sum_{i=1}^{N} H_i + \frac{1}{2}\sum_{i,j=1}^{N}(J_{ij} - K_{ij}), \tag{1.3}$$

where

$$H_i = \int \chi_i^*(\boldsymbol{x}_1)\left(-\frac{1}{2}\Delta_i - \sum_{A=1}^{M}\frac{Z_A}{r_{iA}}\right)\chi_i(\boldsymbol{x}_1)d\boldsymbol{x}_1, \tag{1.4}$$

$$J_{ij} = \int\int \chi_i^*(\boldsymbol{x}_1)\chi_j^*(\boldsymbol{x}_2)\frac{1}{r_{ij}}\chi_i(\boldsymbol{x}_1)\chi_j(\boldsymbol{x}_2)d\boldsymbol{x}_1 d\boldsymbol{x}_2, \tag{1.5}$$

$$K_{ij} = \int\int \chi_i^*(\boldsymbol{x}_1)\chi_j^*(\boldsymbol{x}_2)\frac{1}{r_{ij}}\chi_i(\boldsymbol{x}_2)\chi_j(\boldsymbol{x}_1)d\boldsymbol{x}_1 d\boldsymbol{x}_2. \tag{1.6}$$

J_{ij} and K_{ij} are called Coulomb integrals and exchange integrals, respectively, with the following relationship:

$$J_{ii} = K_{ii}. \tag{1.7}$$

Minimizing Equation (1.3) subject to the orthonormalization conditions

$$\int \chi_i^*(\boldsymbol{x})\,\chi_j(\boldsymbol{x})d\boldsymbol{x} = \delta_{ij}, \tag{1.8}$$

the HF differential equations are obtained

$$\hat{f}|\chi_i\rangle = \sum_{j=1}^{N}\varepsilon_{ij}|\chi_j\rangle, \tag{1.9}$$

where

$$\hat{f}(i) = -\frac{1}{2}\Delta_i - \sum_{A=1}^{M}\frac{Z_A}{r_{iA}} + v^{HF}(i). \tag{1.10}$$

The operator $\hat{f}(i)$ is an effective one-electron operator, called the Fock operator. $v^{HF}(i)$ is the average potential influenced by the i-th electron due to the presence of the other electrons. This approach treats electron-electron repulsion in an averaged manner, allowing the complex many-body problem to be approximated as a simpler single-electron problem.

Equation (1.9) has N solutions, and their unitary transformations are also solutions of Equation (1.9). In other words, the wavefunction based on the Slater determinant is invariant under unitary transformations. Since ε is a Hermitian matrix, it is possible to choose a unitary matrix $\boldsymbol{U}$ that diagonalizes it. The corresponding orbitals χ_i' are called canonical HF orbitals and satisfy the following canonical HF equation:

$$\hat{f}|\chi_i'\rangle = \varepsilon_i'|\chi_i'\rangle. \tag{1.11}$$

Hereafter, the prime in Equation (1.11) is omitted, and it is referred to as the HF equations as

$$\hat{f}|\chi_i\rangle = \varepsilon_i|\chi_i\rangle. \tag{1.12}$$

From the above, the problem of solving a single Slater determinant can be regarded as the problem of solving molecular orbitals (MOs) using the HF equation (1.12). According to Koopmans' theorem, the canonical orbitals obtained by solving this equation are understood to be suitable for describing the removal of an electron from the system [5].

1.1.2 Restricted closed-shell HF method: Roothaan equation

By solving the HF equation, molecular information can be obtained; however, solving this equation numerically in its original form is difficult. Roothaan devised a method to solve the HF equation using standard matrix operations by introducing the linear combination of atomic orbitals (LCAO), which transforms the differential equation into a system of algebraic equations [6].

First, let us consider eliminating spin. For the restricted closed-shell case, the set of spin orbitals is

$$\chi_i(\boldsymbol{x}) = \begin{cases} \psi_j(\boldsymbol{r})\alpha(s) \\ \psi_j(\boldsymbol{r})\beta(s) \end{cases}. \tag{1.13}$$

Substituting Equation (1.13) into the HF equation (1.12), the following equation is obtained

$$\hat{f}(\boldsymbol{x}_1)\psi_j(\boldsymbol{r}_1)\alpha(s_1) = \varepsilon_j\psi_j(\boldsymbol{r}_1)\alpha(s_1). \tag{1.14}$$

Multiplying both sides of Equation (1.14) from the left by $\alpha^*(s_1)$ and integrating with respect to the spin variables, the following HF equation for the spatial orbitals in a closed-shell system is obtained

$$\hat{f}(1)\psi_j(1) = \varepsilon_j\psi_j(1), \tag{1.15}$$

where $\hat{f}(1)$ is the closed-shell Fock operator,

$$\hat{f}(1) = h(1) + \sum_{a}^{N/2} 2J_a(1) - K_a(1). \tag{1.16}$$

$J_a(1)$ and $K_a(1)$ represent the closed-shell Coulomb and exchange operators, respectively.

Next, a basis set is introduced to transform the differential equation into a set of algebraic equations. By introducing a set of K basis functions $\{\phi_\mu(\boldsymbol{r}) \mid \mu = 1,2, \ldots, K\}$, the unknown molecular orbitals $\psi_i(\boldsymbol{r})$ are expanded as a linear combination

$$\psi_i = \sum_{\mu=1}^{K} C_{\mu i}\phi_\mu, \qquad i = 1,2,\cdots,K, \tag{1.17}$$

where $C_{\mu i}$ is the μ-th orbital coefficient of i-th MO ψ, which is called LCAO-MO. Substituting Equation (1.17) into the closed-shell HF equation (1.15), multiplying both sides of equation from the left by $\phi_\mu^*(1)$ and integrating, the integro-differential equation is transformed into a matrix equation:

$$\sum_{\nu} C_{\nu i}\int \phi_\mu^*(1)\hat{f}(1)\phi_\nu(1)d\boldsymbol{r}_1 = \varepsilon_i\sum_{\nu} C_{\nu i}\int \phi_\mu^*(1)\phi_\nu(1)d\boldsymbol{r}_1. \tag{1.18}$$

Here the overlap matrix $\boldsymbol{S}$ and the Fock matrix $\boldsymbol{F}$ are defined as follows:

$$S_{\mu\nu} = \int \phi_\mu^*(1)\phi_\nu(1)d\boldsymbol{r}_1, \tag{1.19}$$

$$F_{\mu\nu} = \int \phi_\mu^*(1)\hat{f}(1)\phi_\nu(1)d\boldsymbol{r}_1, \tag{1.20}$$

and then, the HF equation (1.18) can be rewritten by using the two matrix (1.19) and (1.20),

$$\sum_{\nu} F_{\mu\nu}C_{\nu i} = \varepsilon_i\sum_{\nu} S_{\mu\nu}C_{\nu i}, \qquad i = 1,2,\cdots K, \tag{1.21}$$

or

$$\boldsymbol{FC} = \boldsymbol{SC\varepsilon}. \tag{1.22}$$

Equation (1.22) is called the Roothaan equation [6].

1.1.3 Unrestricted open-shell HF method: Pople-Nesbet equation

In Section 1.1.2, the author discussed the restricted closed-shell HF equation; here, the author derives the unrestricted open-shell Hartree-Fock (UHF) method. This method can be applied not only to open-shell systems, such as radicals, but also to problems like the dissociation of the hydrogen molecule when the bond length becomes large.

In open-shell systems, spatial orbitals are described separately for electrons with α-spin and β-spin.

$$\chi_i(\boldsymbol{x}) = \begin{cases} \psi_j^{\alpha}(\boldsymbol{r})\alpha(s) \\ \psi_j^{\beta}(\boldsymbol{r})\beta(s) \end{cases}. \tag{1.23}$$

The derivation of the UHF equation is similar to the restricted case. Specifically, by substituting Equation (1.23) into Equation (1.12) and integrating over the spin variables after multiplying both sides from the left by $\alpha^*(s_1)$ or $\beta^*(s_1)$,

$$\hat{f}^{\alpha}(1)\psi_j^{\alpha}(1) = \varepsilon_j^{\alpha}\psi_j^{\alpha}(1), \tag{1.24}$$

$$\hat{f}^{\beta}(1)\psi_j^{\beta}(1) = \varepsilon_j^{\beta}\psi_j^{\beta}(1). \tag{1.25}$$

To solve the UHF equations (1.24) and (1.25), the basis functions are introduced, and molecular orbitals are defined separately for the α-spin and β-spin electrons as follows:

$$\psi_i^{\alpha} = \sum_{\mu=1}^{K} C_{\mu i}^{\alpha}\phi_{\mu}, \qquad i = 1,2,\cdots,K, \tag{1.26}$$

$$\psi_i^{\beta} = \sum_{\mu=1}^{K} C_{\mu i}^{\beta}\phi_{\mu}, \qquad i = 1,2,\cdots,K. \tag{1.27}$$

As in the case of the Roothaan equations, substituting Equations (1.26) and (1.27) into the HF equation (1.16), and multiplying both sides from the left by $\phi_{\mu}^*(1)$ and integrating, the differential equation is transformed into an algebraic equation

$$\boldsymbol{F}^{\alpha}\boldsymbol{C}^{\alpha} = \boldsymbol{SC}^{\alpha}\boldsymbol{\varepsilon}^{\alpha}, \tag{1.28}$$

$$\boldsymbol{F}^{\beta}\boldsymbol{C}^{\beta} = \boldsymbol{SC}^{\beta}\boldsymbol{\varepsilon}^{\beta}. \tag{1.29}$$

Equations (1.28) and (1.29) are called the Pople-Nesbet eqautions [7].

Since the Fock matrix $\boldsymbol{F}$ depends on the orbital coefficient $\boldsymbol{C}$, the Roothaan equation (1.22) and the Pople-Nesbet equations (1.28) and (1.29) are nonlinear. Therefore, starting with an appropriate initial value of $\boldsymbol{C}$, the energy is calculated iteratively, updating $\boldsymbol{C}$ until it converges and no longer changes. This procedure is called the self-consistent field (SCF) method.

1.2 Density functional theory

Density functional theory (DFT) has been widely used since the 1990s as it efficiently incorporates electron correlation in the form of electron density, and it has now become one of the primary methods in computational chemistry [8]. The DFT approach expresses electron correlation as a functional of the electron density. The foundation of this approach dates back to the Hohenberg-Kohn theorem proposed in 1964.

1.2.1 Hohenberg-Kohn theorems

Hohenberg-Kohn theorem consists of two fundamental theorems [9].

The first Hohenberg-Kohn theorem

The external potential $v(\boldsymbol{r})$ is uniquely determined by the electron density $\rho(\boldsymbol{r})$.

The second Hohenberg-Kohn theorem

For a trial density $\tilde{\rho}(\boldsymbol{r})$ such that $\tilde{\rho}(\boldsymbol{r}) \geq 0$ and $\int \tilde{\rho}(\boldsymbol{r})d\boldsymbol{r} = N$, then $E_0 \leq E_v[\tilde{\rho}(\boldsymbol{r})]$.

The first Hohenberg-Kohn theorem establishes that the Hamiltonian is uniquely determined by the external potential. Once the Hamiltonian is determined, the wavefunction can be obtained. From the wavefunction, the electron density can be constructed. Therefore, this theorem demonstrates a one-to-one correspondence between the electron density, the nuclear potential, the Hamiltonian, and the total energy. The first theorem is proven by reductio ad absurdum. Suppose there exist two external potentials v and v' that differ by more than a constant and yield the same ground state electron density. Then, there would exist two Hamiltonians $\hat{H}$ and $\hat{H}'$ corresponding to these potentials, which share the same ground state density. However, the normalized wavefunctions Ψ and Ψ' corresponding to $\hat{H}$ and $\hat{H}'$, respectively, must be different. When Ψ' is used as the trial wavefunction for $\hat{H}$,

$$E_0 < \langle \Psi' | \hat{H} | \Psi' \rangle = \langle \Psi' | \hat{H}' | \Psi' \rangle + \langle \Psi' | \hat{H} - \hat{H}' | \Psi' \rangle$$
$$= E_0' + \int \rho(\boldsymbol{r})[v(\boldsymbol{r}) - v'(\boldsymbol{r})]d\boldsymbol{r}, \tag{1.30}$$

where E_0 and E_0' are the grand state energies corresponding to $\hat{H}$ and $\hat{H}'$, respectively. Similarly, when Ψ is used as the trial function for $\hat{H}'$, the following inequality holds,

$$E_0' < \langle \Psi | \hat{H}' | \Psi \rangle = \langle \Psi | \hat{H} | \Psi \rangle + \langle \Psi | \hat{H}' - \hat{H} | \Psi \rangle$$
$$= E_0 + \int \rho(\boldsymbol{r})[v'(\boldsymbol{r}) - v(\boldsymbol{r})]d\boldsymbol{r}. \tag{1.31}$$

Addition Equations (1.30) and (1.31), the following contradictory equation is obtained,

$$E_0 + E_0' < E_0' + E_0. \tag{1.32}$$

Therefore, two external potentials that give the same ground state electron density $\rho(\boldsymbol{r})$ cannot exist. In other words, once the electron density $\rho(\boldsymbol{r})$ is determined, the external potential $v(\boldsymbol{r})$ is uniquely

determined.

The second Hohenberg-Kohn theorem states that the Hamiltonian operator expressed in terms of the ground state electron density always has a solution that minimizes the energy, demonstrating the variational principle for the energy. The requirement of the variational principle arises from the stationary principle with respect to the electron density of the ground state,

$$\delta\left\{E_v[\rho(\boldsymbol{r})] - \mu\left[\int \rho(\boldsymbol{r})d\boldsymbol{r} - N\right]\right\} = 0. \tag{1.33}$$

The Euler-Lagrange equation can be obtained from Equation (1.33),

$$\mu = \frac{\delta E_v[\rho(\boldsymbol{r})]}{\delta\rho(\boldsymbol{r})} = v(\boldsymbol{r}) + \frac{\delta F_{\mathrm{HK}}[\rho(\boldsymbol{r})]}{\delta\rho(\boldsymbol{r})}, \tag{1.34}$$

where μ represents the chemical potential. $F_{\mathrm{HK}}[\rho(\boldsymbol{r})]$ is defined independently of the external potential, which means that it is a universal functional of $\rho(\boldsymbol{r})$. If $F_{\mathrm{HK}}[\rho(\boldsymbol{r})]$ could be explicitly written, the Hohenberg-Kohn theorem could be applied to any systems; however, obtaining such a functional $F_{\mathrm{HK}}[\rho(\boldsymbol{r})]$ is extremely difficult.

1.2.2 Levy constrained search

According to the Hohenberg-Kohn theorem, if a trial electron density $\tilde{\rho}(\boldsymbol{r})$ is non-negative and the total particle number is finite, the external potential is uniquely determined. Here, if *v*-representability is defined as "a system is *v*-representable if the electron density $\rho(\boldsymbol{r})$ is derived from the ground state antisymmetric wavefunction for a Hamiltonian with a given external potential $v(\boldsymbol{r})$," then, for example, when the ground state is degenerate, multiple wavefunctions can yield the same density, meaning the system is not *v*-representable. Furthermore, as shown in the following equation, the formulation of DFT is still possible even if the conditions on the density in the variational principle are relaxed.

$$\tilde{\rho}(\boldsymbol{r}) \geq 0, \int \tilde{\rho}(\boldsymbol{r})\, d\boldsymbol{r} = N, \text{and } \int \left|\nabla\tilde{\rho}^{\frac{1}{2}}(\boldsymbol{r})\right|^2 d\boldsymbol{r} < \infty. \tag{1.35}$$

It is called *N*-representability and means that a density is obtained from some antisymmetric wavefunction. Since *N*-representability is a necessary condition for *v*-representability, the conditions for *N*-representability are weaker than those for *v*-representability.

The one-to-one correspondence between the ground state density and the wavefunction has been established, so now considering how to determine the wavefunction when the density is given. The density $\rho_0(\boldsymbol{r})$ is expressed as the square of the wavefunction Ψ_0, but there exist infinitely many antisymmetric wavefunctions that yield the same density. If such wavefunction is denoted that satisfies $\rho_0(\boldsymbol{r})$ as Ψ_{ρ_0},

$$\langle\Psi_{\rho_0}|\hat{H}|\Psi_{\rho_0}\rangle \geq \langle\Psi_0|\hat{H}|\Psi_0\rangle = E_0. \tag{1.36}$$

Equation (1.36) is trivial from the stationary principle with respect to the electron density of the ground state. The Hamiltonian of *N* electrons system is $\hat{H} = \hat{T} + \hat{V}_{ee} + \sum_i^N v(\boldsymbol{r_i})$ ($\hat{T}$ and $\hat{V}_{ee}$ are the kinetic

energy and potential energy, respectively.), and then, the following equation is obtained:

$$\langle \Psi_{\rho_0} | \hat{T} + \hat{V}_{ee} | \Psi_{\rho_0} \rangle + \int v(\boldsymbol{r})\, \rho_0(\boldsymbol{r}) d\boldsymbol{r} \geq \langle \Psi_0 | \hat{T} + \hat{V}_{ee} | \Psi_0 \rangle + \int v(\boldsymbol{r})\, \rho_0(\boldsymbol{r}) d\boldsymbol{r}$$

$$\therefore \langle \Psi_{\rho_0} | \hat{T} + \hat{V}_{ee} | \Psi_{\rho_0} \rangle \geq \langle \Psi_0 | \hat{T} + \hat{V}_{ee} | \Psi_0 \rangle. \tag{1.37}$$

The right-hand side of Equation (1.37) shows *v*-representability, and the left-hand side shows *N*-representability. Minimizing the left-hand side of Equation (2.37), it turns to show *v*-representability.

$$F_{\mathrm{HK}}[\rho_0(\boldsymbol{r})] = \langle \Psi_0 | \hat{T} + \hat{V}_{ee} | \Psi_0 \rangle = \min_{\Psi \to \rho_0} \langle \Psi | \hat{T} + \hat{V}_{ee} | \Psi \rangle. \tag{1.38}$$

This is a constrained search for the density functional $F_{\mathrm{HK}}[\rho_0(\boldsymbol{r})]$ [10]. That is, by searching over all antisymmetric wavefunctions corresponding to a density $\rho_0(\boldsymbol{r})$, a *v*-representable wavefunction can be obtained. Therefore, the condition of non-degenerate ground states, which is a limitation of the Hohenberg-Kohn theorem, can be removed. In essence, the ground state energy is expressed as a functional of the density, as shown below.

$$[\rho(\boldsymbol{r})] = F[\rho(\boldsymbol{r})] + \int v(\boldsymbol{r})\, \rho_0(\boldsymbol{r}) d\boldsymbol{r}$$

$$= \min_{\Psi \to \rho_0} \langle \Psi | \hat{T} + \hat{V}_{ee} | \Psi \rangle + \int v(\boldsymbol{r})\, \rho_0(\boldsymbol{r}) d\boldsymbol{r}. \tag{1.39}$$

1.2.3 Kohn-Sham equation

In Section 1.2.1, the electron density of the grand state is obtained by minimizing $E[\rho(\boldsymbol{r})]$, and satisfies the Euler-Lagrange equation (1.34). The density functional $F_{\mathrm{HK}}[\rho(\boldsymbol{r})]$ is expressed as below,

$$F_{\mathrm{HK}}[\rho(\boldsymbol{r})] = T[\rho(\boldsymbol{r})] + V_{ee}[\rho(\boldsymbol{r})]. \tag{1.40}$$

If the kinetic energy term $T[\rho(\boldsymbol{r})]$ and the electron-electron interaction term $V_{ee}[\rho(\boldsymbol{r})]$ could be explicitly expressed, this method could be applied to any system. However, it is difficult to obtain their explicit forms beyond rough approximations. Kohn and Sham proposed to introduce the orbitals into this problem [11].

The kinetic energy without the interactions can be expressed by wavefunctions as below,

$$T_s = \sum_{i=1}^{N} \left\langle \Psi_s \middle| -\frac{1}{2}\Delta \middle| \Psi_s \right\rangle. \tag{1.41}$$

Using T_s, Equation (1.40) can be rewritten as:

$$F[\rho(\boldsymbol{r})] = T_s + J[\rho(\boldsymbol{r})] + E_{XC}[\rho(\boldsymbol{r})], \tag{1.42}$$

where

$$E_{XC}[\rho(\boldsymbol{r})] = T[\rho(\boldsymbol{r})] - T_s + V_{ee}[\rho(\boldsymbol{r})] - J[\rho(\boldsymbol{r})]. \tag{1.43}$$

$E_{XC}[\rho(\boldsymbol{r})]$ is called the exchange-correlation energy. This term contains the difference between $T[\rho(\boldsymbol{r})]$ and T_s, and the electron-electron interaction term. In other words, the parts of the energy that cannot be explicitly expressed are integrated into this term.

The energy functional is expressed as follows:

$$E[\rho(\boldsymbol{r})] = T[\rho(\boldsymbol{r})] + V_{ee}[\rho(\boldsymbol{r})] + \int \rho(\boldsymbol{r})v(\boldsymbol{r})d\boldsymbol{r}$$

$$= \sum_{i=1}^{N}\sum_{s}\int \Psi_i^{s,*}(\boldsymbol{r})\left(-\frac{1}{2}\Delta\right)\Psi_i^{s}(\boldsymbol{r})d\boldsymbol{r} + J[\rho(\boldsymbol{r})] + E_{XC}[\rho(\boldsymbol{r})] + \int \rho(\boldsymbol{r})v(\boldsymbol{r})d\boldsymbol{r}. \quad (1.44)$$

The relationship between the electron densities and molecular orbitals is

$$\rho(\boldsymbol{r}) = \sum_{i=1}^{N}\sum_{s}\Psi_i^{s*}(\boldsymbol{r})\Psi_i^{s}(\boldsymbol{r}). \quad (1.45)$$

Thus, the energy can be expressed by N orbitals.

In order to derive the Kohn-Sham (KS) equation, it is necessary to minimize $E[\rho(\boldsymbol{r})]$ with respect to the orbitals under the constraint that the orbitals are the orthonormal,

$$\int \Psi_i^*(\boldsymbol{r})\Psi_j(\boldsymbol{r})d\boldsymbol{r} = \delta_{ij}. \quad (1.46)$$

A functional $\Omega[\{\Psi_i\}]$ of the N orbitals is considered as follows:

$$\Omega[\{\Psi_i\}] = E[\rho(\boldsymbol{r})] - \sum_{i}^{N}\sum_{j}^{N}\varepsilon_{ij}\int \Psi_i^*(\boldsymbol{r})\Psi_j(\boldsymbol{r})d\boldsymbol{r}, \quad (1.47)$$

where $E[\rho(\boldsymbol{r})]$ is the functional of Ψ_i, which is expressed by Equations (1.44) and (1.45), and ε_{ij} is a set of the Lagrange multipliers. To minimize $E[\rho(\boldsymbol{r})]$ under the given constraint, minimizing $\Omega[\{\Psi_i\}]$ is require. That is, $\Omega[\{\Psi_i\}] = 0$, and these equations are obtained,

$$\left[-\frac{1}{2}\Delta + v_{\text{eff}}\right]\Psi_i = \sum_{j=1}^{N}\varepsilon_{ij}\Psi_j, \quad (1.48)$$

$$v_{\text{eff}}(\boldsymbol{r}) = v(\boldsymbol{r}) + \int \frac{\rho(\boldsymbol{r}')}{|\boldsymbol{r}-\boldsymbol{r}'|}d\boldsymbol{r}' + v_{XC}(\boldsymbol{r}). \quad (1.49)$$

Finally, the canonical KS equation follow as:

$$\left[-\frac{1}{2}\Delta + v_{\text{eff}}\right]\Psi_i = \varepsilon_i\Psi_i, \quad (1.50)$$

where $v_{\text{eff}}(\boldsymbol{r})$ is an effective potential (Kohn-Sham potential). The KS equation has the same form as the HF equation, except that it includes a more general local potential. Therefore, if the potential is uniquely determined, it can be solved in the same manner as in HF theory. If $E_{XC}[\rho]$ and $v_{XC}(\boldsymbol{r})$ represent the exact exchange-correlation energy and potential, solving the KS equation yields the exact energy, including electronic correlation effects. In other words, the KS approximation enables calculations that include challenging electronic correlation effects with computational effort similar to that of the HF method.

In the case of a one-electron system, the Coulomb energy $J[\rho]$ depends solely on the electron density ρ, resulting in a finite value. This leads to the unphysical situation where a single electron interacts with itself. In the HF method (and correlation methods based on it), this issue is resolved as the

exchange integral precisely cancels out the Coulomb integral. However, in the case of approximate exchange-correlation functionals, this cancellation is not exact, leading to a problem. This problem is called the self-interaction errors (SIE).

1.3 Exchange-correlation functional

Up to this point, Hohenberg and Kohn have shown that the exchange-correlation functional $E_{XC}[\rho(\boldsymbol{r})]$ is determined solely by the electron density. However, obtaining an explicit form of $E_{XC}[\rho(\boldsymbol{r})]$ is extremely difficult, and thus approximate functionals are employed.

1.3.1 Local density approximation

The $E_{XC}[\rho(\boldsymbol{r})]$ functional is typically divided into the exchange functional $E_X[\rho(\boldsymbol{r})]$ and the correlation functional $E_C[\rho(\boldsymbol{r})]$. The first approximation to the exchange functional $E_X[\rho(\boldsymbol{r})]$ is called the local density approximation (LDA). This functional is introduced by using the basic model of DFT, called a homogeneous electron gas (HEG). The HEG, also known as the Jellium model, is a system in which N electrons exist within a uniformly distributed positive charge background of N positive charges.

To derive this model, a box potential system in which N electrons move within a cube of edge length l under periodic boundary conditions is considered [12]. The electronic wavefunctions for such a box potential system are given as:

$$\Psi = \frac{1}{l^{\frac{3}{2}}} e^{i(k_x x + k_y y + k_z z)} = \frac{1}{\sqrt{V}} e^{i\boldsymbol{k}\cdot\boldsymbol{r}}, \tag{1.51}$$

where

$$k_x = \frac{2\pi}{l} n_x, k_y = \frac{2\pi}{l} n_y, k_z = \frac{2\pi}{l} n_z. \tag{1.52}$$

By using Equation (1.51), the spin-independent first-order density matrix is expressed as follows:

$$\begin{aligned} \rho_1(\boldsymbol{r}_1, \boldsymbol{r}_2) &= \sum_i^{N/2} \phi_i(\boldsymbol{r}_1) \phi_i^*(\boldsymbol{r}_1') \\ &= \frac{2}{V} \sum_{k_{occ}} e^{i\boldsymbol{k}\cdot(\boldsymbol{r}_1 - \boldsymbol{r}_2)} \\ &\approx \frac{1}{4\pi^3} \int e^{i\boldsymbol{k}\cdot(\boldsymbol{r}_1 - \boldsymbol{r}_2)} \, d\boldsymbol{k} \\ &= \frac{1}{4\pi^3} \int_0^{k_F} \boldsymbol{k}^2 d\boldsymbol{k} \int \int e^{i\boldsymbol{k}\cdot(\boldsymbol{r}_1 - \boldsymbol{r}_2)} \sin\theta \, d\theta d\phi, \end{aligned} \tag{1.53}$$

where

$$dn = \left(\frac{l}{2\pi}\right)^3 dk = \left(\frac{V}{8\pi}\right) dk.$$

k_F is called the Fermi moment and determined as below:

$$k_F = \{3\pi^2\rho(\boldsymbol{r})\}^{\frac{1}{3}}. \tag{1.54}$$

In inhomogeneous systems, the average of $\boldsymbol{r}_1$ and $\boldsymbol{r}_2$ is often used. Thus, a variable is defined such as

$$\boldsymbol{r} = \frac{1}{2}(\boldsymbol{r}_1 + \boldsymbol{r}_2), \quad \boldsymbol{s} = \boldsymbol{r}_1 - \boldsymbol{r}_2, \tag{1.54}$$

and s is taken the k_z-direction, then,

$$\rho_1(\boldsymbol{r}_1, \boldsymbol{r}_2) = \frac{1}{4\pi^3}\int_0^{k_F} \boldsymbol{k}^2 d\boldsymbol{k} \int_0^{\pi} e^{i\boldsymbol{k}\cdot\boldsymbol{r}_{12}\cos\theta} \sin\theta \, d\theta \int_0^{2\pi} d\phi$$

$$= 3\rho(\boldsymbol{r})\left[\frac{\sin \boldsymbol{t} - \boldsymbol{t}\cos t}{\boldsymbol{t}^3}\right] = \rho_1(\boldsymbol{r}, \boldsymbol{s}), \tag{1.55}$$

where $\boldsymbol{t} = k_F(\boldsymbol{r})\boldsymbol{s}$. Expressed in terms of coordinates $\boldsymbol{r}$ and $\boldsymbol{s}$, this equation represents the exact spin-independent first-order density matrix for the HEG. By using the spherical Bessel functions,

$$j_0(z) = \frac{\sin z}{z}, j_1(z) = \frac{\sin z}{z^2} - \frac{\cos z}{z}, \tag{1.56}$$

Equation (1.55) can be rewritten as

$$\rho_1(\boldsymbol{r}_1, \boldsymbol{r}_2) = \frac{3j_1(sk_F)}{sk_F}\rho(\boldsymbol{r}). \tag{1.57}$$

Using this first-order reduced density matrix, the kinetic energy and exchange energy can be calculated. The kinetic energy functional is given as follows:

$$T_{TF}[\rho(\boldsymbol{r})] = \frac{3}{10}(3\pi^2)^{\frac{2}{3}}\int \rho^{\frac{5}{3}}(\boldsymbol{r})\, d\boldsymbol{r}. \tag{1.58}$$

Equation (1.58) is called the Thomas-Fermi kinetic energy. The exchange energy functional is given as follows:

$$E_x[\rho(\boldsymbol{r})] = \frac{3}{4}\left(\frac{3}{\pi}\right)^{\frac{1}{3}}\int \rho^{\frac{3}{4}}(\boldsymbol{r})\, d\boldsymbol{r}. \tag{1.59}$$

Equation (1.59) is celled the Dirac exchange energy or Slater exchange energy. Thus, the exchange energy is proportional to the electron density raised to the power of 4/3, and the kinetic energy is proportional to the electron density raised to the power of 5/3.

1.3.2 Expansion to open-shell system

In the DFT calculations, when dealing with open-shell electronic structures, it is necessary to consider spin-unrestricted orbitals, similar to the HF theory. The spin-unrestricted DFT calculation is also called the spin-polarized DFT, where the difference between the α-spin density and β-spin density is taken into account. The kinetic energy functional and exchange energy functional can be separate into each spin element,

$$T_{TF}[\rho_\alpha, \rho_\beta] = T_{TF}[\rho_\alpha, 0] + T_{TF}[0, \rho_\beta]$$

$$= \frac{1}{2} T_{TF}[\rho_\alpha, \rho_\beta] + \frac{1}{2} T_{TF}[\rho_\alpha, \rho_\beta]$$

$$= \frac{1}{2} T_s{}^0[2\rho_\alpha] + \frac{1}{2} T_s{}^0[2\rho_\beta], \tag{1.60}$$

$$E_X[\rho_\alpha, \rho_\beta] = \frac{1}{2} E_X[\rho_\alpha, \rho_\beta] + \frac{1}{2} E_X[\rho_\alpha, \rho_\beta]$$

$$= \frac{1}{2} E_X{}^0[2\rho_\alpha] + \frac{1}{2} E_X{}^0[2\rho_\beta], \tag{1.61}$$

where T_s^0 and E_X^0 are the kinetic energy and exchange energy for the total density in the closed-shell system. The Thomas-Fermi kinetic energy is given as follows:

$$T_{TF}[\rho_\alpha, \rho_\beta] = 2^{\frac{2}{3}} C_{TF}^0 \int \left[\rho_\alpha{}^{\frac{3}{5}} + \rho_\beta{}^{\frac{3}{5}} \right] d\boldsymbol{r}$$

$$= \sum_{\sigma=\alpha,\beta} \int C_{TF}^1 \, \rho_\sigma{}^{\frac{3}{5}} d\boldsymbol{r}, \tag{1.62}$$

$$C_{TF}^0 = \frac{3}{10} (3\pi^2)^{\frac{2}{3}}, C_{TF}^1 = \frac{3}{10} (6\pi^2)^{\frac{2}{3}}. \tag{1.63}$$

The Dirac exchange energy is

$$E_X[\rho_\alpha, \rho_\beta] = -2^{\frac{1}{3}} C_X^0 \int \left[\rho_\alpha{}^{\frac{4}{3}} + \rho_\beta{}^{\frac{4}{3}} \right] d\boldsymbol{r}$$

$$= \sum_{\sigma=\alpha,\beta} \int C_X^1 \, \rho_\sigma{}^{\frac{4}{3}} d\boldsymbol{r}, \tag{1.64}$$

$$C_X^0 = \frac{3}{4} \left(\frac{3}{\pi} \right)^{\frac{1}{3}}, C_X^1 = \frac{3}{2} \left(\frac{3}{4\pi} \right)^{\frac{1}{3}}. \tag{1.65}$$

The variable that express the spin polarization is defined as follows:

$$\zeta = \frac{\rho_\alpha - \rho_\beta}{\rho} = \frac{\rho_\alpha - \rho_\beta}{\rho_\alpha + \rho_\beta}, \tag{1.66}$$

where

$$\rho_\alpha = \frac{1}{2}(1 + \zeta)\rho, \rho_\beta = \frac{1}{2}(1 - \zeta)\rho.$$

The exchange energy functional (1.64) can be rewritten by using Equation (1.66),

$$E_X[\rho_\alpha, \rho_\beta] = \int \rho \epsilon_X(\rho, \zeta) d\boldsymbol{r}, \tag{1.67}$$

$$\epsilon_X(\rho, \zeta) = \epsilon_X^0(\rho) + [\epsilon_X^1(\rho) - \epsilon_X^0(\rho)] f(\zeta), \tag{1.68}$$

$$f(\zeta) = \frac{1}{2^{\frac{4}{3}} - 2} [(1 + \zeta)^{\frac{4}{3}} + (1 - \zeta)^{\frac{4}{3}} - 2], \tag{1.69}$$

where $\epsilon_X(\rho,\zeta)$ is the exchange energy density; $\epsilon_X^0 = C_X^0 \rho_\sigma^{\frac{4}{3}}$ is a spin-compensated (paramagnetic) exchange energy and $\epsilon_X^1 = C_X^1 \rho_\sigma^{\frac{4}{3}}$ is a fully spin-polarized (ferromagnetic) exchange energy of HEG. Such a spin-polarized LDA is also referred to as the local spin density approximation (LSDA).

1.3.3 Correlation energy functional for LDA

Unlike the kinetic and exchange functionals, which can be derived exactly for the HEG, the correlation functional is not exactly known even for the HEG. Therefore, the correlation functional is obtained by fitting empirical functional forms to the correlation energy extracted from the total energy of the HEG obtained through numerical simulations, such as quantum Monte Carlo calculations, after subtracting the kinetic and exchange energies. Below, the author introduces two commonly used types of LDA correlation functionals.

・VWN correlation functional [13]

The functional developed by Vosko, Wilk, and Nusair (VWN) uses analytical information for the upper and lower limits of the density to determine the correlation energy density for spin-unpolarized (0) and spin-polarized (1) systems.

$$\begin{aligned}\epsilon_{0/1}^{VWN}(x) = A\Bigg\{&\ln\frac{x^2}{X(x)} + \frac{2b}{Q}\tan^{-1}\frac{Q}{2x+b} \\ &- \frac{bx_0}{X(x_0)}\left[\ln\frac{(x-x_0)^2}{X(x)} + \frac{2(b+2x_0)}{Q}\tan^{-1}\frac{Q}{2x+b}\right]\Bigg\}, \\ x = \sqrt{r_s}, X(x) &= x^2 + bx + c, Q = \sqrt{4c-b}\end{aligned} \tag{1.70}$$

By interpolating between these limits, the correlation energy density $\epsilon_C^{VWN}(r_s,\zeta)$ applicable to general cases is obtained.

$$\epsilon_C^{VWN}(r_s,\zeta) = \epsilon_0^{VWN}(r_s) + \epsilon_1^{VWN}(r_s)\left[\frac{f_2(\zeta)}{f_2''(0)}\right](1-\zeta^4) + [\epsilon_1^{VWN}(r_s) - \epsilon_0^{VWN}(r_s)]f_2(\zeta)\zeta^4, \tag{1.71}$$

$$f_2(\zeta) = \frac{f_1(\zeta) - 2}{2^{\frac{1}{3}} - 1},$$

where r_s is the variable defined from

$$\frac{4}{3}\pi {r_s}^3 = \frac{1}{\rho}, \tag{1.72}$$

which is the radius of an effective volume containing a single electron, known as the Wigner-Seitz radius.

・PW92 correlation functional [14]

This functional was proposed by Perdew and Wang.

$$\epsilon_{0/1}^{PW92} = -2a\rho(1 - ar_s) \times \ln\left[1 + \frac{1}{2a\left(\beta_1 r_s^{\frac{1}{2}} + \beta_2 r_s + \beta_3 r_s^{\frac{3}{2}} + \beta_4 r_s\right)}\right], \tag{1.73}$$

These functionals are used interpolating at ζ = 0 to 1.

1.3.4 Generalized gradient approximation

So far, the LDA has been introduced; however, LDA has two main drawbacks. The first is that it is based on the HEG, even though the charge density in real systems is not uniform. The second is that it does not correctly describe the $\boldsymbol{r}$-dependence in the limit as $\boldsymbol{r} \to \infty$. To incorporate the inhomogeneity of the charge density, which was not considered in LDA, a correction using the density gradient is introduced. This approach is called the generalized gradient approximation (GGA). The GGA functionals are currently the main functionals used in density functional theory and can generally be expressed as follows:

$$E_{XC}^{\mathrm{GGA}}[\rho_\alpha, \rho_\beta] = \int e_{XC}^{\mathrm{GGA}}(\rho_\alpha, \rho_\beta, \nabla\rho_\alpha, \nabla\rho_\beta) d\boldsymbol{r}. \tag{1.74}$$

Similar to the LDA, the exchange-correlation functional is separated into exchange and correlation components, and approximations are made for each.

1.3.5 GGA exchange functional

The GGA exchange functionals are generally written as

$$E_X^{\mathrm{GGA}} = \sum_{\sigma=\alpha,\beta} \int F_X(x_\sigma)\rho^{\frac{4}{3}}(\boldsymbol{r}) d\boldsymbol{r}, \tag{1.75}$$

where F_X is a expansion function of x_σ, and in the case of LDA, $F_X^{LDA} = C_D^l$. x_σ is a variable that expressed the local heterogeneity,

$$x_\sigma = \frac{|\nabla\rho_\sigma|^2}{\rho^{\frac{4}{3}}}. \tag{1.76}$$

This variable represents the deviation from the uniform electron gas and can take large values not only in regions with significant electron density gradients near the nucleus but also in low-density regions, such as the asymptotic region where the density decays exponentially. Similarly, small gradients are typical in bonding regions but can also occur in high-density regions. The notable differences in this region arise because, while the exact local density limit and GGA limit for exchange energy exist as fundamental physical conditions, the physical constraints on functionals in regions of high-density gradients or low electron density are largely unknown. Below, several representative GGA exchange functionals are introduced.

・Becke88 exchange functional [15]

$$E_X^{B88} = E_X^{LDA} \frac{\zeta {x_\sigma}^2}{1 + 6\zeta x_\sigma \sinh^{-1} x_\sigma}. \tag{1.77}$$

Here, ζ is a parameter with a value of 0.042, and the functional is designed to satisfy the asymptotic behavior of the exchange energy density. Due to its improved accuracy in reproducing physical properties compared to previously developed functionals, it was widely used in combination with LYP correlation or Perdew86 correlation [16], among others, contributing significantly to the widespread adoption of DFT.

・PBE exchange functional [17]

$$E_X^{PBE} = E_X^{LDA}\left[1 + \kappa - \frac{\kappa}{1 + \mu/\kappa {s_\sigma}^2}\right] = E_X^{LDA}\left[1 + \kappa \frac{\mu/\kappa {s_\sigma}^2}{1 + \mu/\kappa {s_\sigma}^2}\right] \tag{1.78}$$

PBE exchange fictional is simplified and derived from PW91, and widely used as well as B88 exchange functional. The revPBE [18], which recalibrated the parameters, is also commonly used.

LDA exchange functional is known to consistently underestimate the exchange energy, and this underestimation is significantly improved in GGA exchange functional. On the other hand, the differences between GGA exchange functionals are relatively small compared to the discrepancy with LDA.

1.3.6 GGA correlation functional

GGA correlation functionals improve the LDA correlation functionals by multiplying them with a GGA enhancement factor, similar to the GGA exchange functionals. Some example of GGA correlation functionals are introduced as below.

・PBE correlation functional [17]

PBE correlation functional is obtained by adding $H(t)$ to the PW92 correlation functional (1.73).

$$\epsilon_C^{PBE} = \epsilon_C^{LDA} + H(t),$$

$$H(t) = c{f_3}^3 \ln\left[1 + dt^2\left(\frac{1 + At^2}{1 + At^2 + A^2t^4}\right)\right], \tag{1.79}$$

$$A = d\left[exp\left(-\frac{\epsilon_C^{LDA}}{c{f_2}^3}\right)\right]^{-1},$$

$$f_3(\zeta) = \frac{1}{2}\left[(1+\zeta)^{\frac{2}{3}} + (1-\zeta)^{\frac{2}{3}}\right],$$

$$t = \left[2(3\pi^3)^{\frac{1}{3}} f_s\right]^{-1} x.$$

・Lee-Yang-Parr (LYP) correlation functional [19]

The PBE correlation functional was created by multiplying the LDA correlation functional by a GGA factor. However, there is also an approach to derive correlation functionals based on approximate correlation wavefunctions, known as Colle-Salvetti type correlation functionals. First, the correlation wavefunction $\Psi_0(x_1, x_2, \ldots, x_n)$ is approximated as the product of the Slater determinant from the HF method and a Jastrow factor.

$$\Psi_0(x_1, x_2, \cdots, x_n) = \Psi_0^{\mathrm{HF}}(x_1, x_2, \cdots, x_n) \prod_{i<j} \left[1 - \Phi_{12}(r_i, r_j)\right], \tag{1.80}$$

where Ψ_0^{HF} is the Slater determinant (1.2), $\Phi_{12}(r_i, r_j)$ is a correlation factor, which describes the correlations between all particle pairs. The Colle-Salvetti wavefunction is given as follows [20,21]:

$$\Phi_{12}(r_i, r_j) = e^{-\beta^2 s^2} \left\{1 - \Psi_0^{\mathrm{HF}}(R) \left(1 + \frac{s}{2}\right)\right\}, \tag{1.81}$$

where R and s are the variables between two electrons. A parameter β determines the size of the Coulomb hole, and q is a dimensionless parameter, q = 2.29. In regions of high electron density, the Coulomb hole is deep and localized, while in regions of low electron density, the Coulomb hole is shallow and spread out. Using these relationships in calculations, the electron correlation energy is expressed as:

$$E_C^{CS} = -4a \int \frac{\rho_2^{HF}(r,s)}{\rho} \left[1 + b\rho^{-\frac{8}{3}} [\nabla_s^2 \rho_2^{HF}(r,s)]_{s=0} e^{-c\rho^{-\frac{1}{3}}}\right] \times \left(1 + d\rho^{-\frac{1}{3}}\right)^{-1} dr, \tag{1.82}$$

where ρ_2^{HF} is the pair density matrix (diagonal elements of the second-order electron density) in the HF method. Four parameters, a, b, c and d, can be fitted by the He atom.

One of the most widely used functionals, the Lee-Yang-Parr (LYP) correlation functional, is derived from the Colle-Salvetti electron correlation energy. The LYP functionals is known to provide highly accurate correlation energy in molecular property calculations. In practice, the expressions commonly used are the one proposed by Miehlich et al. [22], which converts the Laplacian term $\Delta\rho$ into a density gradient term through integration by parts, and the implementation formula proposed by Johnson et al. [23]. Although the mathematical expression is omitted due to its complexity, one characteristic feature is the presence of a $\rho_\alpha\rho_\beta$ term. This ensures that, for single-electron systems, it equals zero, meaning that the correlation functional does not suffer from self-interaction.

For closed-shell atoms, LDA correlation functionals overestimate the correlation energy by about a factor of two, but this overestimation is significantly improved with GGA correlation functionals such as LYP and PBE. Similarly to exchange functionals, the energy differences between GGA functionals are much smaller compared to the discrepancy with LDA. Notably, although LYP and PBE have significantly different functional forms, they are known to achieve comparable computational accuracy.

1.3.7 Hybrid exchange-correlation functional

In Section 1.2.3, DFT calculations have the issue of self-interaction error (SIE), where electrons interact with themselves. On the other hand, the HF method resolves the SIE issue as the exchange integral precisely cancels out the Coulomb integral. Additionally, DFT calculations tend to overestimate the delocalization of electrons, whereas HF calculations overestimate the electron localization. Therefore, to improve the SIE issue in DFT, hybrid exchange-correlation functionals, which incorporate a portion of the HF exchange energy into GGA functionals, have been proposed and are widely used today.

Generally, the hybrid exchange-correction functional is written as follows:

$$E_{XC}^{hybrid} = c_X^{HF} E_X^{HF} + \sum_i c_X^i E_X^i + \sum_j c_C^j E_C^j, \tag{1.83}$$

where

$$c_X^{HF} + \sum_i c_X^i E_X^i = 1,$$

$$\sum_j c_C^j E_C^j = 1.$$

E_X^{HF}, E_X^i and E_C^j are the HF exchange energy, i-th exchange functional and j-th correlation functional, respectively. The mixing ratio of HF exchange, c_X^{HF}, is known to significantly influence the results, and hybrid functionals with the same mixing ratio often yield similar outcomes. The fllowing are three commonly used hybrid functionals.

・B3LYP [24]

B3LYP exchange-correlation functional is the most widely used functionals in the quantum chemical calculations. The functional is written as follows:

$$E_{XC}^{B3LYP} = E_{XC}^{LDA} + a_1(E_X^{HF} - E_X^{LDA}) + a_2 E_X^{B88} + a_3(E_C^{LYP} - E_C^{LDA}), \tag{1.84}$$

where E_X^{LDA}, E_X^{B88}, E_C^{LYP} and E_C^{LDA} are the Slater exchange energy (1.59), the B88 exchange energy (1.77), the LYP correlation energy and the VWN correlation energy (1.71), respectively. The three parameters, a_1 = 0.2, a_2 = 0.72 and a_3 = 0.81 are determined to reproduce the physical properties of the G2 benchmark set [25], which consists of several dozen atoms and small molecules. The mixing ratio of HF exchange is a_1 = 0.2, i.e. 20 %.

・BHandHLYP [26]

Another hybrid functional using the Becke's exchange energy (1.77) and the LYP correlation energy is BHandHLYP,

$$E_{XC}^{BHandHLYP} = 0.5E_X^{HF} + 0.5E_X^{B88} + E_C^{LYP}. \tag{1.85}$$

This functional mixes the HF exchange energy and the GGA exchange energy at a 1:1 ratio, meaning

that the HF exchange component is 50 %. BHandHLYP has been reported to reproduce experimental values more accurately than B3LYP in the calculation of magnetism [27].

・PBE0 [28]

PBE0 functional is also a widely used hybrid functionals.

$$E_{XC}^{PBE0} = E_{XC}^{PBE} + 0.25(E_X^{HF} - E_X^{PBE}). \quad (1.86)$$

The mixing ratio of HF exchange is 25 %. This functional is based on the adiabatic connection and uses the PBE exchange-correlation functional as a reference. It is derived by expanding the energy difference between the exchange functional and the HF exchange integral as a perturbation and replacing one-fourth of the PBE exchange with the HF exchange integral in the third-order term of the expansion. Therefore, unlike B3LYP, it is a hybrid functional derived without using empirical parameters.

1.4 DFT calculation for periodic systems

In the HF and DFT calculations for atoms and isolated molecules, the physical properties of materials can be obtained by using the wavefunctions (or electron density). These molecular orbital calculations are performed using the localized (gaussian) basis sets like the LCAO-MO described in Equation (1.17). However, it is difficult to handle the electronic structures of systems with periodic boundary conditions, such as metals and crystals, using the localized basis sets. To handle periodic systems, band theory is commonly used. This approach uses plane-wave basis sets, which are particularly suited for describing the periodicity of the system. Additionally, the influence of core electrons is often replaced with effective potentials, such as pseudopotentials, to reduce computational cost while maintaining accuracy. Solid surfaces, interfaces, and isolated molecular systems can also be modeled using plane-wave basis sets by employing a slab model. In this approach, the computational target is periodically arranged within an enlarged unit cell, known as a supercell, with vacuum layers inserted to separate adjacent replicas of the target system. Furthermore, the autho describes the DFT+U method, which incorporates on-site Coulomb parameters U, as a technique for handling open-shell systems in the DFT calculations using plane-wave basis sets [29-32].

1.4.1 Lattice and reciprocal lattice

In crystals and supercells with periodic systems, the same unit cell repeats at each lattice point (Fig. I.1.1). The lattice vector $\boldsymbol{R}$ indicatingr the position of the lattice point (unit cell) is expressed using the basic translation vectors $\boldsymbol{a}_1$, $\boldsymbol{a}_2$, $\boldsymbol{a}_3$ as $\boldsymbol{R} = l_1\boldsymbol{a}_1 + l_2\boldsymbol{a}_2 + l_3\boldsymbol{a}_3$, where l_1, l_2, l_3 are integers. The unit cell can be taken as a parallelepiped with $\boldsymbol{a}_1$, $\boldsymbol{a}_2$, $\boldsymbol{a}_3$ as edges, and the atomic positions are given as $\boldsymbol{R} + \boldsymbol{t}_a$, where $\boldsymbol{t}_a$ is the relative position vector within the unit cell. In crystals and supercells, the potential term in the Kohn-Sham equation possesses translational symmetry, meaning that for any lattice vector $\boldsymbol{R}$, the

following condition holds:

$$v_{\text{eff}}(\boldsymbol{r} + \boldsymbol{R}) = v_{\text{eff}}(\boldsymbol{r}), \tag{1.87}$$

where v_{eff} is the Kohn-Sham potential consisting of the sum of the Coulomb attraction with the atomic nuclei, the Coulomb repulsion with the electrons, and the exchange-correlation potential. The potential is repeated identically for each unit cell.

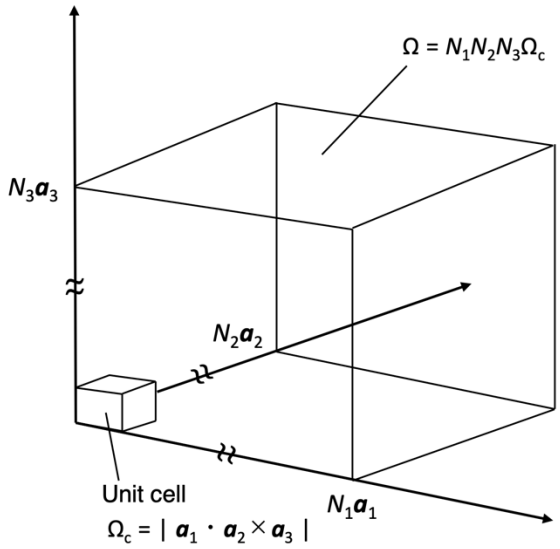

Fig. I.1.1. The arrangement of unit cells in a crystal and the Born-von Karman periodic boundary conditions. The unit cell (with volume Ω_c) repeats periodically along the basic translation vectors $\boldsymbol{a}_1$, $\boldsymbol{a}_2$, $\boldsymbol{a}_3$. On the other hand, the crystal region with a volume Ω, which spans $N_1\boldsymbol{a}_1$, $N_2\boldsymbol{a}_2$, $N_3\boldsymbol{a}_3$ in three directions, is assumed to repeat further beyond its boundaries under the Born-von Karman boundary conditions.

On the other hand, the primitive reciprocal lattice vectors, which correspond to the real-space lattice, are defined as follows:

$$\boldsymbol{b}_1 = 2\pi \frac{\boldsymbol{a}_2 \times \boldsymbol{a}_3}{\boldsymbol{a}_1 \cdot (\boldsymbol{a}_2 \times \boldsymbol{a}_3)}, \tag{1.88}$$

$$\boldsymbol{b}_2 = 2\pi \frac{\boldsymbol{a}_3 \times \boldsymbol{a}_1}{\boldsymbol{a}_1 \cdot (\boldsymbol{a}_2 \times \boldsymbol{a}_3)}, \tag{1.89}$$

$$\boldsymbol{b}_3 = 2\pi \frac{\boldsymbol{a}_1 \times \boldsymbol{a}_2}{\boldsymbol{a}_1 \cdot (\boldsymbol{a}_2 \times \boldsymbol{a}_3)}, \tag{1.90}$$

and these vectors satisfy a relationship,

$$\boldsymbol{a}_i \cdot \boldsymbol{b}_j = 2\pi\delta_{ij}. \tag{1.91}$$

The reciprocal lattice space ($\boldsymbol{k}$-space) is defined as a space where the reciprocal lattice vectors $\boldsymbol{G} = m_1\boldsymbol{b}_1 + m_2\boldsymbol{b}_2 + m_3\boldsymbol{b}_3$ (where m_1, m_2, m_3 are integers) repeat periodically. In this case, the dot product

with the lattice vector is expressed as

$$\boldsymbol{G} \cdot \boldsymbol{R} = 2\pi M, \quad M\text{: integer.} \tag{1.92}$$

The parallelepiped formed by the fundamental reciprocal lattice vectors $\boldsymbol{b}_1$, $\boldsymbol{b}_2$, $\boldsymbol{b}_3$ represents a unit cell of the reciprocal lattice, but in its original form, it does not fully reflect the symmetry of the reciprocal lattice. To address this, a region is constructed by bisecting the space with planes equidistant from the origin and its neighboring reciprocal lattice points. This region has a volume equal to that of the unit cell in the reciprocal lattice and incorporates the symmetry of the reciprocal lattice. This region is called the Brillouin zone. The volume of the unit cell in real space is given by the parallelepiped formed by $\boldsymbol{a}_1$, $\boldsymbol{a}_2$, $\boldsymbol{a}_3$ as $\Omega_c = |\boldsymbol{a}_1 \cdot \boldsymbol{a}_2 \times \boldsymbol{a}_3|$. Correspondingly, the volume of the Brillouin zone in reciprocal space, formed by $\boldsymbol{b}_1$, $\boldsymbol{b}_2$, $\boldsymbol{b}_3$, is $|\boldsymbol{b}_1 \cdot \boldsymbol{b}_2 \times \boldsymbol{b}_3| = 2\pi^3\Omega_c^{-1}$. As the unit cell volume Ω_c increases, the volume of the Brillouin zone decreases.

1.4.2 Bloch's theorem

In periodic systems characterized by lattice vectors $\boldsymbol{R}$ and reciprocal lattice vectors $\boldsymbol{G}$ (systems with translational symmetry), solving the Kohn-Sham equations is referred to as band structure calculations. According to Bloch's theorem, the eigenfunctions of a periodic system always have a wave vector $\boldsymbol{k}$, which corresponds to a wave (propagating in the direction of $\boldsymbol{k}$ with a wavelength 2π / $|\boldsymbol{k}|$), and $\boldsymbol{k}$ is confined within the Brillouin zone. Moreover, the eigenfunctions take the following form:

$$\phi_{\boldsymbol{k}n} = e^{i\boldsymbol{k}\cdot\boldsymbol{r}} u_{\boldsymbol{k}n}(\boldsymbol{r}), \tag{1.93}$$

where $u_{\boldsymbol{k}n}(\boldsymbol{r})$ is a lattice-periodic function, and for any lattice translation vector $\boldsymbol{R}$, it satisfies the translational symmetry condition:

$$u_{\boldsymbol{k}n}(\boldsymbol{r} + \boldsymbol{R}) = u_{\boldsymbol{k}n}(\boldsymbol{r}). \tag{1.94}$$

And n is a band index, and for each $\boldsymbol{k}$-point, several eigenstates are calculated based on the number of electrons per unit cell, and these eigenstates are labeled with the index n in ascending order of energy. From Equation (1.93), the contribution of the eigenstate $\phi_{\boldsymbol{k}n}(\boldsymbol{r})$ to the electron density distribution in Equation (1.45), $|\phi_{\boldsymbol{k}n}(\boldsymbol{r})|^2$, eliminates the exponential term and becomes $|U_{\boldsymbol{k}n}(\boldsymbol{r})|^2$. Furthermore, from Equation (1.94), this distribution is also a lattice periodic function.

The reason for constructing reciprocal lattice vectors and the Brillouin zone from lattice vectors is that the eigenstates of electrons in periodic systems are identified by $\boldsymbol{k}$, and solving for the eigenvalues and eigenfunctions at all $\boldsymbol{k}$-points within the Brillouin zone completely determines the electronic structure. By combining Equations (1.87), (1.93), and (1.94) with the KS equation (1.50), the KS equation for periodic systems takes a form dependent on $\boldsymbol{k}$. The eigenvalues $E_{\boldsymbol{k}n}$ and eigenfunctions $\phi_{\boldsymbol{k}n}$ are solved for each $\boldsymbol{k}$-point. The obtained $E_{\boldsymbol{k}n}$ and $\phi_{\boldsymbol{k}n}$ change gradually as $\boldsymbol{k}$ varies, and can be regarded as continuous functions of $\boldsymbol{k}$. A continuous set of eigenstates within the Brillouin zone corresponding to a specific band index n is referred to as a "band." When multiple bands overlap, the values of n may interchange. The variation of $E_{\boldsymbol{k}n}$ with respect to $\boldsymbol{k}$ within the Brillouin zone is called

the band structure (or band dispersion).

The Brillouin zone contains densely distributed ***k***-points. The number of ***k***-points in the Brillouin zone is, in principle, the same as the number of unit cells in the entire periodic system. Under the macroscopic periodic boundary condition depicted in Figure 1.1 (Born–von Karman periodic condition), the unit cell repeats in the $\boldsymbol{a}_1$, $\boldsymbol{a}_2$ and $\boldsymbol{a}_3$ directions with sizes of $N_1\boldsymbol{a}_1$, $N_2\boldsymbol{a}_2$ and $N_3\boldsymbol{a}_3$, respectively. The total crystal volume is given as $\Omega = N\Omega_c$, where $N = N_1N_2N_3$ and N is a macroscopic number. The total translational degrees of freedom N correspond to the number of ***k***-points defined in the system. Therefore, the Brillouin zone accommodates 2N states (electrons) per band, including spin. Two electrons per unit cell always fill a single band (the entire Brillouin zone); in the case of spin polarization, one electron fills one band.

1.4.3 Pseudopotential method

In solid-state electronic structure calculations, the construction of basis functions presents significant challenges. This is due to the coexistence of an extremely deep potential field near the atomic nucleus and a relatively flat potential field in the interatomic regions (Fig. I.1.2). Focusing on the region near the atomic nucleus, (i) ϕ, which represents atomic orbital-like basis functions as solutions to the deep spherical symmetric field, can be considered. On the other hand, (ii) ψ, which uses plane-wave basis functions to describe the extended free-electron-like characteristics in the flat interatomic regions, can be utilized. However, the (i) case faces difficulties in representing the interatomic regions, while the (ii) case encounters challenges in accurately describing the areas near the atomic nucleus.

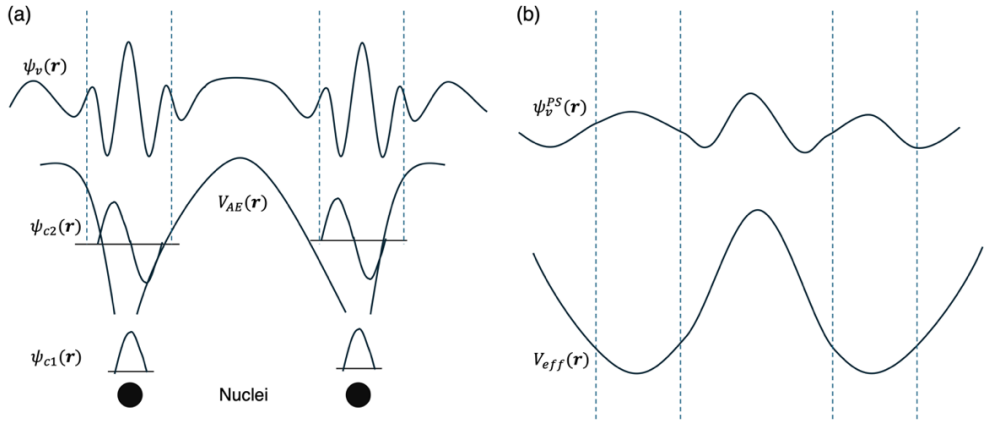

Fig. I.1.2. (a) Conceptual diagram of the all-electron potential $V_{AE}(\boldsymbol{r})$ and eigenstate wavefunctions (core orbitals ψ_{c1}, ψ_{c2}, and valence band wavefunction ψ_v) in a solid (crystal). (b) By introducing a "pseudopotential" that smoothens the potential within a cutoff radius r_c, oscillations in the valence wavefunction ψ_v near the atomic nucleus are removed. Outside the radius r_c, the pseudopotential ensures that the valence wavefunction and the all-electron potential accurately reproduce the correct valence electron properties.

As shown in Fig. I.1.2 (a), the valence wavefunction ψ_v is smooth in the interatomic region but exhibits oscillations near the atomic nucleus. These oscillations arise due to the orthogonality requirement with the core orbital ψ_c ($\int \phi_v^*(\boldsymbol{r})\phi_c(\boldsymbol{r})\, d\boldsymbol{r} = 0$). To represent wavefunctions with significant local variations using a plane-wave basis, a large number of short-wavelength plane waves are required, leading to an enormous computational size. On the other hand, methods that bridge (i) and (ii) have also been proposed, such as (iii), which constructs basis functions that are atomic orbital-like (spherical wave expansion) near the atomic nucleus and connect these to plane waves in the interatomic regions.

First-principles band calculation methods have been developed across several categories:

(i) LCAO-based methods:

First-principles approaches using the linear combination of atomic orbitals (LCAO), including hybrid basis methods [33].

(ii) Plane-wave pseudopotential methods:

These employ plane-wave basis sets and include the norm-conserving pseudopotential (NCPP) method [34,35], ultrasoft pseudopotential (USPP) method [36], and the projector augmented wave (PAW) method [37,38].

(iii) Linearized methods:

These include full-potential linearized augmented plane wave (FLAPW) methods and full-potential linear muffin-tin orbital (FP-LMTO) methods [39]. This category offers the highest accuracy, as it handles all electrons from core orbitals to valence bands (hence often referred to as “all-electron methods”), but the high computational cost is a notable drawback.

Here, the author explains the methods in category (ii). The three approaches—NCPP, USPP, and PAW—were developed sequentially, with newer methods achieving improvements in both efficiency and accuracy. Therefore, the author primarily focuses on explaining the foundational NCPP method. When dividing the region of each atom where the wave functions of core orbitals exist into an inner and outer region using a cutoff radius r_c , the effective potential $V_{\mathrm{eff}}(\boldsymbol{r})$ for each region is considered. Inside r_c, near the atomic nucleus, $V_{\mathrm{eff}}(\boldsymbol{r})$ is a deep spherical symmetric potential similar to that of a free atom, and the core orbitals, such as ψ_{c1} and ψ_{c2} shown in Fig. I.1.2, form low-energy eigenstates in crystals as they do in free atoms. These core orbitals do not directly contribute to interatomic bonding. Additionally, the Coulomb potential of other atomic nuclei is screened by the electrons near those nuclei. On the other hand, in the interatomic region outside r_c, only valence electrons are present, and $V_{\mathrm{eff}}(\boldsymbol{r})$ effectively represents the potential experienced by the valence electrons. This potential consists of the Coulomb field of the positively charged ion, screened by the core electrons, and the electrostatic and exchange potentials generated by the valence electrons both inside and outside r_c.

The wave function of the valence band (ψ_v in Fig. I.1.2) changes smoothly outside r_c, making it suitable for plane-wave basis expansion. However, as mentioned earlier, it oscillates (with nodes) inside r_c due to orthogonality with the core orbitals. The presence of a deep potential and core orbitals inside the r_c sphere is the origin of these oscillations. To address this, core orbitals are excluded from electronic structure calculations, and only valence electrons are considered. By introducing an "artificial potential" that has a shallower well inside r_c but matches the true all-electron potential $V_{\mathrm{AE}}(\boldsymbol{r})$ outside r_c, density functional theory calculations can be performed with the focus on valence electrons (Fig. I.1.2(b)). The process can be considered as follows:

(a) By "raising the bottom" of the potential inside r_c, a smooth, non-oscillating, and delocalized valence electron wave function can be generated.

(b) Ensuring that the integral of $|\psi_v|^2$ (norm) for the valence wave function inside r_c is preserved correctly for each atom allows the potential outside r_c to accurately reproduce the true all-electron potential $V_{\mathrm{AE}}(\boldsymbol{r})$.

(c) This setup should enable the correct valence wave function obtained from all-electron calculations to be reproduced outside r_c.

(d) The raised potential inside r_c and the elimination of wave function oscillations should compensate each other, potentially allowing the eigenvalues (energy levels) to be accurately reproduced.

The atom-specific potential that satisfies these requirements is referred to as the pseudopotential. Instead of using $V(\boldsymbol{r})$, which represents the sum of the Coulomb potentials from the atomic nuclei, the sum of the pseudopotentials $V_{\mathrm{PS}}(\boldsymbol{r})$ for each atom is utilized. Under this framework, density functional theory (DFT) calculations for the valence electron system alone are performed by solving the Kohn–Sham equations using the following effective potential,

$$V_{\mathrm{eff}}(\boldsymbol{r}) = V_{\mathrm{PS}}(\boldsymbol{r}) + V_{\mathrm{H}}(\boldsymbol{r}) + \mu_{\mathrm{xc}}(\boldsymbol{r}), \tag{1.95}$$

where $V_{\mathrm{H}}(\boldsymbol{r})$ and $\mu_{\mathrm{xc}}(\boldsymbol{r})$ are the electrostatic potential and the exchange-correlation potential, respectively, derived from the valence electron distribution under the pseudopotential framework. $V_{\mathrm{PS}}(\boldsymbol{r})$ is sum of pseudopotentials $V_{\mathrm{a}}^{\mathrm{PS}}$ from all atoms (with internal coordinates $\boldsymbol{t}_{\mathrm{a}}$) in all unit cells of the periodic system $\boldsymbol{R}$:

$$V_{\mathrm{PS}}(\boldsymbol{r}) = \sum_{\boldsymbol{R}} \sum_{a} V_a^{\mathrm{PS}}(\boldsymbol{r} - \boldsymbol{t}_a - \boldsymbol{R}). \tag{1.96}$$

$V_{\mathrm{a}}^{\mathrm{PS}}$ is preconstructed for each atomic species a and acts only on the valence electrons. Inside the cutoff radius r_c, it is adjusted upwards, while outside r_c, it becomes the Coulomb potential of the positively charged ion with the valence electrons removed. Thus, under the potential field described by Equation (1.95), the valence electron wavefunctions are smooth and free of oscillations (nodes) both inside and outside r_c (as shown in Fig. I.1.2), enabling expansion using plane-wave basis functions. Equation (1.95) describes a potential field in the interatomic region composed of the Coulomb field of the

positive ions and the contributions from $V_H(\boldsymbol{r}) + \mu_{xc}(\boldsymbol{r})$ due to the valence electrons. If the norm of the valence electron wavefunctions inside each atomic r_c-sphere is preserved to match the correct values from all-electron calculations, this pseudopotential can be considered equivalent to the full all-electron potential $V_{AE}(\boldsymbol{r})$ in the interatomic regions.

The calculated valence electron wavefunction is accurate in the interatomic region outside r_c, but within r_c, the nodes are removed, making it incorrect (as shown in Fig. I.1.2). Therefore, this wavefunction is referred to as the pseudo wavefunction. To correct the inaccuracies in the wavefunction within r_c, methods such as the USPP method and the PAW method have been developed. In the USPP method, condition (a) of the pseudopotential construction criteria (a)-(d) mentioned earlier is relaxed, allowing the smooth potential and extended wavefunction outside r_c to be assumed within r_c as well. This method significantly reduces the number of plane-wave basis functions required.

The PAW method, building upon the USPP method, combines it with the all-electron method (iii), resulting in further improvements in computational accuracy. While handling pseudo wavefunctions that do not have nodes near the atomic nucleus, in the expression of total energy and the Hamiltonian, the portion within the radius r_c of each atomic sphere is replaced with the correct valence wave function that possesses nodes (see Fig. I.1.2(a)). As a result, variational calculations using plane-wave basis can be performed efficiently with a relatively small number of plane waves, similar to the USPP method. Ultimately, this approach enables the accurate reconstruction of the correct valence wave functions with nodes near the atomic nucleus, leading to highly precise total energy calculations. In the PAW method, the valence electron wavefunction in a solid is treated as follows: first, a potential is constructed by adding the electrostatic potential $V_H(\boldsymbol{r})$ and the exchange-correlation potential $\mu_{xc}(\boldsymbol{r})$ from the valence electron distribution to the potential outside the cutoff radius r_c . Under this potential, a pseudo-wave function $\phi_{\boldsymbol{kn}}^{PS}(\boldsymbol{r})$ is handled using a plane-wave basis expansion. This pseudo wavefunction does not have nodes inside r_c but reproduces the correct wave function in the interatomic region outside r_c. The true wavefunction form $\phi_{\boldsymbol{kn}}(\boldsymbol{r})$ is obtained by modifying the pseudo wavefunction $\phi_{\boldsymbol{kn}}^{PS}(\boldsymbol{r})$ within the spherical region r_c of each atom as follows:

$$\phi_{\boldsymbol{kn}}(\boldsymbol{r}) = \phi_{\boldsymbol{kn}}^{PS}(\boldsymbol{r}) + \sum_i \left(|\phi_i\rangle - |\widetilde{\phi}_i\rangle\right)\langle\widetilde{p}_i|\,\phi_{\boldsymbol{kn}}^{PS}(\boldsymbol{r}). \tag{1.97}$$

The second term on the right-hand side represents the modification operation within the r_c sphere. The summation over i runs over the valence electron states of each atom, where $i = (l, m, \tau)$. The functions $|\phi_i\rangle$, $|\widetilde{\phi}_i\rangle$, and $|\widetilde{p}_i\rangle$ are atomic orbital-like functions (or operators) centered at each atomic position. For each element, two functions ($\tau = 1, 2$) are assigned to each valence orbital angular momentum l. $|\phi_i\rangle$ represents an expansion basis that correctly describes the electronic structure within the r_c sphere. It is an all-electron (AE) partial wave, constructed as the product of the radial wave function obtained from an all-electron calculation of a free atom and a spherical harmonic function. $|\widetilde{\phi}_i\rangle$ represents the pseudo (PS) partial wave, which corresponds to each AE partial wave. It is constructed such that:

・Outside the r_c sphere, it smoothly connects to the radial wavefunction of $|\phi_i\rangle$.

・Inside the r_c sphere, it is a smooth pseudo radial wavefunction that does not have nodes.

This pseudo wavefunction is appropriately designed to ensure computational efficiency while retaining the necessary accuracy in electronic structure calculations. The final form is obtained by multiplying the pseudo radial wavefunction with a spherical harmonic function. Projectors $|\widetilde{p}_i\rangle$ corresponding to each $|\phi_i\rangle$ also takes the form of a radial function multiplied by the spherical harmonic function.

The accuracy and reliability of a series of plane-wave-based first-principles calculation methods, including the NCPP, USPP, and PAW method, are fundamentally ensured by the treatment of valence electron behavior inside and outside the cutoff radius r_c of atomic spheres, based on all-electron orbital calculations of free atoms. Since the free atom calculation assumes a spherically symmetric potential, it allows for variable separation, enabling the execution of one-dimensional radial equations with relative ease. This systematic approach facilitates the construction of pseudopotentials, partial waves, and projectors, ensuring high accuracy in practical electronic structure calculations.

1.4.4 Cut-off energy

By Fourier expanding the lattice periodic function $u_{\boldsymbol{k}n}(\boldsymbol{r})$ in Equation (1.94), Equation (1.93) becomes:

$$\phi_{\boldsymbol{k}n}(\boldsymbol{r}) = e^{i\boldsymbol{k}\cdot\boldsymbol{r}}u_{\boldsymbol{k}n}(\boldsymbol{r}) = e^{i\boldsymbol{k}\cdot\boldsymbol{r}}\sum_{\boldsymbol{G}} u_{\boldsymbol{k}n}(\boldsymbol{G})e^{i\boldsymbol{G}\cdot\boldsymbol{r}} = \sum_{\boldsymbol{G}} u_{\boldsymbol{k}n}(\boldsymbol{G})e^{i(\boldsymbol{k}+\boldsymbol{G})\cdot\boldsymbol{r}}, \tag{1.98}$$

where $u_{\boldsymbol{k}n}(\boldsymbol{G})$ is Fourier expanding coefficient. Equation (1.98) can be regarded as a plane-wave basis expansion, where $e^{i(\boldsymbol{k}+\boldsymbol{G})\cdot\boldsymbol{r}}$ represents the plane-wave basis and $u_{\boldsymbol{k}n}(\boldsymbol{G})$ corresponds to the expansion coefficients. The summation is taken over $\boldsymbol{G}$, which changes while fixing $\boldsymbol{k}$ (restricted to the first Brillouin zone).

On the other hand, under the Born–von Karman periodic boundary conditions, where the unit cell repeats with periodicities $N_1\boldsymbol{a}_1$, $N_2\boldsymbol{a}_2$, $N_3\boldsymbol{a}_3$ along the directions of $\boldsymbol{a}_1$, $\boldsymbol{a}_2$, $\boldsymbol{a}_3$, respectively, forming a crystal volume Ω, the plane-wave basis normalized to a probability of 1 is considered:

$$|\boldsymbol{k}+\boldsymbol{G}\rangle = \Omega^{-\frac{1}{2}}e^{i(\boldsymbol{k}+\boldsymbol{G})\cdot\boldsymbol{r}}. \tag{1.99}$$

And then, the basis is

$$\phi_{\boldsymbol{k}n}(\boldsymbol{r}) = \sum_{\boldsymbol{G}} \Omega^{\frac{1}{2}}u_{\boldsymbol{k}n}(\boldsymbol{G})|\boldsymbol{k}+\boldsymbol{G}\rangle = \sum_{\boldsymbol{G}} C^n_{\boldsymbol{k}+\boldsymbol{G}}|\boldsymbol{k}+\boldsymbol{G}\rangle, \tag{1.100}$$

where $\{C^n_{k+G} = \Omega^{1/2}u_{\boldsymbol{k}n}(\boldsymbol{G})\}$ is a eigen vector. In a plane-wave basis expansion, the reciprocal lattice vector $\boldsymbol{G}$ starts from $\boldsymbol{G} = 0$, and the expansion includes all plane waves up to a certain cut-off energy E_{cut}. This cut-off energy is defined as:

$$\frac{\hbar^2}{2m}|\boldsymbol{k}+\boldsymbol{G}|^2 \leq E_{\text{cut}}, \tag{1.101}$$

This corresponds to specifying the lower limit of the wavelength in the plane-wave basis. From this

condition, the total number of plane wave bases N_G is determined. N_G dictates the computational load (the size of the Hamiltonian matrix is $N_G \times N_G$). If the wave function has no nodes and is smooth (and the pseudopotential is shallow and smooth), a smaller E_{cut} suffices, thereby reducing N_G. Typically, the shape of the pseudopotential for each element determines the value of E_{cut}.

1.4.5 DFT+*U* method

In plane-wave basis sets, describing systems with localized spins, such as those involving magnetic materials or strongly correlated electrons, is challenging due to the inherently delocalized nature of the basis functions. To address this issue, hybrid-DFT, as discussed in Section 1.3.7, can be considered. However, hybrid-DFT calculations may become impractical in terms of computational cost in certain cases. As another approach for the calculation of open-shell systems, DFT+*U* method is frequently employed [40-42]. This method introduces an on-site Coulomb interaction parameter *U* to account for electron correlation effects that are inadequately described by standard DFT calculations. The total energy based on the Hubbard model is given as follows:

$$E_{\text{tot}} = E_{\text{DFT}} + \frac{U - J}{2} \sum_{\sigma} (n_{i\sigma} - {n_{i\sigma}}^2), \tag{1.102}$$

where E_{DFT} represents the calculated energy by DFT methods, U is the on-site Coulomb repulsion, J represents the exchange interaction, n is the atomic-orbital occupation number, i is the orbital momentum and σ is a spin index. In the Hubbard model, the U term inherently includes exchange interactions; therefore, it is common to set $J = 0$. U is generally applied to strongly correlated d-orbitals or f-orbitals. The combination of plane-wave basis sets and the DFT+*U* method allows for efficient and accurate analysis of electronic structures in complex periodic systems.

Chapter 2. Electron transport for single molecule

Electron transport in single molecule or molecular scale devices is different from that of silicon-based devices with continuous energy levels, as single molecules possess discrete energy levels. Since controlling the junction between molecules and electrodes in experiments remains challenging, theoretical approaches are crucial for understanding conduction within molecules. This section provides an overview of general quantum transport concepts and a method for calculation of electron conduction in single molecule[43].

2.1 Quantum transport theory

2.1.1 Landauer formula

Let us consider a ballistic conductor with a single conduction channel. A ballistic conductor is defined as a conductor whose length is shorter than the mean free path of electrons. Here, electron-electron interactions and temperature effects are neglected. The model is depicted in Fig. I.2.1. The chemical potentials of the electrode 1 and electrode 2 are μ_1 and μ_2 ($\mu_1 > \mu_2$), respectively, with a voltage $V = (\mu_1 - \mu_2)/e$ applied between the electrodes. The conductor is assumed to be connected to the electrodes via ideal leads (L_1, L_2) that satisfy the following conditions:

1. The states in L_1 are occupied only by electrons coming from the electrode 1, and the chemical potential is μ_1.
2. The states in L_2 are occupied only by electrons coming from the electrode 2, and the chemical potential is μ_2.
3. Electrodes 1 and 2 are sufficiently large, ensuring that the current always maintains thermal equilibrium.

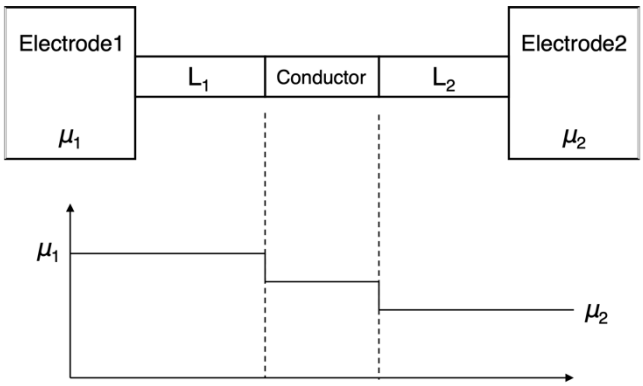

Fig. I.2.1. A model of a ballistic conductor connected to two electrodes.

At 0 K, the current arises within the energy range between μ_1 and μ_2. The current $I_1{}^+$ generated by electrons flowing from L_1 is given as follows:

$$I_1^+ = \frac{2e}{h}[\mu_1 - \mu_2]. \tag{2.1}$$

When the average probability of electrons transported from L_1 to L_2 is $\mathcal{T}$, then the outflow from L_2 is given by the inflow from L_1 multiplied by the transition probability $\mathcal{T}$. Thus:

$$I_2^+ = \frac{2e}{h}\mathcal{T}[\mu_1 - \mu_2]. \tag{2.2}$$

And then, the remining electrons returns to L_1, and it can be expressed as follows:

$$I_1^- = \frac{2e}{h}(1-\mathcal{T})[\mu_1 - \mu_2]. \tag{2.3}$$

Therefore, the net current I and conductance g are given as follows:

$$I = I_1^+ - I_1^- = I_2^+ = \frac{2e}{h}\mathcal{T}[\mu_1 - \mu_2], \tag{2.4}$$

$$g = \frac{I}{V} = \frac{I|e|}{(\mu_1 - \mu_2)} = \frac{2e^2}{h}\mathcal{T}. \tag{2.5}$$

If $\mathcal{T}$=1, the conductance g = 77.4 μS, which is referred to as the quantum conductance. This indicates that the conductance of the ballistic conductor with a single conduction channel is 77.4 μS, and it cannot exceed this value. In the Landauer model, the conductance depends on the interface between the conductor and the electrodes, and the resistance is therefore referred to as contact resistance. Consequently, the conductance expressed in Equation (2.5) represents the contact resistance. The interface between the leads and the conductor depends on the transition probability $\mathcal{T}$.

2.1.2 Landauer formula at finite temperature

At finite temperature, the average number of electrons is obtained from the Fermi distribution,

$$f_0(E-\mu) = \frac{1}{1+\exp\left(\frac{E-\mu}{k_B T}\right)}. \tag{2.6}$$

$f(E-\mu)$ represents the probability that an energy state E is occupied by an electron at an absolute temperature T. The Fermi distribution applies to indistinguishable particles in thermal equilibrium, specifically, those that obey Pauli exclusion principle. Based on this, the electron inflow from lead 1 and lead 2 can be expressed as follows, respectively:

$$i_1^+(E) = \frac{2e}{h}f_1(E), \tag{2.7}$$

$$i_2^-(E) = \frac{2e}{h}f_2(E). \tag{2.8}$$

On the other hand, the electron outflow from lead 1 and lead 2 can be expressed as follows:

$$i_1^-(E) = (1-\mathcal{T})i_1^+(E) + \mathcal{T}'i_2^-(E), \tag{2.9}$$

$$i_2^+(E) = \mathcal{T}i_1^+(E) + (1-\mathcal{T}')i_2^-(E). \tag{2.10}$$

Therefore, the current flowing through the device $i(E)$ is given by

$$
\begin{aligned}
i(E) &= i_1^+ - i_1^- \\
&= i_2^+ - i_2^- \\
&= \mathcal{T} i_1^+ - \mathcal{T}' i_2^- \\
&= \frac{2e}{h}[\mathcal{T}(E) f_1(E) - \mathcal{T}'(E) f_2(E)].
\end{aligned} \tag{2.11}
$$

If $\mathcal{T}(E) = \mathcal{T}'(E)$, the total current is written as

$$
I = \int i(E) dE, \tag{2.12}
$$

where

$$
i(E) = \frac{2e}{h} \mathcal{T}(E)[f_1(E) - f_2(E)]. \tag{2.13}
$$

When the system is no longer in equilibrium, the applied bias voltage could change the two transmission functions and make them unequal, so generally $\mathcal{T}(E) \neq \mathcal{T}'(E)$. However, if inelastic scattering is assumed to be absent within the device, $\mathcal{T}(E) = \mathcal{T}'(E)$ always holds for a two-terminal devices.

When the deviation from equilibrium is small, the current is proportional to the applied bias voltage. Equation (2.13) is given by

$$
\delta I = \frac{2e}{h} \int \left([\mathcal{T}(E)]_{eq} \delta[f_1 - f_2] + [f_1 - f_2]_{eq} \delta[\mathcal{T}(E)] \right) dE. \tag{2.14}
$$

Since $f_1(E) = f_2(E)$ at equilibrium state, the second term is zero. The first term is written by using the Taylor expansion,

$$
\begin{aligned}
\delta[f_1 - f_2] &\approx [\mu_1 - \mu_2] \left(\frac{\partial f}{\partial \mu} \right)_{eq} \\
&= \left(-\frac{\partial f_0}{\partial E} \right) [\mu_1 - \mu_2].
\end{aligned} \tag{2.15}
$$

Thus, the linear response formula at finite temperature is obtained

$$
\begin{aligned}
g &= \frac{e}{(\mu_1 - \mu_2)} \delta I \\
&= \frac{2e^2}{h} \int \mathcal{T}(E) \left(-\frac{\partial f_0}{\partial E} \right) \\
&= \frac{2e^2}{h k_B T} \int \mathcal{T}(E)\, f_0(E)[1 - f_0(E)] dE.
\end{aligned} \tag{2.16}
$$

2.1.3 Multi-channel case

The Landauer model quantizes the conductance of a one-dimensional conductor, where the conductance of a ballistic conductor with a single conduction channel is given by g = 77.4 μS. When

multiple conduction channels are present, the sum of the transition probabilities for each channel is expressed as the total transition probability,

$$g = \frac{2e^2}{h}\sum_{i,j}\mathcal{T}_{i,j}, \tag{2.17}$$

where $\mathcal{T}_{i,j}$ represents the transition probability of the transmission from channel *i* to *j*.

In each channel, incoming and outgoing waves are moving. Let us consider a system where two conduction channels, 1 and 2, are connected as illustrated in Fig. I.2.2.

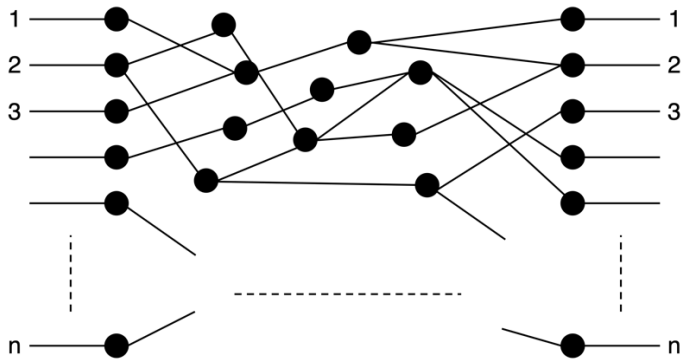

Fig. I.2.2. The model of multi-channel system.

The wavefunctions in channels 1 and 2 are represented by the following plane waves:

$$\psi_1 = a_1 e^{ikx} + b_1 e^{ikx}, \tag{2.18}$$

$$\psi_2 = a_2 e^{ikx} + b_2 e^{ikx}. \tag{2.19}$$

For simplicity, the same *k* is used for channels 1 and 2, however, it is generally different. From the Schrödinger equation, there is a linear relationship between the amplitudes of the incoming wave (a_1,a_2) and outgoing wave (b_1,b_2). Thus,

$$b_1 = ra_1 + t'a_2, \tag{2.20}$$

$$b_2 = ta_1 + r'a_2, \tag{2.21}$$

where (*r*,*t*) is the left side of the matrix of the reflection coefficient, and (*r*',*t*') is the right side of the matrix of the transmission coefficient. Equation (2.20) and (2.21) are rewritten as following:

$$\boldsymbol{b} = \boldsymbol{S}\boldsymbol{a}, \quad \boldsymbol{S} = \begin{pmatrix} r & t' \\ t & r' \end{pmatrix}. \tag{2.22}$$

The unitary matrix $\boldsymbol{S}$ is called *S*-matrix. The *S*-matrix is often used in order to calculate $\mathcal{T}_{i,j}$ in Equation (2.17). At each energy, a coherent conductor is characterized by the *S*-matrix that relates the amplitudes of the outgoing waves to the incoming waves in different leads.

To generalize the above concept, one coherent conductor and count all the channels through which electrons can move id considered. The transition probability $\mathcal{T}_{m\leftarrow n}$ is obtained by taking the square of the corresponding element of the *S*-matrix.

$$T_{m\leftarrow n} = |s_{m\leftarrow n}|^2 \tag{2.23}$$

The arrow in the subscript is introduced to indicate the direction of transition, from the second subscript to the first.

2.1.4 Current density

The Landauer formula is the method that calculates the conductance or current between the electrodes and conductor. In this section, the author derives the Landauer formula from a different approach. In an equilibrium state without an applied bias voltage, the current does not flow because the amplitudes of the waves traveling in the left and right directions are equal. When the voltage difference is applied between the left and right electrodes, current begins to flow. The general problem is shown in Fig. I.2.3 for a tunneling barrier. Considering that a real device is three-dimensional system, assuming that the flowing direction of the tunneling current is z-direction, and split of z-direction into perpendicular direction against it. When the electron transport in z-direction is treated as the tunneling process, the transport in perpendicular direction does not affect the tunneling process because it is regarded as free-electron movement. The energy of z-direction is written as

$$E_z = \frac{\hbar^2 k_{lz}^2}{2m} = \frac{\hbar^2 k_{rz}^2}{2m} + constant, \tag{2.24}$$

where k_{lz} and k_{rz} are the z-components of the wave vector for a region of the left and right side of the barrier, respectively. The constant depends on the applied voltage and takes negative value when the potential of the right electrode is positive. The derivative of Equation (2.24) corresponds to the velosity,

$$v_z(k_{lz}) = \frac{1}{\hbar}\frac{dE_z}{dk_{lz}}, \tag{2.25}$$

$$v_z(k_{rz}) = \frac{1}{\hbar}\frac{dE}{dk_{rz}}. \tag{2.26}$$

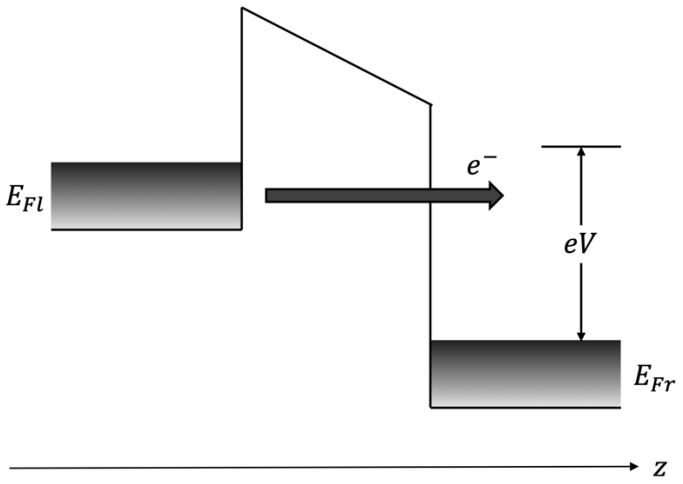

Fig. I.2.3. Band diagram for the tunneling barrier under the bias voltage

The current through the barrier depends on the tunneling probability and the number of electrons contributing to the tunneling. Therefore, the current density flowing from the left to right is

$$J_{LR} = e \int D(\boldsymbol{k})\, v_z(k_{lz}) \mathcal{T}(k_{lz}) f(E_L) d^3\boldsymbol{k}, \quad D(\boldsymbol{k}) = \frac{2}{(2\pi)^3}. \tag{2.27}$$

$f(E_L)$ is the Fermi distribution function on the left side of the barrier, $D(\boldsymbol{k})$ is the density of state in $\boldsymbol{k}$-space, and $\mathcal{T}(k_{lz})$ is the transition probability. Similarly, the current density from the right to left is

$$J_{RL} = e \int D(\boldsymbol{k})\, v_z(k_{rz}) \mathcal{T}(k_{rz}) f(E_R) d^3\boldsymbol{k}. \tag{2.28}$$

If the energy of the left side electrode is equal to that of the right side electrode, the transition probability on the left side becomes equal to that on the right side, resulting $\mathcal{T}(k_{lz}) = \mathcal{T}(k_{rz})$. From Equation (2.27) and (2.28),

$$\begin{aligned} J &= e \int D(\boldsymbol{k})\, v_z(k_z) \mathcal{T}(k_z) [f(E_L) - f(E_R)] d^3\boldsymbol{k} \\ &= \int D(\boldsymbol{k})\, v_z(k_z) \mathcal{T}(k_z) [f(E_L) - f(E_L + eV)] d^3\boldsymbol{k}. \end{aligned} \tag{2.29}$$

In order to simplify, the energy of the left barrier can be divided into the energy in the z-direction E_z and the energy in the perpendicular direction $E_\perp$, then:

$$E = E_z + E_\perp, \tag{2.30}$$

$$d^3\boldsymbol{k} = d^2k_\perp dk_z. \tag{2.31}$$

Here, the differential dk_z can be rewritten as the derivative of the z-direction energy E_z,

$$k_z = \left(\frac{dE}{dk_z}\right)^{-1} \frac{dE}{dE_z} dE_z, \tag{2.32}$$

$$\frac{dE}{dk_z} = \frac{\hbar^2 k_z}{m} = \hbar v_z. \tag{2.33}$$

Also,

$$\begin{aligned} d^2k_\perp &= 2\pi k_\perp dk_\perp \\ &= \left(\frac{2\pi m}{\hbar^2}\right) dE_\perp, \end{aligned} \tag{2.34}$$

where

$$k_\perp dk_\perp = \frac{m}{\hbar^2} dE_\perp.$$

Therefore, Equation (2.29) can be rewritten as follows:

$$J = \frac{4\pi em}{(2\pi)^3 \hbar} \int_0^\infty \mathcal{T}(E_z)\, dE_z \int_0^\infty [f(E_z + E_\perp) - f(E_z + E_\perp + eV)]\, dE_\perp$$

$$= \frac{emk_BT}{2\pi^2\hbar^3}\int_0^\infty \mathcal{T}(E_z)\ln\left(\frac{1+e^{\frac{E_F^l-E_z}{k_BT}}}{1+e^{\frac{E_F^l+eV-E_z}{k_BT}}}\right)dE_z, \tag{2.35}$$

where E_F^l is the Fermi energy on the left side, and the logarithmic term is called the supply function.

2.2 Single-molecule electron conductivity using elastic scattering Green's function method

The electrical conductivity of single molecules is evaluated not only through experimental measurements but also through theoretical calculations. Two primary calculation methods are used: the elastic scattering Green's function (ESGF) method [44] and the non-equilibrium Green's function (NEGF) method [45]. By combining these methods with Hartree-Fock or DFT calculations, it becomes possible to predict the conductivity of single molecules based on the quantum chemical calculations. This section discusses the theory behind conductivity calculations based on the ESGF method.

2.2.1 Scattering theory[46]

Electric current is generated by the movement of electrons, and describing it requires addressing the scattering of particles. Scattering processes can be broadly classified into two categories: those in which energy is conserved before and after scattering, and those in which energy loss occurs. The former is referred to as elastic scattering, while the latter is called inelastic scattering. In the following discussion, the author focuses on elastic scattering. In scattering theory, the Schrödinger equation is replaced with the Lippmann-Schwinger equation as follows, and the discussion is developed based on this formulation.

$$|\psi^{\pm}\rangle = |\phi\rangle + \hat{G}_0^{\pm}\hat{V}|\psi^{\pm}\rangle, \tag{2.36}$$

where $|\psi^{\pm}\rangle$ and $|\phi\rangle$ represent the scattered state and incident state, respectively, $\hat{V}$ is the interaction with the scatterer, and $\hat{G}_0^{\pm}$ is the Green's function without the interaction. By defining the transition operator $\hat{T}$ as the operator that connects the incident state and scattered state, the following equation can be obtained

$$\hat{T}|\phi\rangle = \hat{V}|\psi^{\pm}\rangle. \tag{2.37}$$

By using the transition operator $\hat{T}$, Equation (2.36) can be rewritten as

$$|\psi^{\pm}\rangle = |\phi\rangle + \hat{G}_0^{\pm}\hat{T}|\phi\rangle, \tag{2.38}$$

and then, the transition operator $\hat{T}$ can be represented by Equation (2.37) and (2.38) as follows:

$$\hat{T} = \hat{V} + \hat{V}\hat{G}_0^{\pm}\hat{T}. \tag{2.39}$$

Expanding Equation (2.39) sequentially, it becomes the following equation

$$\hat{T} = \hat{V} + \hat{V}\hat{G}_0^{\pm}\hat{V} + \hat{V}\hat{G}_0^{\pm}\hat{V}\hat{G}_0^{\pm}\hat{V} + \cdots. \tag{2.40}$$

By applying the Born approximation and neglecting higher-order terms, the following result can be obtained

$$\hat{T} = \hat{V} + \hat{V}\hat{G}_0^{\pm}\hat{V}. \tag{2.41}$$

From Equation (2.41), in the scattering theory, the transition operator can be obtained by the interaction with the scatterer and the Green's function.

2.2.2 Formulation of electron conductivity by using ESGF method

The single-molecule electron conductivity can be considered based on the molecular orbitals. At first, Mujica et al. formularized the single-molecule electron conductivity evaluation method based on the elastic scattering method [47-49]. Luo et al. improved the method to a simple model by using the (1) overlap matrix elements, (2) the anchor atoms connected to the electrodes and (3) the probabilities that the electron is present at the anchor atoms in LUMO[44,50,51].

First, the Hamiltonian of the system H is defined as follows,

$$H = H_M + H_L + H_R + U, \tag{2.42}$$

$$H_M = \sum_{\sigma=\pm}\sum_{\alpha} E^0_{\alpha\sigma}\,|\alpha_\sigma\rangle\langle\alpha_\sigma| \equiv \sum_{\sigma=\pm}\sum_{\alpha} E^0_{\alpha\sigma}\,C^*_{\alpha\sigma I}C_{\alpha\sigma J}|I\rangle\langle J|, \tag{2.43}$$

$$H_L = \sum_{\sigma=\pm}\sum_{i} E^0_{i\sigma}\,|i_\sigma\rangle\langle i_\sigma|, \tag{2.44}$$

$$H_R = \sum_{\sigma=\pm}\sum_{j} E^0_{j\sigma}\,|j_\sigma\rangle\langle j_\sigma|, \tag{2.45}$$

$$U = \sum_{\sigma=\pm}\sum_{I}\left(\sum_{i}\gamma_{iI,\sigma}|i_\sigma\rangle\langle I| + \sum_{j}\gamma_{jI,\sigma}|j_\sigma\rangle\langle I|\right) + \text{complex conjugate}, \tag{2.46}$$

where H_M, $H_{L(R)}$ represent the Hamiltonians of the molecule and the left (right) electrode, respectively; U is the interaction potential between the molecule and the electrodes; and $\gamma_{iI,\sigma}$ is the interaction between the I-th site of the molecule and the i-th orbital of the electrodes with spin σ (= α or β).

In the ESGF method, the transition operator is defined as follows,

$$\hat{\mathcal{T}} = U + UGU. \tag{2.47}$$

G is the Green's function,

$$G = \frac{1}{z - H}, \tag{2.48}$$

where z is a complex variable. Assuming that the electrodes only interact directly with the end-sites, (site 1 and M) of the molecule (see Fig. I.2.4), the transition matrix element can be written as

$$\hat{\mathcal{T}}_{ij,\sigma} = \gamma_{i1,\sigma}G_{1M,\gamma}\gamma_{Nj,\sigma}, \tag{2.49}$$

$$G_{1M,\gamma} = \sum_{\eta}\left\langle 1\left|\frac{1}{z-H}\right|\phi^\eta_\sigma\right\rangle\langle\phi^\eta_\sigma|M\rangle$$

$$= \sum_{\eta} \frac{\langle 1|\phi_\sigma^\eta\rangle\langle\phi_\sigma^\eta|M\rangle}{z-\varepsilon_\sigma^\eta}$$
$$\approx \sum_{\eta} \frac{\langle 1|\phi_\sigma^\eta\rangle\langle\phi_\sigma^\eta|M\rangle}{z-\tilde{\varepsilon}_\sigma^\eta}, \quad (2.50)$$

where ϕ_σ^η is the eigenstate of the total Hamiltonian H, i.e. $H|\phi_\sigma^\eta\rangle = \varepsilon_\sigma^\eta|\phi_\sigma^\eta\rangle$. Here, the end-sites are defined as the terminal atoms connected to the electrodes, the eigenstate η that overlaps with end-sites only contributes to the matrix elements in the Green's function . Therefore, $|\phi_\sigma^\eta\rangle$ can be approximated by orbitals obtained from the Kohn-Sham equation for the finite systems consisting of the molecule sandwiched the electrodes ($\tilde{H}|\phi_\sigma^\eta\rangle = \tilde{\varepsilon}_\sigma^\eta|\phi_\sigma^\eta\rangle$) [44].

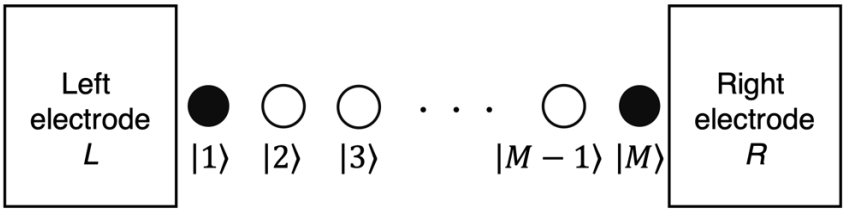

Fig. I.2.4. Model of the finite system consisting of the molecule sandwiched the electrodes. This model is referred to as the extended molecule.

In the linear response theory, a static carrier conduction i^{LR} of the system that are applied the bias voltage V_D by right and left electrodes is given as

$$i_\sigma^{LR} = \frac{1}{2}\sum_{\eta} \frac{emk_BT}{2\pi^2\hbar^3} \int_{eV_D}^{\infty} \left|\hat{\mathcal{T}}_\sigma(E)\right|_\eta^2 f_\sigma(E)dE, \quad (2.51)$$

$$f_\sigma(E) = \left\{\ln\left[1+\exp\left(\frac{E_{F,\sigma}+eV_D-E}{k_BT}\right)\right] - \ln\left[1+\exp\left(\frac{E_{F,\sigma}-E}{k_BT}\right)\right]\right\}, \quad (2.52)$$

where T is the temperature of the system and $f_\sigma(E)$ represents the Fermi distribution. $E_{F,\sigma}$ is the Fermi energy that is defined as the intermediate value between the orbital energies of the HOMO and LUMO of the extended molecule. Assuming that the interactions between the different scattering channels are negligible because the spacing between the molecular orbitals is large enough, then the transition probability is written as

$$\left|\hat{\mathcal{T}}_\sigma(E)\right|_\eta^2 = \gamma_{L1,\sigma}^2\gamma_{MR,\sigma}^2 \sum_{\eta} \frac{\left|\langle 1|\phi_\sigma^\eta\rangle\right|^2\left|\langle\phi_\sigma^\eta|M\rangle\right|^2}{\left(\tilde{\varepsilon}_\sigma^\eta - E\right)^2 + \Gamma_{\eta,\sigma}^2}, \quad (2.53)$$

where $\Gamma_{\eta,\sigma}^2$ denote the spin-depend escape rate determined by the Fermi's golden rule,

$$\Gamma_{\eta,\sigma} = \frac{\gamma_{L1,\sigma}\langle 1|\phi_\sigma^\eta\rangle + \gamma_{MR,\sigma}\langle\phi_\sigma^\eta|M\rangle}{2}. \quad (2.54)$$

$\langle 1|\phi_\sigma^\eta\rangle$ and $\langle\phi_\sigma^\eta|M\rangle$ represent the site-orbital overlap matrix elements between the end-sites and the

extended molecule. The product of the two site-orbital overlap matrixes, $\left|\langle 1|\phi_\sigma^\eta\rangle\right|^2\left|\langle\phi_\sigma^\eta|M\rangle\right|^2$, represents delocalization of the molecular orbitals of the extended molecule, which is called site-overlap.

γ is called the coupling constant between the molecule and electrodes. Luo et al. proposed that the occupied molecular orbitals of the electrodes interact with the LUMO of the bare molecule without electrodes based on the frontier orbital theory[44,50]. Therefore, the coupling constant γ between the left electrode and site 1 of the molecule with subscripts L and 1 is written as

$$\gamma_{L1,\sigma}(\mathrm{LUMO}) = V_{L,\sigma}(\mathrm{LUMO})d_{1,\sigma}(\mathrm{LUMO}), \tag{2.55}$$

$$V_{L,\sigma}^2(\mathrm{LUMO}) = \frac{\left(\Delta E_{\sigma,\mathrm{HOMO-LUMO}} - \Delta E_{\sigma,\mathrm{LUMO}}\right)\Delta E_{\sigma,\mathrm{LUMO}}}{2}, \tag{2.56}$$

$$d_{1,\sigma}^2(\mathrm{LUMO}) = \frac{\sum_i c_{1,i,\sigma}^2}{\sum_{a,i} c_{a,i,\sigma}^2}, \tag{2.57}$$

where $V_{L,\sigma}(\mathrm{LUMO})$ is the interaction between the HOMO of the electrodes and the LUMO of the bare molecule, and $\Delta E_{\sigma,\mathrm{LUMO}}$ is the energy difference between them. $\Delta E_{\sigma,\mathrm{HOMO\text{-}LUMO}}$ is the HOMO-LUMO gap of the extended molecule and $d_{1,\sigma}(\mathrm{LUMO})$ is the ratio of the ratio of the electron density at end-site 1 to that of the entire molecule. In other words, $V_{L,\sigma}(\mathrm{LUMO})$ is the strength of the junction between the molecule and electrodes, and $d_{1,\sigma}(\mathrm{LUMO})$ express the degree of transmission from the electrode to the molecule. Therefore, $\gamma_{L1,\sigma}(\mathrm{LUMO})$ represents the coupling strength of the junction between the left electrode and site 1, and determines the electron conductivity derived from the electron transfer between them. Equations (2.55)-(2.57) also hold between the end-site M and the right electrode with subscripts M and R.

In the systems where the LUMO of the molecules is non-degenerate, Equations (2.55)-(2.57) can be applied; however, these equations cannot be applied to systems where the LUMO of the molecules is degenerate. Nakanishi et al. extended the method to the degenerated or quasi-degenerated systems by using the Boltzmann distribution[52]. Assuming that Equation (2.56) does not change in the degenerated systems, Equations (2.55)-(2.57) can be written as follows:

$$\gamma_{L1,\sigma} = V_{L,\sigma}d_{1,\sigma}^*, \tag{2.58}$$

$$V_{L,\sigma} \approx V_{L,\sigma}(\mathrm{LUMO}), \tag{2.59}$$

$$d_{1,\sigma}^2 = \frac{\sum_k \exp[-(E_{\mathrm{LUMO}+k} - E_{\mathrm{LUMO}})/RT]\, d_{\mathrm{LUMO}+k}}{\sum_k \exp[-(E_{\mathrm{LUMO}+k} - E_{\mathrm{LUMO}})/RT]}$$

$$= \frac{\sum_k B_k\, d_{\mathrm{LUMO}+k}}{\sum_k B_k}, \tag{2.60}$$

where k is the number of orbitals degenerate with the LUMO, and B_k is the Boltzmann distribution. If $k = 0$, Equations (2.58)-(2.60) are equivalent to Equations (2.55)-(2.57).

The total current density I^{LR} is finally calculated as Ai^{LR}, where A is the effective injection area of the electron transmitted from the electrodes. A can be approximated that πr_s^2, where $r_s = [3/(4\pi n)]^{1/3}$

is defined as the radius of a sphere with the same volume as an electron. Also, n is the density of the electron, which is assumed in the three-dimensional free-electron model [50] as:

$$n = \frac{\left(2mE_{F,\sigma}\right)^{\frac{3}{2}}}{(3\pi^2\hbar^3)}.$$

Chapter 3. Estimation of molecular magnetism and correction of spin contamination

In systems with open-shell electronic states, such as strongly correlated systems, magnetism arises from the interactions between localized spins. By estimating these magnetic interactions, it becomes possible to predict stable spin states. Calculation methods for open-shell electronic states, such as UHF and UDFT-based Broken-Symmetry (BS) methods, are commonly used; however, it is known that BS methods introduce errors referred to as spin contamination [1]. This section explains calculation methods for magnetic interactions corrected for spin contamination, namely the Yamaguchi method and the approximate spin projection method. Additionally, a method for optimizing molecular structures while correcting spin contamination using the approximate spin projection method is discussed [29].

3.1 Approximate spin projection method

In systems such as open-shell biradical molecules, a possibility of the different spin coupling states must be considered. In the case of biradical systems, the energy gap between the singlet (BS) and triplet states must be considered. Usually, the energy gap between those states can be discussed by using the effective exchange integrals (J_{ab}) in the Heisenberg Hamiltonian [54,55]. For example, the Heisenberg Hamiltonian for two spin-site system is

$$\hat{H} = -2J_{ab}\hat{\boldsymbol{S}}_a \cdot \hat{\boldsymbol{S}}_b, \tag{3.1}$$

where J_{ab} is the effective exchange integral between the localized spin site a and b, and $\hat{\boldsymbol{S}}_{a(b)}$ is the total spin operator at site $a(b)$. When considering two spins coupled in antiferromagnetic (AFM, also referred to as spin-polarized low spin (LS) state, which in this model is represented as a BS singlet) and ferromagnetic (FM, or high spin (HS) state, represented as a triplet) interactions, the total spin operator can be expressed as the sum of the spin operators at each spin site. In this case, Equation (3.1) is:

$$\hat{H} = -2J_{ab}(-\hat{\boldsymbol{S}}^2 + \hat{\boldsymbol{S}}_a{}^2 + \hat{\boldsymbol{S}}_b{}^2). \tag{3.2}$$

Thus, the energies in the Heisenberg model for singlet and triplet states are as follows

$$E^{\text{singlet}} = J_{ab}(-\langle\hat{\boldsymbol{S}}^2\rangle^{\text{singlet}} + \langle\hat{\boldsymbol{S}}_a{}^2\rangle^{\text{singlet}} + \langle\hat{\boldsymbol{S}}_b{}^2\rangle^{\text{singlet}}), \tag{3.3}$$

$$E^{\text{triplet}} = J_{ab}(-\langle\hat{\boldsymbol{S}}^2\rangle^{\text{triplet}} + \langle\hat{\boldsymbol{S}}_a{}^2\rangle^{\text{triplet}} + \langle\hat{\boldsymbol{S}}_b{}^2\rangle^{\text{triplet}}). \tag{3.4}$$

If the magnitude of the spin at each spin site remains the same for both the singlet and triplet states, the total spin interaction energy can be expressed as

$$E^{\text{singlet}} - E^{\text{triplet}} = J_{ab}(\langle\hat{\boldsymbol{S}}^2\rangle^{\text{triplet}} - \langle\hat{\boldsymbol{S}}^2\rangle^{\text{singlet}}). \tag{3.5}$$

Therefore,

$$J_{ab} = \frac{E^{\text{singlet}} - E^{\text{triplet}}}{\langle\hat{\boldsymbol{S}}^2\rangle^{\text{triplet}} - \langle\hat{\boldsymbol{S}}^2\rangle^{\text{singlet}}}. \tag{3.5}$$

By generalizing to arbitrary ferromagnetic coupling states (HS) and antiferromagnetic coupling states (LS), the energy expressions can be described as follows

$$J_{ab} = \frac{E_{\mathrm{BS}}^{\mathrm{LS}} - E^{\mathrm{HS}}}{\langle \widehat{\boldsymbol{S}}^2 \rangle^{\mathrm{HS}} - \langle \widehat{\boldsymbol{S}}^2 \rangle_{\mathrm{BS}}^{\mathrm{LS}}}, \tag{3.6}$$

where $E_{\mathrm{BS}}^{\mathrm{LS}}$ and E^{HS} represent the total energy of the LS and HS states calculated by the BS method. This is referred to as the effective exchange integral (J) value calculated by the approximate spin projection (AP) method. The denominator in the formula for the effective exchange integral is always positive, and considering that the molecule's energy corresponds to the energy difference between the HS state and the LS state, the energy takes a negative value. Therefore, if $J_{ab} < 0$, the LS states is more stable than the HS states; if $J_{ab} > 0$, the HS states is more stable than LS states. The electronic structures with localized spins are often calculated by using the BS method. This method can approximate the spin-polarized electronic structures of the open-shell systems at low cost of calculations, however it has a problem called the spin contamination error. The spin contamination is an error that the electronic structure of the lower spin multiplicity (such as the LS state) is contaminated by the electronic states of higher spin multiplicity (such as the HS state) [1]. The spin contamination error is usually not negligible in the systems with larger spin-polarization. Equation (3.6) is called Yamaguchi's approach to calculate J_{ab} values with the AP procedure [56-37].

To apply the Yamaguchi equation to the results of the plane-wave calculations, it is necessary to determine the total spin angular momentum $\langle \widehat{\boldsymbol{S}}^2 \rangle^{\mathrm{Y}}$ (Y means the spin states and Y = LS or HS) in the context of the plane-wave calculations. Wang et al. proposed that $\langle \widehat{\boldsymbol{S}}^2 \rangle^{\mathrm{Y}}$ can be estimated using the electron density [59],

$$\langle \widehat{\boldsymbol{S}}^2 \rangle^{\mathrm{Y}} = \langle \widehat{\boldsymbol{S}}^2 \rangle_{exact}^{\mathrm{Y}} - {\rho_{\mathrm{Y}}}^{-}(r), \tag{3.7}$$

$${\rho_{\mathrm{Y}}}^{-}(r) = \begin{cases} {\rho_{\mathrm{Y}}}^{\alpha}(r) - {\rho_{\mathrm{Y}}}^{\beta}(r) & \text{when } {\rho_{\mathrm{Y}}}^{\alpha}(r) < {\rho_{\mathrm{Y}}}^{\beta}(r) \\ 0 & \text{when } {\rho_{\mathrm{Y}}}^{\alpha}(r) \geq {\rho_{\mathrm{Y}}}^{\beta}(r) \end{cases}, \tag{3.8}$$

where ${\rho_{\mathrm{Y}}}^{\alpha}(r)$ and ${\rho_{\mathrm{Y}}}^{\beta}(r)$ are the density of the up and down spins for the spin states Y, respectively. By substituting $\langle \widehat{\boldsymbol{S}}^2 \rangle^{\mathrm{Y}}$ defined in Equations (3.7) and (3.8) into Yamaguchi equation (3.6), the effective exchange integrals J_{ab} in plane-wave calculations can be obtained. For a system where two spins are coupled (LS = singlet, HS = triplet), J_{ab} is given as follows,

$$J_{ab} = \frac{E^{\mathrm{LS}} - E^{\mathrm{HS}}}{2 + \int {\rho_{\mathrm{LS}}}^{-}(r)dr - \int {\rho_{\mathrm{HS}}}^{-}(r)dr}. \tag{3.9}$$

3.2 Geometry optimization with AP method

J_{ab} value calculated by Equation (3.6) should be equal to J_{ab} value calculated by the spin-projected wavefunctions because the spin contamination error ($J_{ab}\langle \widehat{\boldsymbol{S}}^2 \rangle_{\mathrm{BS}}^{\mathrm{LS}}$) is approximately eliminated, i.e.

$$J_{ab} = \frac{E_{\mathrm{BS}}^{\mathrm{LS}} - E_{\mathrm{BS}}^{\mathrm{HS}}}{\langle \widehat{\boldsymbol{S}}^2 \rangle_{\mathrm{BS}}^{\mathrm{HS}} - \langle \widehat{\boldsymbol{S}}^2 \rangle_{\mathrm{BS}}^{\mathrm{LS}}} = \frac{E_{\mathrm{APBS}}^{\mathrm{LS}} - E_{\mathrm{APBS}}^{\mathrm{HS}}}{\langle \widehat{\boldsymbol{S}}^2 \rangle_{exact}^{\mathrm{HS}} - \langle \widehat{\boldsymbol{S}}^2 \rangle_{exact}^{\mathrm{LS}}}, \tag{3.10}$$

where $E_{\mathrm{APBS}}^{\mathrm{LS}}$ and $E_{\mathrm{APBS}}^{\mathrm{HS}}$ are the total energy of the LS and the HS state with the AP procedure, respectively. In the HS state, the spin contamination is usually negligible, therefore,

$$\langle \widehat{\boldsymbol{S}}^2 \rangle_{\mathrm{BS}}^{\mathrm{HS}} \cong \langle \widehat{\boldsymbol{S}}^2 \rangle_{exact}^{\mathrm{HS}}, \qquad E_{\mathrm{BS}}^{\mathrm{HS}} \cong E_{\mathrm{APBS}}^{\mathrm{HS}}. \tag{3.11}$$

The spin-projected energy $E_{\mathrm{APBS}}^{\mathrm{LS}}$ is then written as

$$E_{\mathrm{APBS}}^{\mathrm{LS}} = \alpha E_{\mathrm{BS}}^{\mathrm{LS}} - \beta E_{\mathrm{BS}}^{\mathrm{HS}}, \tag{3.12}$$

where

$$\alpha = \frac{\langle \widehat{\boldsymbol{S}}^2 \rangle_{\mathrm{BS}}^{\mathrm{HS}} - \langle \widehat{\boldsymbol{S}}^2 \rangle_{exact}^{\mathrm{LS}}}{\langle \widehat{\boldsymbol{S}}^2 \rangle_{\mathrm{BS}}^{\mathrm{HS}} - \langle \widehat{\boldsymbol{S}}^2 \rangle_{\mathrm{BS}}^{\mathrm{LS}}}, \tag{3.13}$$

$$\beta = \frac{\langle \widehat{\boldsymbol{S}}^2 \rangle_{\mathrm{BS}}^{\mathrm{LS}} - \langle \widehat{\boldsymbol{S}}^2 \rangle_{exact}^{\mathrm{LS}}}{\langle \widehat{\boldsymbol{S}}^2 \rangle_{\mathrm{BS}}^{\mathrm{HS}} - \langle \widehat{\boldsymbol{S}}^2 \rangle_{\mathrm{BS}}^{\mathrm{LS}}}, \tag{3.14}$$

$$\beta = \alpha - 1. \tag{3.15}$$

To perform the geometry optimization by using the AP method, an energy gradient of $E_{\mathrm{APBS}}^{\mathrm{LS}}$ is required [60,61]. Taylor expansion of Equation (3.12) is written as

$$E_{\mathrm{APBS}}^{\mathrm{LS}}(\boldsymbol{R}_{\mathrm{APBS}}^{\mathrm{LS}}) = E_{\mathrm{APBS}}^{\mathrm{LS}}(\boldsymbol{R}) + \boldsymbol{X}^T \boldsymbol{G}_{\mathrm{APBS}}^{\mathrm{LS}}(\boldsymbol{R}) + \frac{1}{2}\boldsymbol{X}^T \boldsymbol{F}_{\mathrm{APBS}}^{\mathrm{LS}}(\boldsymbol{R})\boldsymbol{X}, \tag{3.16}$$

where $\boldsymbol{G}_{\mathrm{APBS}}^{\mathrm{LS}}(\boldsymbol{R})$ and $\boldsymbol{F}_{\mathrm{APBS}}^{\mathrm{LS}}(\boldsymbol{R})$ are a gradient and a hessian of $E_{\mathrm{APBS}}^{\mathrm{LS}}(\boldsymbol{R})$, respectively. $\boldsymbol{R}_{\mathrm{APBS}}^{\mathrm{LS}}$ and $\boldsymbol{R}$ are a stationary point of and a present position, respectively, and $\boldsymbol{X} = \boldsymbol{R}_{\mathrm{APBS}}^{\mathrm{LS}} - \boldsymbol{R}$ is a position vector. $\boldsymbol{G}_{\mathrm{APBS}}^{\mathrm{LS}}(\boldsymbol{R}) = 0$ at the stationary point $\boldsymbol{R}_{\mathrm{APBS}}^{\mathrm{LS}}$, therefore $\boldsymbol{R}_{\mathrm{APBS}}^{\mathrm{LS}}$ can be obtained if $\boldsymbol{G}_{\mathrm{APBS}}^{\mathrm{LS}}(\boldsymbol{R})$ can be calculated.

From Equation (3.12), $\boldsymbol{G}_{\mathrm{APBS}}^{\mathrm{LS}}(\boldsymbol{R})$ can be written as

$$\boldsymbol{G}_{\mathrm{APBS}}^{\mathrm{LS}}(\boldsymbol{R}) = \frac{\partial E_{\mathrm{APBS}}^{\mathrm{LS}}(\boldsymbol{R})}{\partial \boldsymbol{R}}$$

$$= \left\{\alpha(\boldsymbol{R})\boldsymbol{G}_{\mathrm{BS}}^{\mathrm{LS}}(\boldsymbol{R}) - \beta(\boldsymbol{R})\boldsymbol{G}_{\mathrm{BS}}^{\mathrm{HS}}(\boldsymbol{R})\right\} + \frac{\partial \alpha(\boldsymbol{R})}{\partial \boldsymbol{R}}\left\{E_{\mathrm{BS}}^{\mathrm{LS}}(\boldsymbol{R}) - E_{\mathrm{BS}}^{\mathrm{HS}}(\boldsymbol{R})\right\}, \tag{3.17}$$

where $\boldsymbol{G}_{\mathrm{APBS}}^{\mathrm{Y}}(\boldsymbol{R})$ is the energy gradient calculated by the BS method for the spin state Y (Y: LS or HS). $\langle \widehat{\boldsymbol{S}}^2 \rangle_{\mathrm{BS}}^{\mathrm{HS}}$ is usually constant because the spin contamination of the HS state is negligible, so $\partial\alpha(\boldsymbol{R})/\partial\boldsymbol{R}$ is written as follows from Equation (3.13)

$$\frac{\partial \alpha(\boldsymbol{R})}{\partial \boldsymbol{R}} = \frac{\langle \widehat{\boldsymbol{S}}^2 \rangle_{\mathrm{BS}}^{\mathrm{HS}} - \langle \widehat{\boldsymbol{S}}^2 \rangle_{exact}^{\mathrm{LS}}}{\left(\langle \widehat{\boldsymbol{S}}^2 \rangle_{\mathrm{BS}}^{\mathrm{HS}} - \langle \widehat{\boldsymbol{S}}^2 \rangle_{\mathrm{BS}}^{\mathrm{LS}}\right)^2} \frac{\partial \langle \widehat{\boldsymbol{S}}^2 \rangle_{\mathrm{BS}}^{\mathrm{LS}}}{\partial \boldsymbol{R}}. \tag{3.18}$$

$\partial \langle \widehat{\boldsymbol{S}}^2 \rangle_{\mathrm{BS}}^{\mathrm{LS}} / \partial \boldsymbol{R}$ can be obtained from a numerical fitting [60] and the AP optimization is carried out by Equation (3.17) and (3.18).

The spin-projected hessian $\boldsymbol{F}_{\mathrm{APBS}}^{\mathrm{LS}}(\boldsymbol{R})$ can be used to estimate the spin contamination in IR spectra. $\boldsymbol{F}_{\mathrm{APBS}}^{\mathrm{LS}}(\boldsymbol{R})$ is written as

$$\boldsymbol{F}_{\mathrm{APBS}}^{\mathrm{LS}}(\boldsymbol{R}) = \frac{\partial^2 E_{\mathrm{APBS}}^{\mathrm{LS}}(\boldsymbol{R})}{\partial \boldsymbol{R}^2}$$

$$= \{\alpha(\boldsymbol{R})\boldsymbol{F}_{\mathrm{BS}}^{\mathrm{LS}}(\boldsymbol{R}) - \beta(\boldsymbol{R})\boldsymbol{F}_{\mathrm{BS}}^{\mathrm{HS}}(\boldsymbol{R})\} + 2\frac{\partial\alpha(\boldsymbol{R})}{\partial\boldsymbol{R}}\{\boldsymbol{G}_{\mathrm{BS}}^{\mathrm{LS}}(\boldsymbol{R}) - \boldsymbol{G}_{\mathrm{BS}}^{\mathrm{HS}}(\boldsymbol{R})\} + \frac{\partial^2\alpha(\boldsymbol{R})}{\partial\boldsymbol{R}^2}\{E_{\mathrm{BS}}^{\mathrm{LS}}(\boldsymbol{R}) - E_{\mathrm{BS}}^{\mathrm{HS}}(\boldsymbol{R})\} \quad (3.19)$$

where $\boldsymbol{F}_{\mathrm{APBS}}^{\mathrm{Y}}(\boldsymbol{R})$ is the hessian calculated by the BS method for the spin state Y (Y: LS or HS). We can obtain the IR spectra by diagonalizing $\boldsymbol{F}_{\mathrm{APBS}}^{\mathrm{LS}}(\boldsymbol{R})$.

Although $\partial\alpha(\boldsymbol{R})/\partial\boldsymbol{R}$ is necessary to calculate the AP gradient by Equation (3.17), most ab initio programs don't give us $\partial\alpha(\boldsymbol{R})/\partial\boldsymbol{R}$ value. For this issue, we used a numerical procedure based on the univariate method introduced by Kitagawa et al. [60,61].

References

1. A. Szabo, N. S. Ostlund, *MODERN QUANTUM CHEMISTRY: Introduction to Advanced Electron Structure Theory*, Reprint, Dover Publications, Mineola, New York, 1996.
2. D. R. Hartree, *Proc. Camb. Phil. Soc.*, **1928**, *24*, 111.
3. V. Fock, *Z. Physik*, **1930**, *61,* 126.
4. J. C. Slater, *Phys. Rev.*, **1929**, *34*, 1293.
5. T. Koopmans, *Physica*, **1934**, *1*, 104.
6. C. C. J. Roothaan, *Rev. Mod. Phys*., **1951**, *23*, 69.
7. J. A. Pople, R. K. Nesbet, *J. Chem. Phys.*, **1954**, *22*, 571.
8. W. Koch, M. C. Holthausen, *A Chemist's Guide to Density Functional Theory*, WILEY-VCH Verlag GmbH, Weinheim, 2001**.**
9. P. Hohenberg, W. Kohn, *Phys. Rev.*, **1964**, *136*, B864.
10. M. Levy, *Proc. Natl. Acad. Sci. U.S.A.*, **1979**, *76*, 6062.
11. W. Kohn, L. J. Sham, *Phys. Rev.*, **1965**, *140*, A1133.
12. R.G. Parr, W. Yang, *Density-Functional Theory of Atoms and Molecules*, Oxford University Press, New York, 1989.
13. S. H. Vosko, L. Wilk, M. Nusair, *Can. J. Phys.*, **1980**, *58,*1200.
14. J. P. Perdew, Y. Wang, *Phys. Rev. B*, **1992**, *45*, 13244.
15. A. D. Becke, *Phys. Rev. A*, **1988**, *38*, 3098.
16. J. P. Perdew, *Phys. Rev. B*, **1986**, *33*, 8822.
17. J. P. Perdew, K. Burke, M. Ernzerhof, *Phys. Rev. Lett.*, **1996**, *77*, 3865.
18. Y. Zhang, W. Yang, *Phys. Rev. Lett.*, **1998**, *80*, 890.
19. C. Lee, W. Yang, R. G. Parr, *Phys. Rev.* B, **1988**, *37*, 785.
20. R. Colle, O. Salvetti, *Theor. Chim. Acta*, **1975**, *37*, 329.
21. R. Colle, O. Salvetti, *Theor. Chim. Acta*, **1979**, *53*, 55.
22. B. Miehlich, A. Savin, H. Stoll, H. Preuss, *Chem. Phys. Lett*., **1989**, *157*, 200.

23. B. G. Johnson, P. M. W. Gill, J. A. Pople, *J. Chem. Phys.*, **1993**, *98*, 5612.
24. A. D. Becke, *J. Chem. Phys.*, **1993**, *98*, 5648.
25. L. A. Curtiss, K. Raghavachari, G. W. Trucks, J. A. Pople, *J. Chem. Phys.*, **1991**, *94*, 7221.
26. A. D. Becke, *J. Chem. Phys.*, **1993**, *98*, 1372.
27. Y. Kitagawa, T. Saito, K. Yamaguchi, in *Symmetry (Group Theory) and Mathematical Treatment in Chemistry*, T. Akitsu (Ed.), InTechOpen, London, 2018, pp. 121-139.
28. C. Adamo, V. Barone, *J. Chem. Phys.*, **1999**, *110*, 6158.
29. R. M. Martin, *Electronic Structure-Basic Theory and Practical Methods, 2nd edition*, Cambridge University Press, Cambridge, 2020.
30. M Kohyama, *Materia Japan*, **2022**, *61*, 588.
31. M Kohyama, *Materia Japan*, **2022**, *61*, 679.
32. M Kohyama, *Materia Japan*, **2022**, *61*, 782.
33. S. Ono, Y. Noguchi, R. Sahara, Y. Kawazoe, K. Ohno, C*omput. Phys. Commun.*, **2015**, *189,* 20.
34. D. R. Hamann, M. Schlüter, C. Chiang, *Phys. Rev. Lett.,* **1979**, *43*, 1494.
35. G. B. Bachelet, D. R. Hamann, M. Schlüter, *Phys. Rev. B*, **1984**, *26*, 4199.
36. D. Vanderbilt, *Phys. Rev. B*, **1990**, *41*, 7892.
37. P. E .Blöchl, *Phys. Rev. B*, **1994**, *50*, 17953.
38. G. Kresse, D. Joubert, *Phys. Rev. B*, **1999**, *59*, 1758.
39. O. K. Andersen, *Phys. Rev. B*, **1975**, *12*, 3060.
40. V. I. Anisimov, J. Zaanen, O. K. Andersen, *Phys. Rev. B*, **1991**, *44*, 943.
41. V. I. Anisimov, F. Aryasetiawan, A. I. Lichtenstein, *J. Phys. Condens. Matter.*, **1997**, *9*, 767.
42. S. L. Dudarev,G. A. Botton, S. Y. Savrasov, C. J. Humphreys, A. P. Sutton, *Phys. Rev. B*, **1998**, *57*, 1505.
43. S. Datta, *Electronic Transport in Mesoscopic Systems*, Cambridge University Press, Cambridge, 1995.
44. C. K. Wang, Y. Fu, Y. Luo, *Phys. Chem. Chem. Phys.*, **2001**, *3*, 5017.
45. M. Brandbyge, J.-L. Mozos, P. Ordejón, J. Taylor, K. Stokbro, *Phys. Rev. B*, **2002**, *65*, 165401.
46. J. R. Taylor, *Scattering Theory: The Quantum Theory of Nonrelativistic Collisions*, John Wiley and Sons, Inc., New York, 1972.
47. V. Mujica, G. Doyen, *Int. J. Quantum Chem.*, **1993**, *48*, 687.
48. V. Mujica, M. Kemp, M. A. Ratner, *J. Chem. Phys.*, **1994**, *101*, 6849.
49. V. Mujica, M. Kemp, M. A. Ratner, *J. Chem. Phys.*, **1994**, *101*, 6856.
50. Y. Luo, C. K. Wang, Y. Fu, *J. Chem. Phys.*, **2002**, *117*, 10283.
51. L. L. Lin, X. N. Song, Y. Luo, C. K. Wang, *J. Phys. Condens. Matter*, **2010**, *22*, 14474.
52. Y. Nakanishi, T. Matsui, Y. Kitagawa, Y. Shigeta, T. Saito, Y. Kataoka, T. Kawakami, M. Okumura, K. Yamaguchi, *Bull. Chem. Soc. Jpn*., **2011**, *288*, 366.

53. Y. Kitagawa, T. Saito, K. Yamaguchi, *Bull. Jpn. Soc. Coord. Chem.*, **2018**, *71,* 57.
54. D. Gatteschi, O. Kahn, J. S. Miller, F. Palacio, *Magnetic Molecular Materials*, Kluwer Academic Publishers, Dordrecht, 1991.
55. O. Kahn, *Magnetism: A Supermolecular Function*, NATO ASI Series C, Kluwer Academic Publishers, Dordrecht, 1996.
56. Y. Takahara, K. Yamaguchi, T. Fueno, *Chem. Phys. Lett*., **1989**, *157*, 211.
57. K. Yamaguchi, H. Fukui, T. Fueno, *Chem. Lett*. **1986**, 625.
58. K. Yamaguchi, Y. Takahara, T. Fueno, K. N. Houk, *Theor. Chim. Acta*, **1988**, *73,* 337.
59. J. H. Wang, A. D. Becke, V. H. Smith, *J. Chem. Phys.*, **1995**, *102*, 3477.
60. Y. Kitagawa, T. Saito, M. Ito, M. Shoji, K. Koizumi, S. Yamanaka, T. Kawakami, M. Okumura, K. Yamaguchi, *Chem. Phys. Lett.*, **2007**, *442*, 445.
61. Y. Kitagawa, T. Saito, M. Ito, Y. Nakanishi, M. Shoji, K. Koizumi, S. Yamanaka, T. Kawakami, M. Okumura, K. Yamaguchi, *Int. J. Quantum Chem.*, **2007**, *107*, 3094.

Part II

Relationship between open-shell electronic state and single-molecule electron conductivity

1. Introduction

To establish design guidelines for single-molecule components utilizing the open-shell electronic states, the selection of target molecular systems is crucial. In this study, the author focused on d-π conjugated compounds. In the molecular electronics, π-conjugated organic molecules are the first promising candidates for the single-molecule components/devices, because their delocalization of π-orbitals exhibit high electron conductivity. Various single-molecule components utilizing π-conjugated organic molecules have been reported to date [1-11]. In addition, d-π conjugated compounds, consist of organic ligands and metal ions, have also attracted attention as another candidate molecules [12-14]. They can exhibit both the high electron conductivity through the π-orbitals of the organic ligands and various functionalities due to the localized electrons in d-orbitals of the metal ions. Extended metal atom chains (EMACs) are one of the d-π conjugated compounds that involve the linearly aligned transition metal ions surrounded by the organic bridging ligands [15]. The EMACs are considered suitable for application as molecular wires because their one-dimensionally aligned metal ions resemble the structure of metal leads [16,17].

As describes in General Introduction, a development of the theoretical calculations for the strongly correlated systems have clarified the electronic structures of the d-π conjugated compounds [18-26]. For example, the DFT and multi-reference (MR) calculations have revealed the nature of the metal-metal bonds [18,21,24,25]. Additionally, the electron transportation in the EMACs have also been simulated based on the Green's function method, such as ESGF and NEGF methods [22-26]. It has been reported that the electron conductivities depend on their structures and electronic states [23].

From the viewpoint of the single-molecule components/devices, a relationship between the electronic/spin structure, magnetic property and electron conductivity of nickel EMACs has also examined based on the DFT and the ESGF methods [24-26]. The nickel EMACs have two types of nickel(II) ions i.e. terminal (high spin, $S = 1$) and inner (low spin, $S = 0$) ions, where S represents the magnitude of spins of the Ni(II) ion, and a difference in the electron conductivity by their spin coupling states between the terminal Ni(II) ions i.e. anti-ferromagnetic (AFM) and ferromagnetic (FM) coupling states was reported [24]. In addition, the FM state exhibited higher conductivity than the AFM state [25,26].

To further discuss the relationship, the author has focused on paddlewheel-type dinuclear complexes, whose structures are considered the smallest units of EMACs. Up to now, a lot of functional paddlewheel-type dinuclear complexes such as redox activity, optical property and electron conductivity have been reported [27-31]. Additionally, paddlewheel-type dichromium tetraacetate complexes have been reported to possess unique spin-polarized quadruple metal-metal bonds consisting of s-, p- and d-orbitals, and their electronic structures have been theoretically examined using the generalized valence bond (GVB) and MR methods [32-34]. Kitagawa et al. conducted a detailed study on a relationship between the molecular structure, electronic structure and effective

exchange integrals (*J*) of the dichromium tetraacetate complexes using the BS and AP methods (see the details in Part I, Chapter 3) [35]. The results indicated that the dichromium complexes have a ground state with a spin-polarized open-shell singlet electronic structure [36], which is preferable for the single-molecule transistors using the spin states. In addition, it was found that the BS method is a powerful tool for calculating *J* values and molecular structures of these complexes when the spin contamination error is corrected by the AP method [36,37].

In this study, therefore, the author investigated the electron conductivity of the paddlewheel-type dichromium(II,II) tetrabenzoate complex shown in Fig. II.1 using the BS-DFT with the AP method and ESGF method, whose detail was explained in Part I, Chapter 2. In addition, the author introduced substituents, such as electron-donating/withdrawing groups, into the bridging ligands (R in Fig. II.1(a)), and compared the electron conductivities between the AFM and FM states, as shown in Fig. II.1(b) to elucidate the relationship between the electronic structure, spin state and single-molecule electron conductivity in detail.

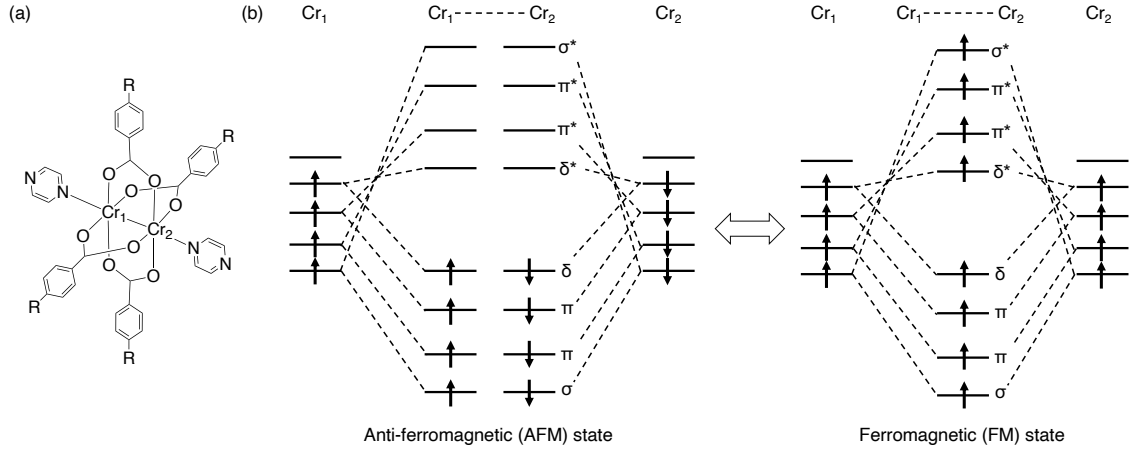

Fig. II.1. (a) Model structure of the paddlewheel-type dichromium(II,II) tetrabenzoate complex. **R** represents the positions where the substituents are introduced. (b) Electron configuration of d-orbitals of two Cr(II) ions for the anti-ferromagnetic (AFM) and ferromagnetic (FM) states. In these complexes, the AFM state corresponds to an open-shell singlet state formed by the d-orbitals of the chromium ions, while the FM state corresponds to a nonet state. In the figure, the upward and downward arrows represent α-spin and β-spin, respectively.

2. Computational Details

The dichromium(II,II) tetrabenzoate pyrazine complex was used as the basic framework, and several substituents were introduced into the benzoate ligands to examined the substitution effect. As electron-donating groups, OH and CH_3, and as electron-withdrawing groups, F, CN, and NO_2 were introduced into the R-parts of Fig. II.1(a) to compare with the non-substituted (R=H, abbreviated as

NS) complex. Hereafter, the complexes with substituents X are referred to as R(X). The structures of these complexes were based on the dichromium tetraacetate pyrazine complex [40].

The structures of the complexes in the AFM state were first optimized by B3LYP/6-31G* level of theory [41-43]. Since these complexes have the open-shell properties, the BS-DFT calculation was used to include the static electron correlation. To eliminate the spin contamination error in the BS-DFT results, the geometry of the Cr(II) ions was only reoptimized by the AP-optimization explained in Part I, Chapter 3.

The anchor nitrogen atoms of the axial pyrazine ligands were designed to bind to the on-top site of the Au(111) surface, as the nitrogen atoms are known to bind to the on-top sites of Au(111) [44,45]. To reduce the computational cost, the electrodes were approximated as gold dimers as shown in Fig. II.2, which reproduce the Fermi energy of the bulk gold [24].

On the complexes plus gold dimers (extended molecule), the electronic structure calculations were performed by BS-B3LYP/LANL2DZ [46](Au), 6-31G* (other atoms) level of theory for both the AFM and FM states. For all models, the total charge was neutral, and the spin multiplicities of the AFM and FM states were singlet and nonet, respectively.

The electron conductivity was calculated by the ESGF method, explained in Part I, Chapter 2, using the DFT calculation results. Assuming that the temperature was 300 K. The molecular orbitals contributing to the electron transition were considered within the range from LUMO+9 to HOMO−9. All DFT calculations were performed in the gas phase using Gaussian 09 Rev. D01 [47] and the electron conductivity was simulated using our self-developed program.

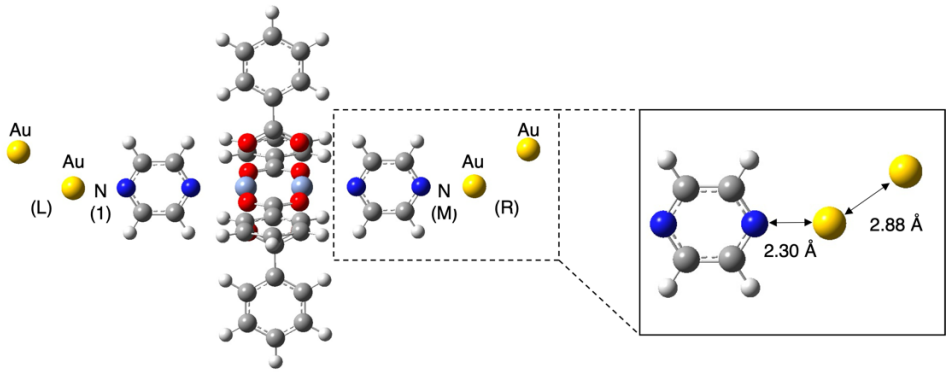

Fig. II.2. Illustration of the extended molecules of the NS complex. The labels 1 and M represent the end-sites of the complex, and L and R are the left and right electrodes, respectively. The Au-N distance and Au-Au distance were fixed to 2.30 Å and 2.88 Å, respectively [38,39].

3. Results and Discussion

3.1 Effect of substituents on the structure and electron conductivity of the complex in the AFM state

First, the author investigated the electron conductivity in the AFM state. Fig. II.3 shows a relationship between the calculated current values at 1.0 V (I_{AFM}) and the optimized Cr(II)-Cr(II) distances of the complexes. As shown in Fig. II.3, when the electron-donating groups (-OH and -CH_3) are introduced, the Cr(II)-Cr(II) distance becomes shorter and the electron conductivity of the complex becomes higher. On the other hand, in the case of introducing the electron-withdrawing groups (-F, -CN and -NO_2), the distance between Cr(II) ions is elongated and the electron conductivity becomes lower.

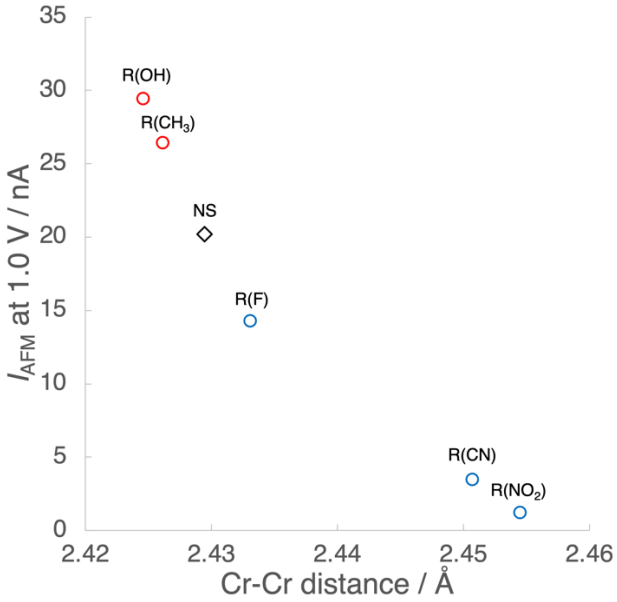

Fig. II.3. Calculated current values at 1.0 V versus the Cr(II)-Cr(II) distance of the optimized complexes in the AFM states. The red, blue and black markers represent the complexes with the electron-donating groups, electron-withdrawing groups and NS form, respectively.

I_{AFM} without the AP-optimization are shown in Fig. II.4, and significant changes were observed in the electron conductivities due to the Cr(II)-Cr(II) distances, suggesting the importance of eliminating the spin contamination error for the electron conductivity calculations in these systems. The optimized Cr(II)-Cr(II) distances, summarized in Table II.1, are slightly longer than the experimental results of the related complexes. The elongation can be attributed to the absence of packing effects in the crystal structure. It has been reported that the AP-B3LYP method reproduces the experimental Cr(II)-Cr(II) distance of paddlewheel-type dichromium(II,II) tetraacetate complexes well when the ligands are fixed to the X-ray structure [48,49]. In this study, however, the entire structure of the model complexes was fully optimized using the BS method in the gas phase, without considering crystal packing effects,

followed by the partial optimization of the Cr(II) ions. As a result, the molecular sizes were expanded. Indeed, the optimized axial molecular lengths, defined as the distance between the end-sites 1 and M (see Fig. II.2), are longer than the experimental values, as summarized in Table. II.2.

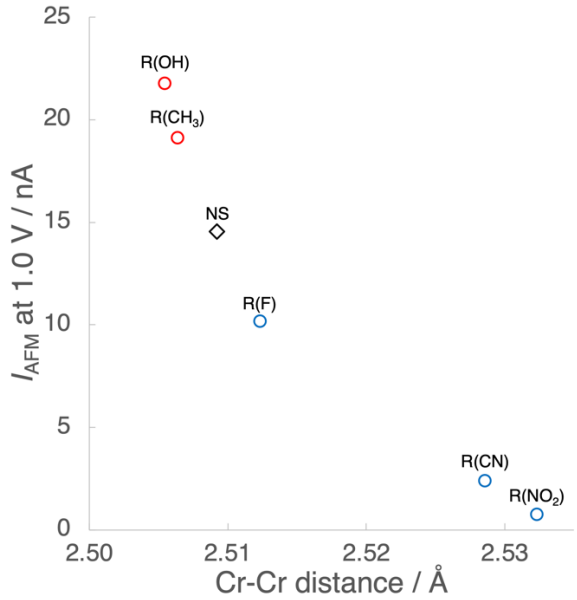

Fig. II.4. Calculated current values at 1.0 V versus the distance between the dichromium ions of the complexes without the AP-optimization in the AFM states. The red circle markers, the blue circle markers and the black diamond-shaped marker represent electron-donating groups, -withdrawing groups and NS form, respectively.

Table II.1. Cr-Cr distances optimized by BS- and AP-B3LYP methods. Experimental Cr-Cr distances of related complexes; $Cr_2(O_2CCH_3)_4(pyridine)_2$ (**1**) and $Cr_2(O_2CCH_3)_4(pyrazine)_2$ (**2**) are also summarized in the table from reference, respectively.

	Cr-Cr distance / Å	
	BS-B3LYP	AP-B3LYP
R(OH)	2.505	2.425
$R(CH_3)$	2.506	2.426
NS	2.509	2.429
R(F)	2.512	2.433
R(CN)	2.529	2.451
$R(NO_2)$	2.532	2.455
Complex **1** [40]	2.369	
Complex **2** [40]	2.295	

Table II.2. Axial molecular length of each complex, defined as the distance between the terminal atoms 1 and M, as shown in Fig. II.2. Since the AP-optimization was performed only for the Cr atoms, these lengths remain unchanged before and after the AP-optimization. Experimental distances of related complexes; $Cr_2(O_2CCH_3)_4(pyridine)_2$ (**1**) and $Cr_2(O_2CCH_3)_4(pyrazine)_2$ (**2**) are also summarized in the table from reference, respectively.

	Axial molecular length / Å
R(OH)	12.802
$R(CH_3)$	12.784
NS	12.786
R(F)	12.790
R(CN)	12.797
$R(NO_2)$	12.798
Complex **1** [40]	12.545
Complex **2** [40]	12.474

As shown in Fig.II.1, the AFM state in these paddlewheel-type dichromium complexes corresponds to the open-shell singlet state formed by the d-orbitals of the chromium ions. Therefore, spin polarization occurs, where the α electrons and β electrons exhibit different spatial distributions. The spin polarization increases as the open-shell property becomes larger, that is, as the bond distance increases. Consequently, when the electron-donating group is substituted, the spin polarization is smaller than that of the NS form, whereas when the electron-withdrawing group is substituted, the spin polarization becomes larger. Summarizing these trends, they are illustrated in Fig. II.5 and explained that:

I. When the electron-donating group is introduced into the paddlewheel-type dichromium complex, the electron density within the Cr-Cr bond increases, leading to the shorter Cr-Cr distance and reduced the spin polarization. Consequently, the orbital overlaps between the chromium ions, i.e., within the molecule, becomes larger. As a result, based on the electron transmission probability equation, the electron conductivity increases.
II. When the electron-withdrawing group is introduced into the complex, the electron density within the Cr-Cr bond decreases, leading to the elongated Cr-Cr distance and increased the spin polarization. Consequently, the orbital overlaps between the chromium ions, i.e., within the molecule, becomes smaller. As a result, the electron conductivity decreases.

In the transition probability equation, the orbital overlaps within the molecule are represented as the site-overlaps. The calculated site-overlaps were analyzed, revealing that they are almost zero except for the LUMO and LUMO+1. Therefore, these two molecular orbitals are considered the primary

contributors to the electron conductivity of these complexes. The site-overlaps of the LUMO and LUMO+1 are summarized in Table II.3. The results align with the aforementioned trends and indicate that the electron-donating groups increase the site-overlaps, whereas these parameters decrease when the electron-withdrawing groups are introduced. From the above, it has been revealed that the electron conductivity of the paddlewheel-type dichromium complexes can be controlled by the substituents.

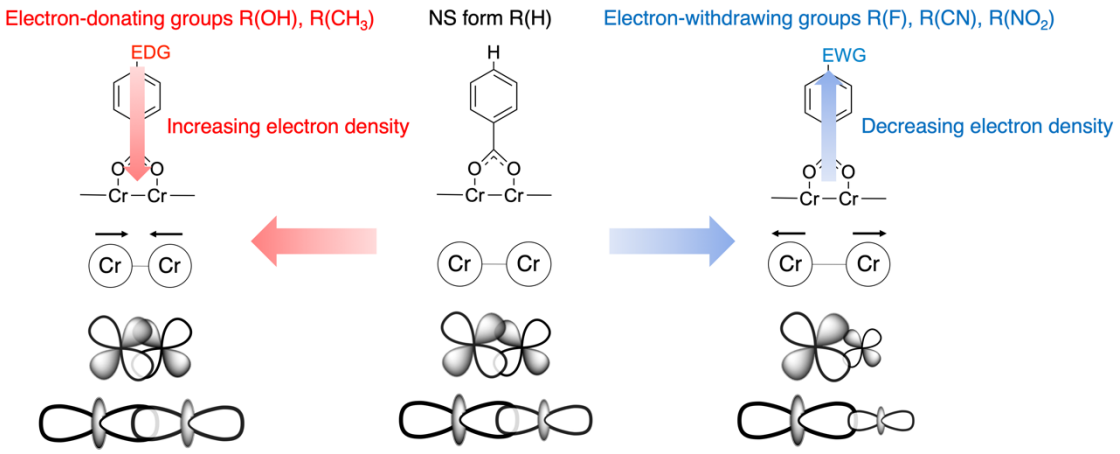

Fig. II.5. Effect of the substituents on the Cr-Cr bond. EDG and EWG mean Electron-Donating Group and Electron-Withdrawing Group, respectively. In addition to the π- and σ-orbitals shown in the figure, similar spin polarization occurs in another π-orbital and the δ-orbital.

Table II.3. The site-overlaps of the LUMO and LUMO+1 in the AFM states. The small difference between α and β orbital is considered to originate in a slight asymmetry of the optimized structures.

		Site-overlap	
		LUMO	LUMO+1
R(OH)	α	0.0085	0.0084
	β	0.0069	0.0069
$R(CH_3)$	α	0.0071	0.0071
	β	0.0076	0.0076
NS	α	0.0070	0.0070
	β	0.0069	0.0069
R(F)	α	0.0068	0.0068
	β	0.0066	0.0066
R(CN)	α	0.0054	0.0054
	β	0.0055	0.0055
$R(NO_2)$	α	0.0051	0.0051
	β	0.0051	0.0051

3.2 Difference in electron conductivity between the AFM and FM states

To consider the effect of changes in the spin state on the electron conductivity, the current in the magnetically excited (FM) states are also calculated for the model complexes. Here, the author only discussed the FM state which is the highest spin state as illustrated in Fig.II.1 (b). Considering the vertical excitation by an external field, the structure was fixed to the optimized structure in the AFM state. Fig. II.6 shows the calculated current values at 1.0 V in the FM state (I_{FM}) plotted against the Cr-Cr distance. The results indicate that the FM state exhibits much higher conductivity than the AFM state; however, changes in the electron conductivity due to substituents show almost the same trend as in the AFM state. Table II.4 shows the current ratio for the AFM and FM states before and after AP-optimization, $I_{Y,\,AP}/I_{Y,\,non\text{-}AP}$ (Y = AFM or FM). From Fig. II.3, II.4, II.6, and Table II.4, the current value increases by approximately 1.3 to 1.6 times in the AFM state due to AP-optimization, whereas it remains almost unchanged in the FM state. This trend corresponds to the fact that the spin contamination significantly affects the low-spin state, while it has little impact on the high-spin state.

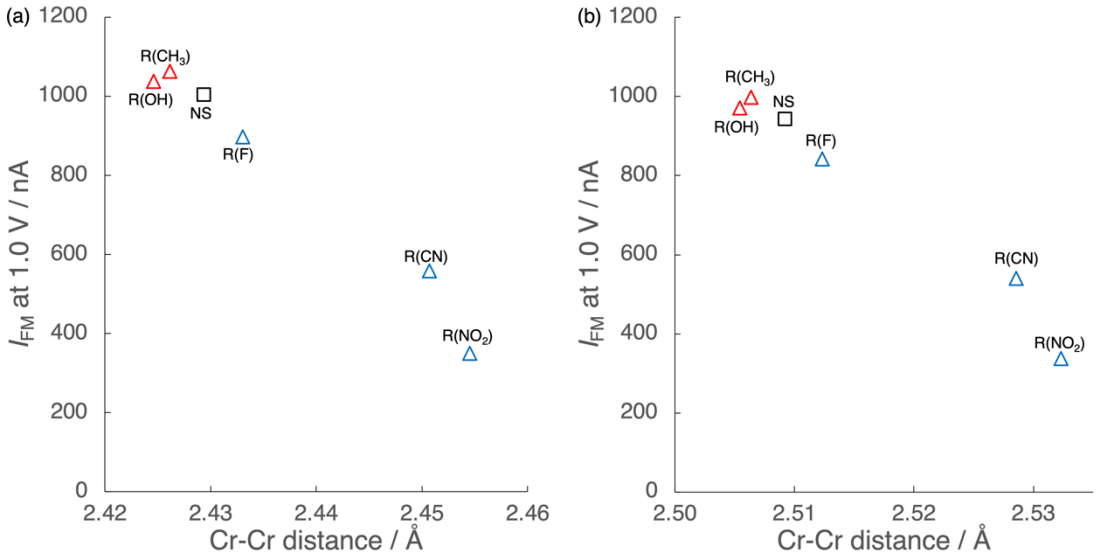

Fig. II.6. Calculated current values I_{FM} at 1.0 V in the FM states versus the distance between the dichromium ions of each complex (a) with AP-optimization and (b) without AP-optimization. The red triangle markers, the blue triangle markers and the black square marker represent electron-donating groups, -withdrawing groups and NS form, respectively.

Table II.4. Calculated current ratio before and after AP-optimization ($I_{Y,\,AP}$ / $I_{Y,\,non\text{-}AP}$), where the subscript Y indicates the spin state (Y = AFM or FM).

	$I_{Y,\,AP}$ / $I_{Y,\,non\text{-}AP}$	
	AFM	FM
R(OH)	1.35	1.07
R(CH_3)	1.38	1.06
NS	1.39	1.06
R(F)	1.40	1.06
R(CN)	1.43	1.04
R(NO_2)	1.59	1.04

The change in the electron conductivity between the AFM and FM states can be explained by the orbital correlation diagram and the spin polarization shown in Fig. II.7. In the AFM state, the spin polarization between α and β electrons leads to the uneven electron distribution. On the other hand, in the FM state, electrons are arranged in antibonding orbitals, resulting in the absence of spin polarization, and consequently, a more delocalized electron distribution. This delocalization facilitates the electron transport between the electrodes through the molecule, thereby increasing the electron conductivity. Table II.5 summarizes the site-overlaps of the LUMO and LUMO+1 in the FM states, which predominantly contribute to the electron conduction, as in the AFM states. From Table II.1 and II.5, comparing the calculated parameters related to the transition probability, the site-overlaps are significantly larger in the FM states than that in the AFM states. In addition, as illustrated in Fig. II.8, the FM states exhibit the delocalized electronic structures in both the LUMO and LUMO+1, whereas the AFM states exhibit the spin-polarized electronic structures. Thus, it has been clarified that in the FM state, the expanded distribution enhances the electron conductivity.

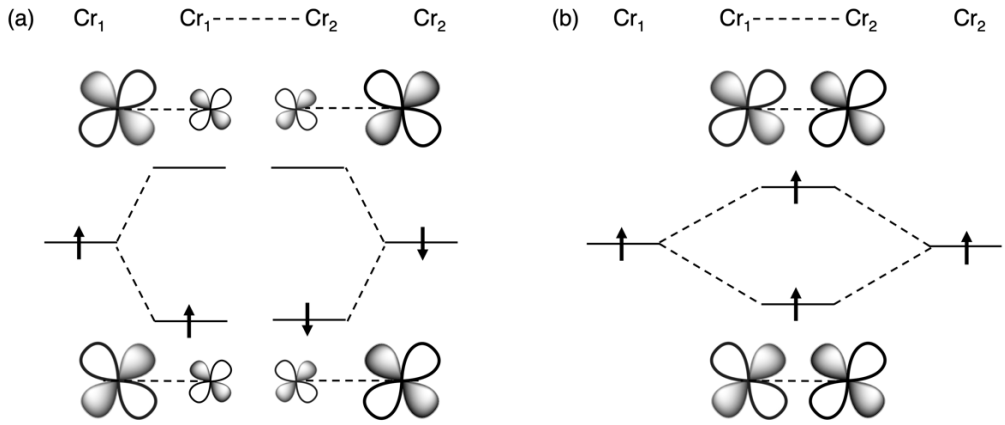

Fig. II.7. Orbital correlation diagram of (a) AFM and (b) FM states. The same trend applies to the σ-orbital, δ-orbital, and the other π-orbital, as shown in the figure.

Table II.5. Site-overlaps that contribute to the electron conductivity in the FM states. In the table, α and β represent the α and β orbitals, respectively. The small difference between α and β orbital values is considered to originate in a slight asymmetry of the optimized structures.

		Site-overlap	
		LUMO	LUMO+1
R(OH)	α	0.0490	0.0470
	β	0.0484	0.0486
$R(CH_3)$	α	0.0492	0.0472
	β	0.0511	0.0513
NS	α	0.0494	0.0475
	β	0.0514	0.0516
R(F)	α	0.0498	0.0481
	β	0.0517	0.0519
R(CN)	α	0.0508	0.0495
	β	0.0523	0.0526
$R(NO_2)$	α	0.0506	0.0497
	β	0.0522	0.0527

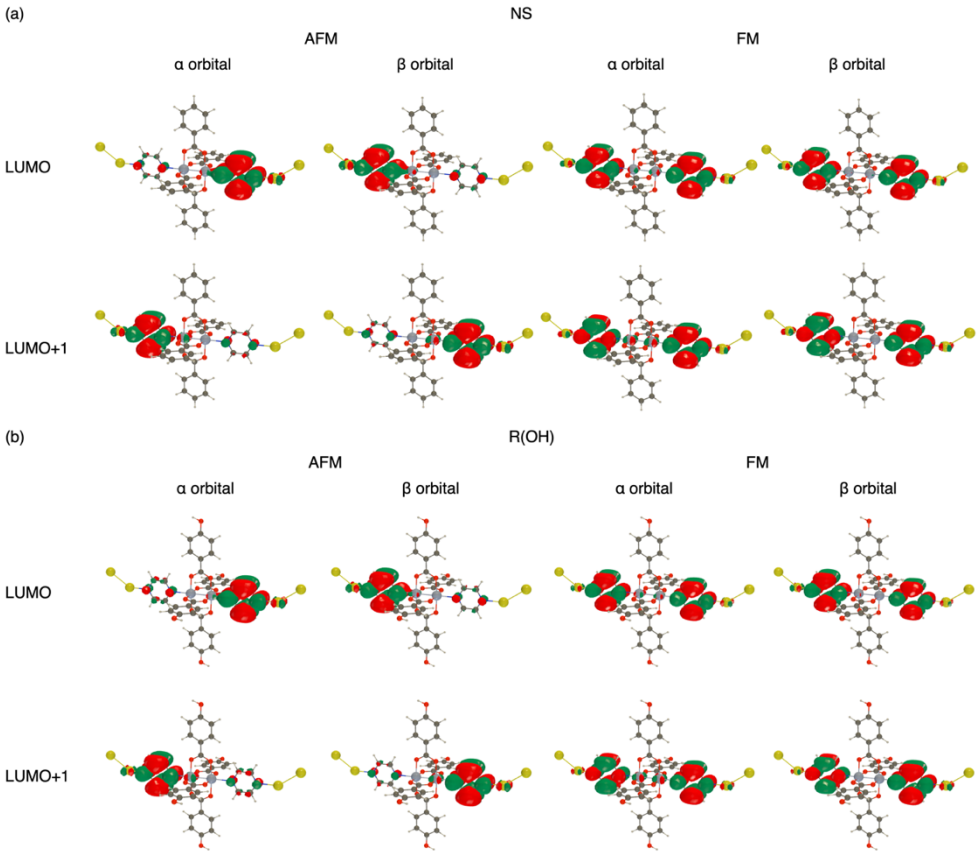

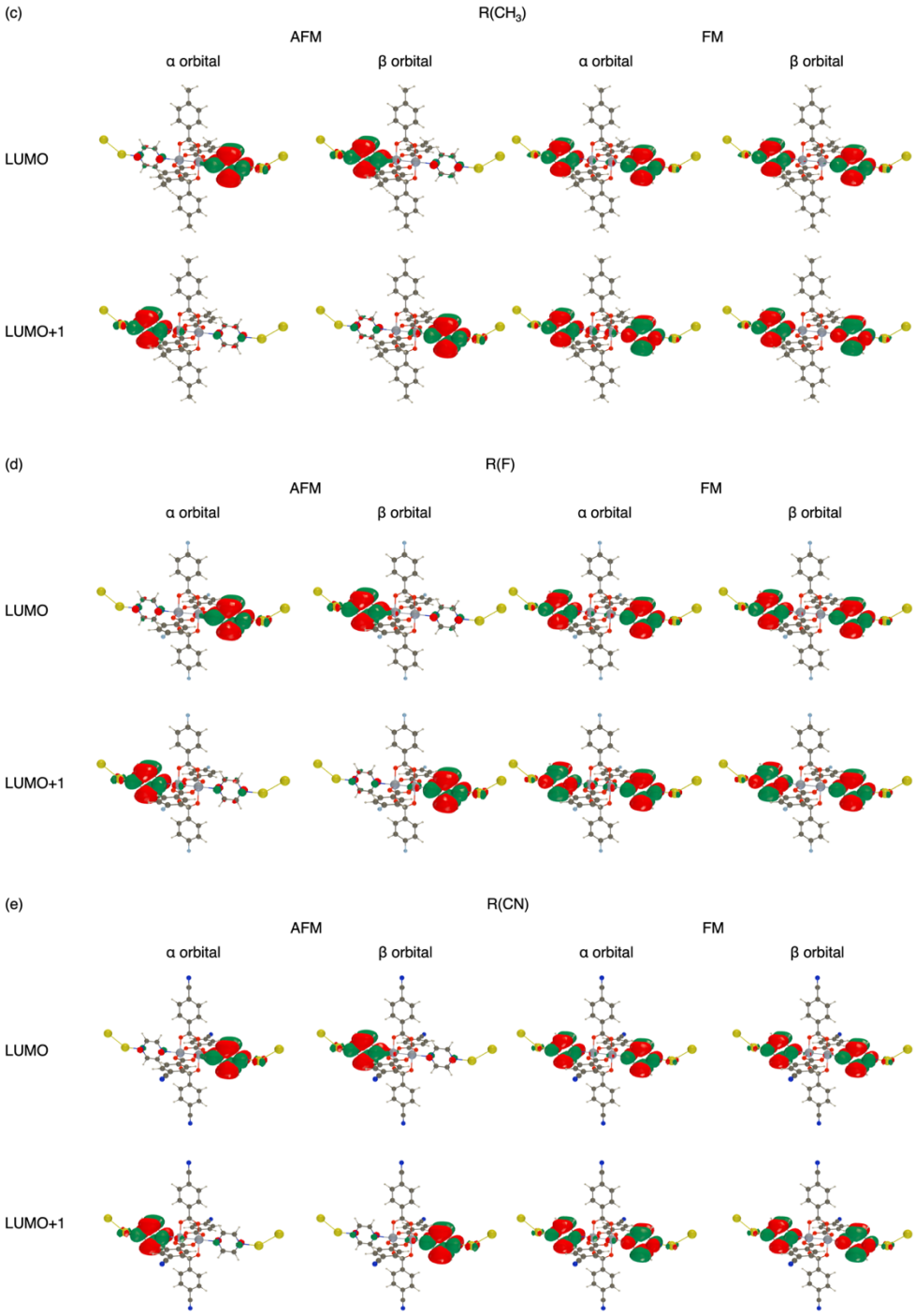
(c)
R(CH3)
AFM
FM
α orbital
β orbital
α orbital
β orbital
LUMO
LUMO+1
(d)
R(F)
AFM
FM
α orbital
β orbital
α orbital
β orbital
LUMO
LUMO+1
(e)
R(CN)
AFM
FM
α orbital
β orbital
α orbital
β orbital
LUMO
LUMO+1

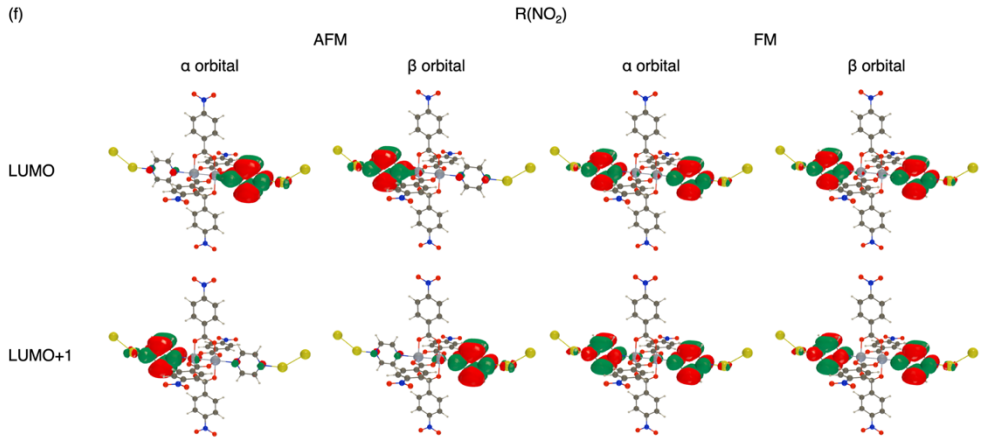

Fig. II.8. Electron distributions in the LUMO and LUMO+1 in the AFM states and the FM states of (a)NS, (b)R(OH), (c)R(CH_3), (d)R(F), (e)R(CN) and (f)R(NO_2).
Their isovalues are 0.02 electron/a.u.^{3}.

In Fig. II.8, the reason why the spin polarization appears on the axial ligand pyrazine rather than on the chromium in the electron distribution of the LUMO and LUMO+1 can be interpreted by considering the spin polarization in Cr-Cr bond and the orbital interactions between the chromium ions and the pyrazine ligands. The nature of the molecular orbitals formed between the metal and the ligand strongly depends on the component (either the metal or the ligand) whose energy levels are closer to the corresponding molecular orbital (see Fig. II.9(a)). Therefore, the molecular orbital correlation diagram formed by the interaction between the Cr-Cr bond and the pyrazine ligand is represented in Fig. II.9(b). The antibonding orbital corresponding to the spin-polarized distribution of the Cr-Cr bond in the bonding orbital appears in the LUMO, where the pyrazine ligand distribution is induced by the spin polarization of the Cr ions. Thus, it can be concluded that the pyrazine ligand exhibits a biased distribution due to spin polarization.

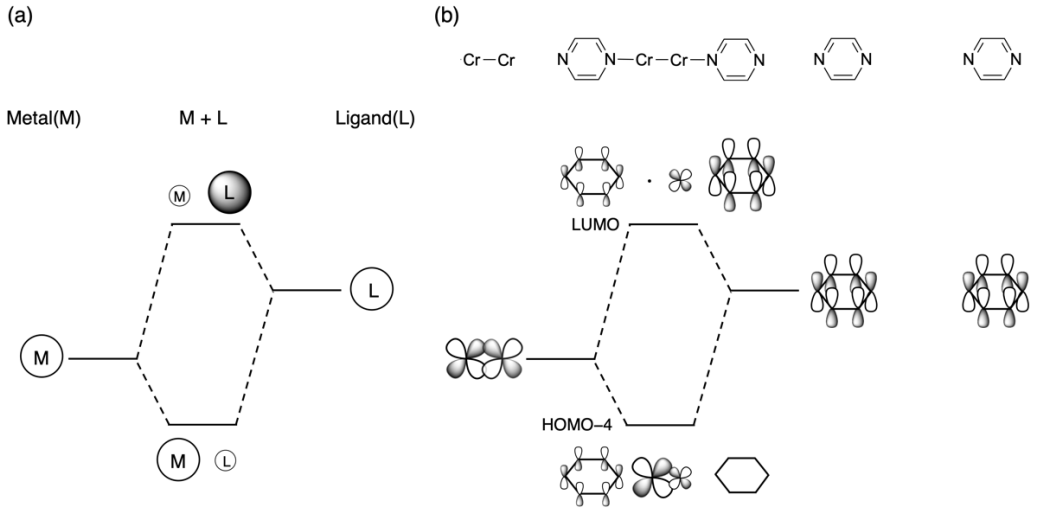

Fig. II.9. Orbital correlation diagram of (a) metal and ligand and (b) the chromium ions and the pyrazine axial ligands.

Fig. II.10 shows a ratio of the electronic currents between the AFM and FM states (I_{FM}/I_{AFM}) at 1.0 V, indicating that the electron-withdrawing groups increase the ratio, while the electron-donating groups decrease it. Moreover, from Fig. II.10, it can be observed that the current ratio, I_{FM}/I_{AFM}, calculated for structures without AP-optimization is overestimated by approximately 1.3 to 1.5 times compared to those obtained using AP-optimized structures, corresponding to the calculated current ratio before and after AP-optimization in the AFM states ($I_{AFM,\,AP}$ / $I_{AFM,\,non\text{-}AP}$). These results highlight the importance of eliminating spin contamination in electronic current calculations for strongly correlated molecular systems.

As summarized in Table II.6, the coupling constants and their products (${\gamma_{L1,\sigma}}^2 \times {\gamma_{MR,\sigma}}^2$) of the FM states are much larger than those of the AFM states. As a result, a significant difference in the electron conductivity between the AFM and FM states is considered to have emerged. To examine the effect of the substituents on the ratio, I_{FM}/I_{AFM}, in detail, the product of coupling constants, ${\gamma_{L1,\sigma}}^2 \times {\gamma_{MR,\sigma}}^2$, of the complexes are illustrated in Fig. II.11. In the AFM states, the spin polarization dominantly contributes to the electron conductivity, and the electron-withdrawing substituents with strong spin polarization exhibited the decrease in the electron conductivity. However, in the FM states, the spin polarization does not occur, and its impact becomes more significant for systems that exhibited strong spin polarization. As a result, from the viewpoint of the switching ratio (I_{FM}/I_{AFM}), the introduction of the electron-withdrawing groups is more effective than that of the electron-donating groups, and therefore, the switching ratio of the paddlewheel-type dichromium complex can be also controlled by the substituents.

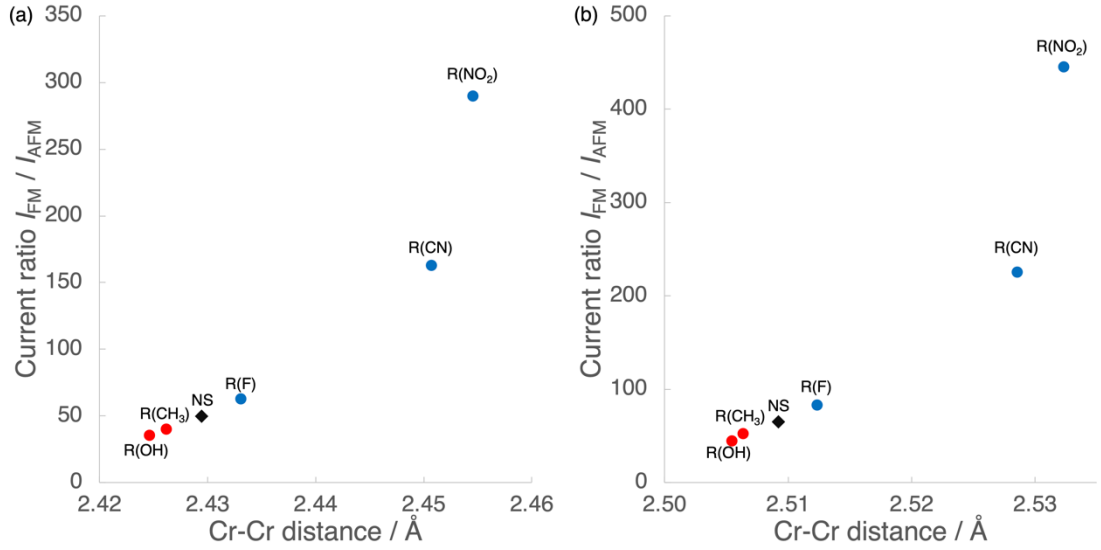

Fig. II.10. A ratio of the electronic currents between the AFM and FM states (I_{FM}/I_{AFM}) at 1.0 V (a) with AP-optimization and (b) without AP-optimization. The red, blue and black markers represent the complexes with the electron-donating groups, -withdrawing groups and NS form, respectively.

Table II.6. Coupling constants in the AFM and the FM states of (a)NS, (b)R(OH), (c)R(CH_3), (d)R(F), (e)R(CN) and (f)R(NO_2). In this table, the subscript σ represents either α or β, which correspond to the α orbital and the β orbital, respectively. Ratio of product (FM/AFM) represents the ratio of the products of the coupling constants ${\gamma_{L1,\sigma}}^2 \times {\gamma_{MR,\sigma}}^2$ for the AFM and the FM states.

(a)	NS			
	α orbital		β orbital	
	AFM state	FM state	AFM state	FM state
$\gamma_{L1,\sigma}$/eV	0.514	1.350	1.224	0.960
$\gamma_{MR,\sigma}$/eV	1.224	1.347	0.513	0.958
${\gamma_{L1,\sigma}}^2 \times {\gamma_{MR,\sigma}}^2$/eV^4	0.396	3.303	0.394	0.845
Ratio of product	8.33		2.14	
(b)	R(OH)			
	α orbital		β orbital	
	AFM state	FM state	AFM state	FM state
$\gamma_{L1,\sigma}$/eV	0.586	1.401	1.262	0.984
$\gamma_{MR,\sigma}$/eV	1.234	1.355	0.531	0.948
${\gamma_{L1,\sigma}}^2 \times {\gamma_{MR,\sigma}}^2$/eV^4	0.522	3.602	0.449	0.869
Ratio of product	6.90		1.93	

(c)	R(CH_3)			
	α orbital		β orbital	
	AFM state	FM state	AFM state	FM state
$\gamma_{L1,\sigma}$/eV	0.533	1.369	1.249	0.967
$\gamma_{MR,\sigma}$/eV	1.257	1.382	0.548	0.979
${\gamma_{L1,\sigma}}^2 \times {\gamma_{MR,\sigma}}^2$/eV^4	0.449	3.580	0.469	0.896
Ratio of product	7.98		1.91	
(d)	R(F)			
	α orbital		β orbital	
	AFM state	FM state	AFM state	FM state
$\gamma_{L1,\sigma}$/eV	0.485	1.302	1.167	0.927
$\gamma_{MR,\sigma}$/eV	1.160	1.292	0.473	0.920
${\gamma_{L1,\sigma}}^2 \times {\gamma_{MR,\sigma}}^2$/eV^4	0.316	2.832	0.304	0.728
Ratio of product	8.96		2.39	
(e)	R(CN)			
	α orbital		β orbital	
	AFM state	FM state	AFM state	FM state
$\gamma_{L1,\sigma}$/eV	0.357	1.112	0.970	0.751
$\gamma_{MR,\sigma}$/eV	0.970	1.112	0.358	0.751
${\gamma_{L1,\sigma}}^2 \times {\gamma_{MR,\sigma}}^2$/eV^4	0.120	1.529	0.120	0.318
Ratio of product	12.75		2.64	
(f)	R(NO_2)			
	α orbital		β orbital	
	AFM state	FM state	AFM state	FM state
$\gamma_{L1,\sigma}$/eV	0.274	0.936	0.759	0.603
$\gamma_{MR,\sigma}$/eV	0.757	0.932	0.270	0.601
${\gamma_{L1,\sigma}}^2 \times {\gamma_{MR,\sigma}}^2$/eV^4	0.043	0.760	0.042	0.131
Ratio of product	17.76		3.13	

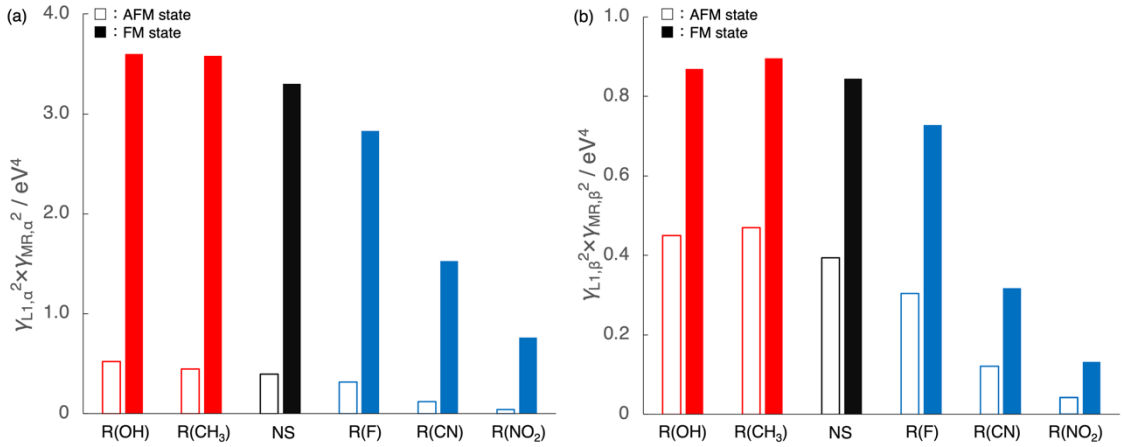

Fig. II.11. $\gamma_{L1,\sigma}{}^2 \times \gamma_{MR,\sigma}{}^2$ values of (a) α orbital and (b) β orbital of the model complexes.

In the experimental work for the single-molecule components, the applied bias voltage has usually been within the range of 0.1 - 1.0 V [12,16,17,44]. Thus, the author also examined the current-voltage (*I-V*) characteristics and the I_{FM}/I_{AFM} ratio at bias voltages of 0.5, 1.5 and 2.0 V. The calculated *I-V* characteristics of the AFM and FM states are shown in Fig. II.12 (a) and (b), respectively. The results indicate that the relationship between the bias voltage and calculated current remains consistent up to 2.0 V. Additionally, the I_{FM}/I_{AFM} ratio indicates the same trend up to 2.0 V, as shown in Fig. II.13.

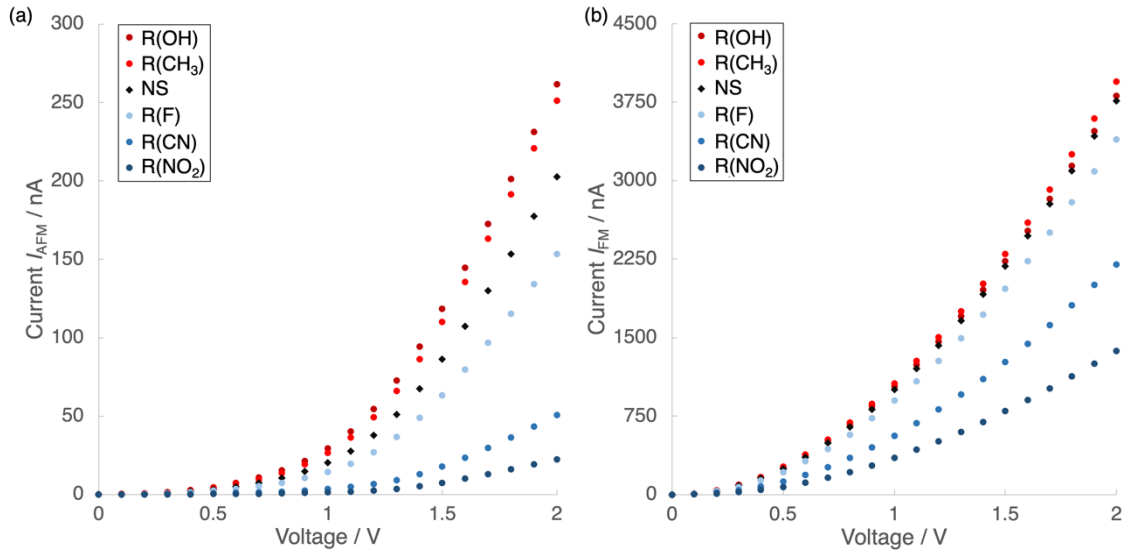

Fig. II.12. Calculated *I-V* characteristics for each complex in (a) the AFM state and (b) the FM state.

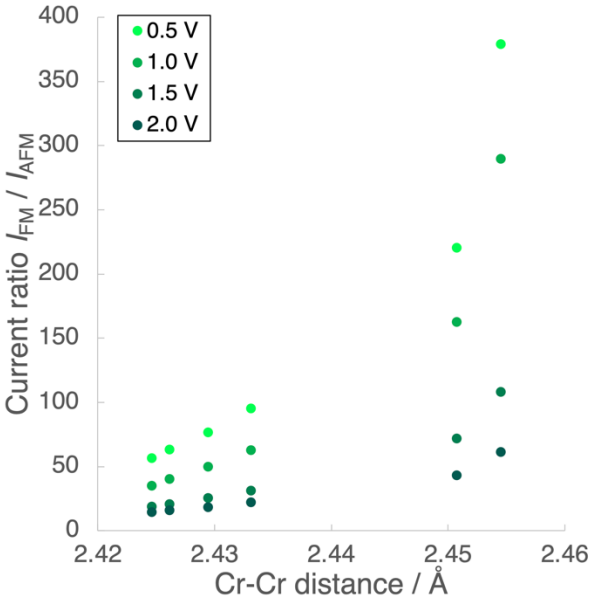

Fig. II.13. Electronic current ratio (I_{FM}/I_{AFM}) at 0.5 V, 1.0 V, 1.5 V and 2.0 V.

Finally, the author examined the exchange coupling (J) values between the two Cr(II) ions. In the two-site Heisenberg Hamiltonian, $\hat{H} = -2J_{ab}\hat{S}_a\hat{S}_b$, a spin operator $\hat{S}_i (i$ = a, b) becomes each Cr(II) ($S = 2$) in these complexes, and Table II.6 summarized the calculated J values by Yamaguchi equation (see Part I, Chapter 3). The total energies and $\langle \widehat{\boldsymbol{S}}^2 \rangle$ for the calculation of these J values are also summarized in Table II.6. The paddlewheel-type dichromium(II,II) complexes has been reported to exhibit partial paramagnetism in the Cr-Cr quadruple bond. The J value of $Cr_2(O_2CCH_3)_4(OH_2)_2$ was experimentally observed to be –490 cm^{-1} (see Table II.7) [52]. However, B3LYP was reported to overestimate the stability of the AFM state in the spin-polarized systems [50]. In fact, the J value of $Cr_2(O_2CCH_3)_4(OH_2)_2$, which was calculated to be –733 cm^{-1} by B3LYP using the X-ray structure, was overestimated by about 70% [35]. Therefore, the calculated J values of the model complexes in this study (–606 ~ –636 cm^{-1}) may represent an over-stabilization of the AFM state. On the other hand, it has also been reported that the overestimation can be corrected by using BHandHLYP, which includes 50% Hartree-Fock exchange [52]. The calculated J values of the NS form between BHandHLYP and B3LYP are summarized in Table II.7. The J value calculated using B3LYP is approximately 70% larger than that obtained with BHandHLYP, suggesting that B3LYP overestimates the J value. However, from the viewpoint of the Cr(II)-Cr(II) distance, AP-B3LYP has been reported to be able to reproduce the experimental Cr-Cr distance [48]. In addition, it has been confirmed that the I-V characteristics estimated using B3LYP can successfully reproduce the experimental results [24]. From these reasons, the author discussed the relationship between the electron conductivity and molecular structure using B3LYP.

The *J* values are slightly changed by the substituents as shown in Table II.6. The complexes with the electron-donating groups enhance the anti-ferromagnetic interaction, while the electron-withdrawing groups weaken it. The result is consistent with the difference in electron conductivity by the substituents. On the other hand, the change in the exchange coupling is within 30 cm^{-1}, suggesting that the electron conductivity shows a stronger dependency on the spin polarization.

Table II.6. The total energy, $\langle \widehat{S}^2 \rangle$ values of the AFM and FM states and effective exchange integrals (*J*) values of the extended molecules.

	Total energy / a. u.		$\langle \widehat{S}^2 \rangle$		
	AFM	FM	AFM	FM	J / cm^{-1}
R(OH)	−5141.465538	−5141.425873	3.5829	20.0191	−636
R(CH_3)	−4997.869403	−4997.829566	3.5811	20.0191	−638
NS	−4840.597525	−4840.557873	3.5830	20.0189	−634
R(F)	−5237.529641	−5237.490277	3.5856	20.0188	−629
R(CN)	−5209.549988	−5209.511696	3.5963	20.0184	−610
R(NO_2)	−5658.575993	−5658.537932	3.5986	20.0183	−606

Table II.7. Calculated and experimental *J* values by B3LYP and BHandHLYP with the paddlewheel-type dichromium(II,II) benzoate (NS) and $Cr_2(O_2CCH_3)_4(H_2O)_2$.

	J / cm^{-1}	
Method	NS	$Cr_2(O_2CCH_3)_4(H_2O)_2$ [35]
B3LYP	−634	−734
BHandHLYP	−460	−520
Expt. [51]	---	−490

4. Conclusion

In this study, the author investigated the single-molecule electron conductivity of the paddlewheel-type dichromium(II,II) tetrabenzoate complexes by introducing the electron-donating and electron-withdrawing groups into the bridging ligands. The results indicated that the electron conductivity of the model complexes increases/decreases by substitution of the electron-donating/withdrawing groups, respectively. Especially, the electron-donating group is effective to increase the electron conductivity due to the suppression of the spin polarization. On the other hand, from the viewpoint of the switching ratio between the AFM and FM states (I_{FM}/I_{AFM}), the electron-withdrawing group is more effective because the transition to the FM state eliminates spin polarization, making its impact more significant. From these results, the electron conductivity and its switching ratio, achieved by changing the spin states of the paddlewheel-type dichromium tetrabenzoate complex, can be controlled through the

introduction of substituents. This finding provides the design guideline for single-molecule transistors utilizing open-shell electronic states.

References

1. R. Yamada, H. Kumazawa, T. Noutoshi, S. Tanaka, H. Tada, *Nano Lett.*, **2008**, *8*, 1237.
2. J. Sukegawa, C. Schubert, X. Zhu, H. Tsuji, D. M. Guldi, E. Nakamura, *Nat. Chem*., **2014**, *6*, 899.
3. T. Gao, C. He, C. Liu, Y. Fan, C. Zhao, C. Zhao, W. Su, Y. J. Dappe, L. Yang, *Phys. Chem. Chem. Phys.*, **2021**, *23*, 21163.
4. C. Jia, A. Migliore, N. Xin, S. Huang, J. Wang, Q. Yang, S. Wang, H. Chen, D. Wang, B. Feng, Z. Liu, G. Zhang, D.-H. Qu, H. Tian, M. A. Ratner, H. Q. Xu, A. Nitzan, X. Guo, *Science*, **2016**, *352*, 1443.
5. Y. Han, C. Nickle, Z. Zhang, H. P. A. G. Astier, T. J. Duffin, D. Qi, Z. Wang, E. del Barco, D. Thompson, C. A. Nijhuis, *Nat. Mater.*, **2020**, *19*, 843.
6. J. Li, S. Pudar, H. Yu, S. Li, J. S. Moore, J. Rodríguez-López, N. E. Jackson, C. M. Schroeder, *J. Phys. Chem. C*, **2021**, *125*, 21862.
7. M. Elbing, R. Ochs, M. Koentopp, M. Fischer, C. von Hänisch, F. Weigend, F. Evers, H. B. Weber, M. Mayor, *Proc. Natl. Acad. Sci. USA*, **2005**, *102*, 8815.
8. B. Capozzi, J. Xia, O. Adak, E. J. Dell, Z.-F. Liu, J. C. Taylor, J. B. Neaton, L. M. Campos, L. Venkataraman, *Nat. Nanotech*., **2015**, *10*, 522.
9. M. Li, H. Fu, B. Wang, J. Cheng, W. Hu, B. Yin, P. Peng, S. Zhou, X. Gao, C. Jia, X. Guo, *J. Am. Chem. Soc.*, **2022**, *144*, 20797.
10. S. Cai, W. Deng, F. Huang, L. Chen, C. Tang, W. He, S. Long, R. Li, Z. Tan, J. Liu, J. Shi, Z. Liu, Z. Xiao, D. Zhang, W. Hong, *Angew. Chem. Int. Ed.*, **2019**, *58*, 3829.
11. W. Zhao, D. Zou, Z. Sun, Y. Xu, G. Ji, X. Li, C. Yang, *Adv. Theory Simul.*, **2020**, *3*, 2000163
12. G. Sedghi, V. M. García-Suárez, L. J. Esdaile, H. L. Anderson, C. J. Lambert, S. Martín, D. Bethell, S. J. Higgins, M. Elliott, N. Bennett, J. E. Macdonald, R. J. Nichols, *Nat. Nanotech.*, **2011**, *6*, 517.
13. D. Aravena, E. Ruiz, *J. Am. Chem. Soc.*, **2012**, *134*, 777.
14. Y. Tanaka, Y. Kato, K. Sugimoto, R. Kawano, T. Tada, S. Fujii, M. Kiguchi, M. Akita, *Chem. Sci.*, **2021**, *12*, 4338.
15. J. F. Berry, in *Multiple Bonds Between Metal Atoms*, F. A. Cotton, C. A. Murillo, R. A. Walton (Ed.), Springer Science and Business Media, Inc., New York, 3rd ed., 2005, pp. 669-706.
16. I.-W. P. Chen, M.-D. Fu, W.-H. Tseng, J.-Y. Yu, S.-H. Wu, C.-J. Ku, C.-H. Chen, S.-M. Peng, *Angew. Chem. Int. Ed.*, **2006**, *45*, 5814.
17. S.-A. Hua, M.-C. Cheng, C.-h. Chen, S.-M. Peng, *Eur. J. Inorg. Chem.*, **2015**, 2510.
18. D. A. Pantazis, J. E. McGrady, *J. Am. Chem. Soc.*, **2006**, *128*, 4128.

19. I. -P. Liu, M. Bénard, H. Hasanov, I. -W. Chen, W. -H. Tseng, M. -D. Fu, M. -M. Rohmer, C. -h. Chen, G. -H. Lee, S. -M. Peng, *Chem.–Eur. J.*, **2007**, *13*, 8667.
20. X. López, M. Bénard, M. -M. Rohmer, *Inorg. Chem.*, **2007**, *46*, 5.
21. M. Spivak, V. Arcisauskaite, X. López, J. E. McGrady, C.de Graaf, *Dalton Trans*., **2017**, *46*, 6202.
22. V. P. Georgiev, W. M. C. Sameera, J. E. McGrady, *J. Phys. Chem. C*, **2012**, *116*, 20163.
23. V. P. Georgiev, P. J. Mohan, D. DeBrincat, J. E. McGrady, *Coord. Chem. Rev.*, **2013**, *257*, 290.
24. Y. Kitagawa, T. Matsui, Y. Nakanishi, Y. Shigeta, T. Kawakami, M. Okumura, K. Yamaguchi, *Dalton. Trans.*, **2013**, *42*, 16200.
25. Y. Kitagawa, M. Asaoka, Y. Natori, K. Miyagi, R. Teramoto, T. Matsui, Y. Shigeta, M. Okumura, M. Nakano, *Polyhedron*, **2017**, *136*, 125.
26. Y. Kitagawa, H. Tada, I. Era, T. Fujii, K. Ikenaga, M. Nakano, *Molecules*, **2019**, *24*, 1956.
27. P.-J. Huang, Y. Natori, Y. Kitagawa, Y. Sekine, W. Kosaka, H. Miyasaka, *Inorg. Chem.*, **2018**, *57*, 5371.
28. T. Tsuchiya, R. Umemura, M. Kaminaga, S. Kushida, K. Ohkubo, S. Noro, Y. Mazaki, *ChemPlusChem*, **2019**, *84*, 655.
29. Y. Kataoka, N. Yano, Y. Kohara, T. Tsuji, S. Inoue, T. Kawamoto, *ChemCatChem*, **2019**, *11*, 6218.
30. S. Ogawa, S. Chattopadhyay, Y. Tanaka, T. Ohto, T. Tada, H. Tada, S. Fujii, T. Nishino, M. Akita, *Chem. Sci.*, **2021**, *12*, 10871.
31. M. Meng, Z. Tang, S. Mallick, M. H. Luo, Z. Tan, J. Liu, J. Shi, Y. Yang, C. Y. Liu, W. Hong, **2020**, *12*, 10320.
32. R. D. Davy, M. B. Hall, *J. Am. Chem. Soc*., **1989**, *111*, 1268.
33. K. Andersson, C.W. Bauschlicher Jr., B.J. Persson, B.O. Roos, *Chem. Phys. Lett.*, **1996**, *257*, 238.
34. G.L. Macchia, G.L. Manni, T.K. Todorova, M. Brynda, F. Aquilante, B.O. Roos, L. Gagliardi, *Inorg. Chem.*, **2010**, *49*, 5216.
35. Y. Kitagawa, T. Kawakami, Y. Yoshioka, K. Yamaguchi, *Polyhedron*, **2001**, *20*, 1189.
36. N. Yasuda, Y. Kitagawa, H. Hatake, T. Saito, Y. Kataoka, T. Matsui, T. Kawakami, S. Yamanaka, M. Okumura, K. Yamaguchi, in *Quantum Systems in Chemistry and Physics Progress in Methods and Applications*, K. Nishikawa, J. Maruani, E. Brändas, G. Delgado-Barrio, P. Piecuch (Ed.), Springer, Dordrecht, 2012, pp. 345-359.
37. Y. Kitagawa, T. Saito, K. Yamaguchi, in *Symmetry (Group Theory) and Mathematical Treatment in Chemistry*, T. Akitsu (Ed.), InTechOpen, London, 2018, pp. 121-139.
38. Y. Luo, C. -K. Wang, Y. Fu, *J. Chem. Phys.* **2002**, *117,* 10283.
39. L. -L. Lin, J. -C. Leng, X. -N. Song, Z. -L. Li, Y. Luo, C. -K. Wang, *J. Phys. Chem. C*, **2009**, *113*, 14474.
40. F. A. Cotton, T. R. Felthouse, *Inorg. Chem.*, **1980**, *19*, 328.
41. A. D. Becke, *J. Chem. Phys*., **1993**, *98*, 5648.

42. W. J. Hehre, R. Ditchfield, J. A. Pople, *J. Chem. Phys.*, **1972**, *56*, 2257.
43. P. C. Hariharan, J. A. Pople, *Theoret. Chim. Acta*, **1973**, *28*, 213.
44. Y. Zang, A. Pinkard, Z.-F. Liu, J. B. Neaton, M. L. Steigerwald, X. Roy, L. Venkataraman, *J. Am. Chem. Soc.*, **2017**, *139*, 14845.
45. I. L. Herrer, A. K. Ismael, D, C. Milań, A. Vezzoli, S. Martín, A. Gonzaĺez-Orive, I. Grace, C. Lambert, J. L. Serrano, R. J. Nichols, P. Cea, *J. Phys. Chem. Lett.*, **2018**, *9*, 5364.
46. P. J. Hay, W. R. Wadt, *J. Chem. Phys.*, **1985**, *82*, 299.
47. M. J. Frisch, G. W. Trucks, H. B. Schlegel, G. E. Scuseria, M. A. Robb, J. R. Cheeseman, G. Scalmani, V. Barone, B. Mennucci, G. A. Petersson, et al., *Gaussian 09 Rev.D01*; Gaussian Inc.: Wallingford, CT, USA, 2009.
48. Y. Kitagawa, N. Yasuda, H. Hatake, T. Saito, Y. Kataoka, T. Matsui, T. Kawakami, S. Yamanaka, M. Okumura, K. Yamaguchi, *Int. J. Quant. Chem*., **2013**, *113*, 290.
49. Y. Kitagawa, T. Saito, Y. Nakanishi, M. Ito, M. Shoji, K. Koizumi, S. Yamanaka, T. Kawakami, M. Okumura, K. Yamaguchi, *AIP Conf. Proc.*, **2007**, *963*, 334.
50. T. Soda, Y. Kitagawa, T. Onishi, Y. Takano, Y. Shigeta, H. Nagao, Y. Yoshioka, K. Yamaguchi, *Chem. Phys. Lett.*, **2000**, *319*, 223.
51. F. A. Cotton, H. Chen, L. M. Daniels and X. Feng, *J. Am. Chem. Soc.*, **1992**, *114*, 8980.
52. Y. Kitagawa, T. Soda, Y. Shigeta, S. Yamanaka, Y. Yoshioka, K. Yamaguchi, *Int. J. Quant. Chem.*, **2001**, *84*, 592.

Part III

Comparison of open-shell electronic state and electron conductivity in single molecule and two-molecule system

1. Introduction

For the use of single-molecule components as devices, integration—such as connecting or assembling them—is considered important. Recently, research on the integration of single-molecule components has also been conducted, with reports evaluating the performance and characteristics of systems consisting of multiple molecular components such as self-assembled monolayers (SAMs), arrangement on semiconductor chips, and placing on carbon nanotube substrate [1-5].

In recent years, there have been interesting results on molecular circuits. According to the Ohm's law, the current value of a parallel circuit equals to the sum of current through each resistor. However, in molecular parallel circuits, the Ohm's law is fail because of quantum interference effects [6]. The conductance G, in nano-scale parallel circuits of two components is given as

$$G = G_1 + G_2 + 2\sqrt{G_1 G_2}\,, \tag{III.1}$$

where G_1 and G_2 are the conductance of respective components and $2\sqrt{G_1 G_2}$ is the quantum interference term. Vazquez and his co-workers demonstrated that the conductance of a molecular parallel circuit model composed of two parallel benzenes is larger than twice that of a single benzene, both experimentally and theoretically [7]. Recently, several exceptions to Equation (III.1) have been reported from the perspectives of aromaticity, frontier orbital theory, and orbital interaction [8,9]. However, molecular circuits in open-shell electronic systems have not been investigated.

In this study, as the first step toward molecular integrated systems utilizing open-shell single-molecule components, the author considered the simplest molecular parallel circuit model composed of two components. As such a model, the author considered a molecular parallel circuit model based on [18]annulene, as shown in Fig. III.1. As shown in Fig. III.1, [18]annulene can be assumed to be a parallel circuit composed of two linear polyenes (Polyene A and Polyene B). The sulfur atoms at the end-sites form thiol radicals, leading the linear polyenes to exhibit open-shell electronic structures. In such a molecular parallel circuit model, the electronic structures and the electron conductivities of both the circuit and its components were calculated by DFT and ESGF methods. Subsequently, the author examined the relationship between electron conductivity in the molecular parallel circuit model and that of individual molecular components, comparing it to the classical parallel circuit, where Ohm's law holds for electrical conductivity.

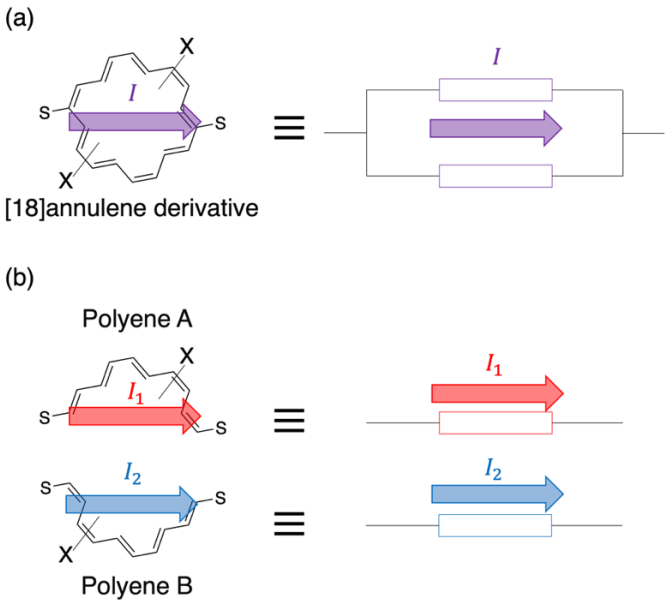

Fig. III.1. Illustration of the molecular parallel circuit models: (a) [18]annulene derivative as the parallel circuit, and (b) two linear polyenes A and B divided from the [18]annulene derivative as the individual components.

2. Computational Details

[18]annulene derivatives were used as the molecular parallel circuit models, which were assumed to be composed of two linear polyenes (Polyene A and Polyene B). The end-sites of these molecules were sulfur atoms, with the assumption that the junctions between the end-sites and Au(111) surface were at the bridge-site, as illustrated in Fig. III.2. Similar to the paddlewheel-type dichromium complexes in Part II, the electrodes were approximated as the gold dimers. To modify the open-shell electronic state of the molecular circuit and single-molecule components, various substituents X were introduced into the model molecules, and comparisons were made with the non-substituted (NS) form. To consider the open-shell electronic state, the electronic structures were calculated using spin-unrestricted DFT, that enabled the spin polarization to be performed involved the static electron correlation effect.

[18]annulene derivatives were geometrically optimized by the BHandHLYP/6-31+G*(S), 6-31G*(other atoms) level of theory [10-13]. The two linear polyenes, Polyene A and Polyene B, were extracted from the optimized [18] annulene structures. Subsequently, only the hydrogen atoms added at the boundaries of the polyenes were geometrically optimized. The electronic structures of the extended molecules, including the gold dimer in the molecules, were determined using spin-unrestricted DFT calculations with the BHandHLYP functional. The basis sets used were LANL2DZ [14] for Au, 6-31+G* for S, and 6-31G* for other atoms. For all models, the charge and the spin states were set to neutral and singlet, respectively.

The electron conductivity was calculated through ESGF methods, explained in Part I, Chapter 2, assuming that the temperature was 300 K and the electron conduction occurred through the molecular orbitals from LUMO+9 to HOMO−9. All DFT calculations were performed in the gas phase using Gaussian 09 Rev. D01 [15], and the electron conductivity was calculated using our self-developed program.

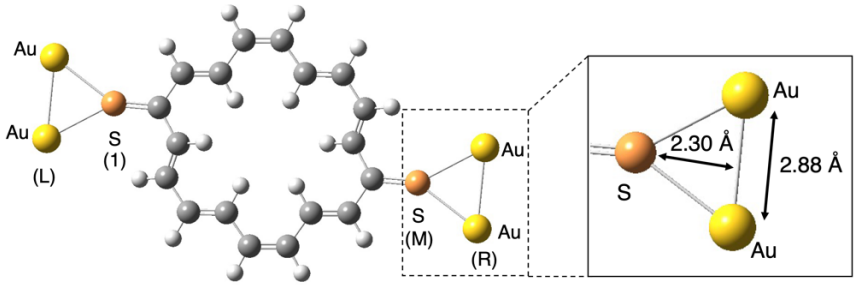

Fig. III.2. Model of the extended molecule of the NS form. The electrodes are approximated by the gold dimers, and the junctions between the Au and S atoms are assumed to be the bridge-site. The labels 1 and M represent the end-sites; L and R are the left and right electrodes, respectively. The distances between the middle point of the Au dimer and the sulfur atom were fixed at 2.30 Å, and the Au–Au distance was assumed to be 2.88 Å [16,17].

3. Results and Discussion

3.1 Electron conductivity of [18]annulene as the molecular parallel circuit model

First, using the NS form, the author examined the relationship between the electron conductivity of the molecular parallel circuit model based on [18]annulene and that of the two linear polyenes as individual single-molecule components. Fig. III.3 shows the current-voltage (*I*–*V*) characteristics of [18]annulene (I_{annulene}) and the total of the current values of the two polyenes, which are defined by two equations. The first equation represents a simply summation, analogous to a classical parallel circuits:

$$I_{\text{A+B}} = I_{\text{Polyene A}} + I_{\text{Polyene B}}, \tag{III.2}$$

where $I_{\text{Polyene A}}$ and $I_{\text{Polyene B}}$ represent the current of Polyene A and Polyene B, respectively. The second equation accounts for the quantum interference (QI) term base on Equation (III.1):

$$I_{\text{A+B+Q}} = I_{\text{Polyene A}} + I_{\text{Polyene B}} + 2\sqrt{I_{\text{Polyene A}} I_{\text{Polyene B}}}, \tag{III.3}$$

where $2\sqrt{I_{\text{Polyene A}} I_{\text{Polyene B}}}$ is the QI term. As shown in Fig. III.3, the calculated currents values of the [18]annulene were larger than $I_{\text{A+B}}$, however, smaller than $I_{\text{A+B+Q}}$. Therefore, in the molecular parallel circuit model with the open-shell electronic system, it has been revealed that neither Ohm's law in classical circuits, as shown in Equation (III.2), nor the existing conductivity equation incorporating quantum interference in molecular parallel circuits, as shown in Equation (III.3), holds.

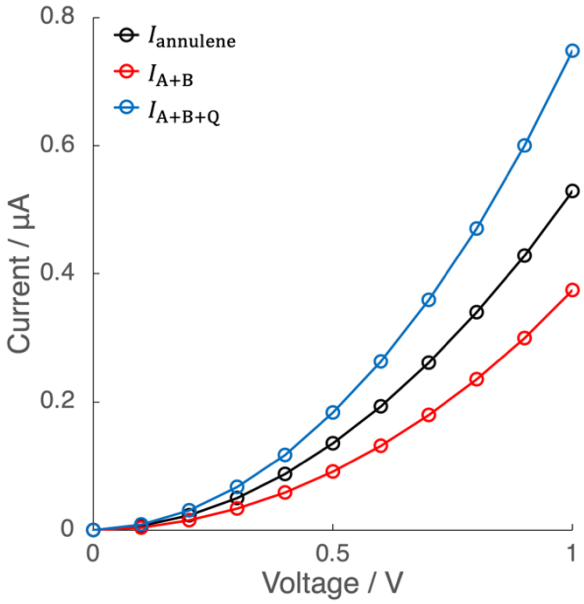

Fig. III.3. *I–V* characteristics of the [18]annulene ($I_{annulene}$), the sum of independent polyenes (I_{A+B}), and the values including the QI term (I_{A+B+Q}).

To analyze the difference in the electron conductivity between the $I_{annulene}$ and I_{A+B}, I_{A+B+Q}, various calculated parameters were examined, including the total spin angular momentum $\langle \widehat{\boldsymbol{S}}^2 \rangle$ and coupling constants $\gamma_{L1,\sigma}, \gamma_{MR,\sigma}$, as summarized in Table III.1, as well as the site-overlaps in each molecular orbital, as summarized in Table III.2. From the calculated $\langle \widehat{\boldsymbol{S}}^2 \rangle$ values in Table III.1, it is found that the [18]annulene exhibits a closed-shell electronic state, whereas the divided polyenes exhibit weak open-shell systems. Such difference in the electronic states significantly affects the coupling constants and site-overlaps. Specifically, according to Tables III.1 and III.2, in the closed-shell system of [18]annulene, the $\gamma_{L1,\sigma}, \gamma_{MR,\sigma}$ and site-overlaps exhibit equal values for the α and β orbitals. However, in the open-shell system of the linear polyenes, these parameters show different values between the α and β orbitals, indicating the spin polarization. Therefore, the [18]annulene facilitates the electron transfer between the left and right electrodes, whereas the divided polyenes, due to their asymmetric electron distributions, makes it more difficult for electrons to migrate to the opposite electrode. Such differences in the electron transfer mechanisms are considered to be the cause of the differences observed between $I_{annulene}$ and I_{A+B}, I_{A+B+Q}. As a result, it has been clarified that in the open-shell electronic molecular parallel circuits, considerations incorporating the quantum interference are essential.

Table III.1. Summary of the total spin angular momentum $\langle \widehat{\boldsymbol{S}}^2 \rangle$ and coupling constants of the [18]annulene and the divided polyenes. In this table, α and β represent α and β orbitals, respectively.

	[18]annulene		Polyene A		Polyene B	
	α	β	α	β	α	β
$\langle \widehat{\boldsymbol{S}}^2 \rangle$	0.000		0.147		0.147	
$\gamma_{L1,\sigma}$ / eV	0.855	0.855	1.078	0.674	0.675	1.049
$\gamma_{MR,\sigma}$ / eV	0.855	0.855	0.675	1.049	1.078	0.674
${\gamma_{L1,\sigma}}^2 \times {\gamma_{MR,\sigma}}^2$ / eV^4	0.534	0.534	0.530	0.500	0.530	0.500

Table III.2. Site-overlap values of each orbital for the [18]annulene and the divided polyenes.

	Site-overlap					
	[18]annulene		Polyene A		Polyene B	
	α	β	α	β	α	β
HOMO−9	0.0000	0.0000	0.0002	0.0000	0.0001	0.0000
HOMO−8	0.0213	0.0213	0.0000	0.0002	0.0000	0.0001
HOMO−7	0.0158	0.0158	0.0000	0.0000	0.0000	0.0000
HOMO−6	0.4074	0.4074	0.0000	0.0000	0.0000	0.0000
HOMO−5	2.2823	2.2823	0.2068	0.1903	0.1287	0.1534
HOMO−4	0.9860	0.9860	0.0043	1.5019	0.0036	1.4478
HOMO−3	0.0033	0.0033	0.0557	0.9201	0.0465	0.8951
HOMO−2	0.0150	0.0150	0.0015	0.0035	0.0000	0.0023
HOMO−1	0.0321	0.0321	0.0000	0.0000	0.0000	0.0000
HOMO	0.0331	0.0331	0.0000	0.0000	0.0000	0.0000
LUMO	0.0703	0.0703	0.0578	0.0351	0.0453	0.0515
LUMO+1	0.0341	0.0341	0.0002	0.0001	0.0000	0.0000
LUMO+2	0.0001	0.0001	0.0099	0.0013	0.0022	0.0001
LUMO+3	0.0023	0.0023	0.0308	0.0323	0.0342	0.0593
LUMO+4	0.0003	0.0003	0.0151	0.0112	0.0127	0.0158
LUMO+5	0.0037	0.0037	0.0000	0.0000	0.0030	0.0027
LUMO+6	0.0130	0.0130	0.0003	0.0002	0.0000	0.0000
LUMO+7	0.0000	0.0000	0.0135	0.0128	0.0310	0.0294
LUMO+8	0.0001	0.0001	0.0016	0.0016	0.0018	0.0017
LUMO+9	0.0170	0.0170	0.0000	0.0000	0.0000	0.0000
Total	3.94	3.94	0.398	2.71	0.309	2.66

3.2. Effects of substituents on the electron conductivity of molecular parallel circuits with the open-shell electronic states

As described in the previous section, both electron conductivity and the QI term were influenced by the open-shell property of the molecules. Additionally, in Part II, it was demonstrated that the electron conductivities and open-shell electronic states of single-molecule components can be modulated by introducing substituents. Based on them, the author examined the impact of adjusting the open-shell electronic states of single-molecule components through substituent introduction on the electron conductivity of molecular parallel circuits. To explore the effects of substituents on the molecular parallel circuits, the relationship between open-shell electronic state and electron conductivity was examined by introducing electron-donating groups (X = -OCH_3, -OH) and electron-withdrawing groups (X = -CN, -NO_2) into [18]annulene and divided polyenes. Two substituted models, **1** and **2**, were considered, with two substituents placed symmetrically, as shown in Fig. III.4(a). The NO_2-substituted derivative of model **2** was excluded because the sulfur atom is structurally too close to the oxygen atoms of the nitro group, leading to unintended bond formation. The current values for substituted annulenes and polyenes at 1.0 V are presented in Fig. III.4(b). The results indicate that introducing substituents reduces electron conductivity in both annulenes and polyenes, irrespective of whether the substituents are electron-donating or withdrawing in the model **1**. However, in the case of the model **2**, an increase in electron conductivity compared to the NS form was observed when electron-donating groups were substituted, whereas the substitution of electron-withdrawing groups resulted in a decrease in electron conductivity. Furthermore, the relationship between the current values of annulenes and the total currents of the two polyenes differs depending on the type of substituents regardless the type of models. For electron-donating groups, the current values of annulenes do not match the total current values of the polyenes, even when the QI term is included ($I_{\mathrm{annulene}} \neq I_{\mathrm{A+B}}$, $I_{\mathrm{annulene}} \neq I_{\mathrm{A+B+Q}}$). In contrast, for electron-withdrawing groups, the annulene current becomes comparable to the simple sum of the two polyene currents ($I_{\mathrm{annulene}} \fallingdotseq I_{\mathrm{A+B}}$). From these results, it is suggested that in the molecular parallel circuits composed of single-molecule components with enhanced spin polarization due to the introduction of electron-withdrawing groups, the quantum interference is suppressed.

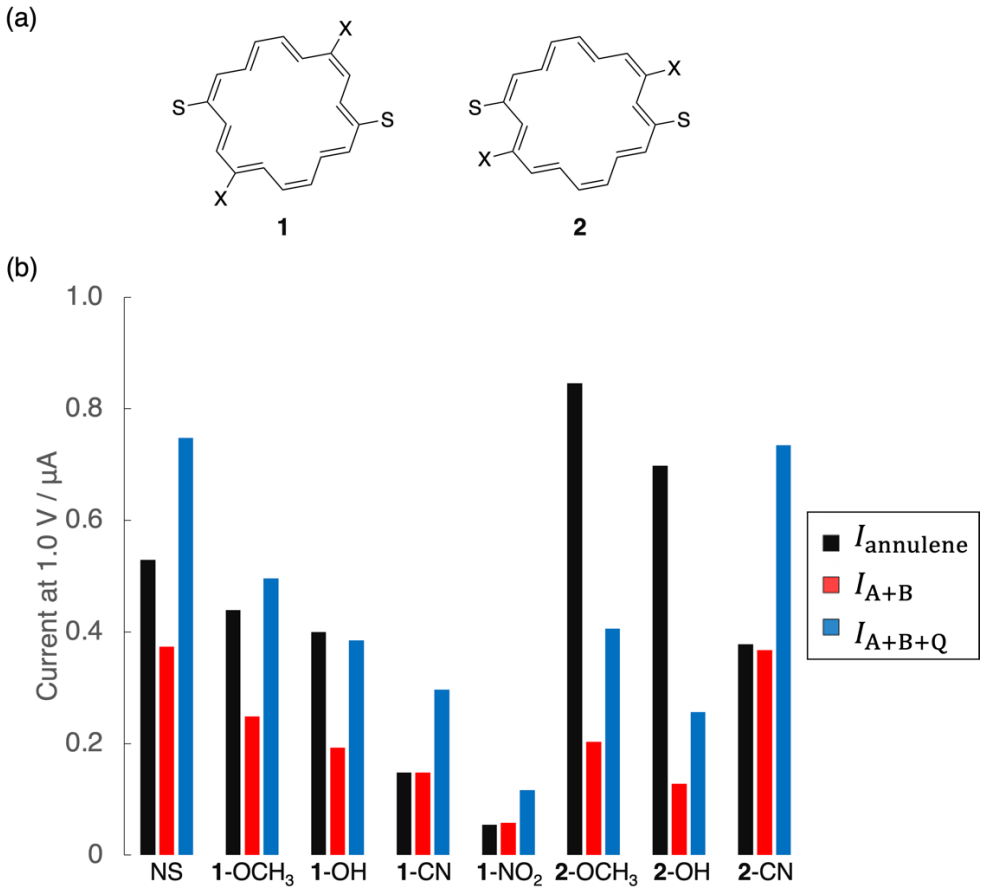

Fig. III.4. (a) Scheme of substituted model **1** (left) and **2** (right). (b) Calculated current of the [18]annulene derivatives and the divided polyenes at 1.0 V. The models **1** and **2** with substituents X are denoted as **1**-X and **2**-X, respectively.

To understand the effects of the substituents, the author examined the $\langle \hat{S}^2 \rangle$ values, as summarized in Table III.3. In the case of the NS form and its derivatives with electron-donating groups, the calculated $\langle \hat{S}^2 \rangle$ values are zero, indicating the closed-shell systems. However, their corresponding polyenes exhibit non-zero values, indicating the open-shell systems. In contrast, in the case of the electron-withdrawing groups, both the [18]annulene derivatives and their corresponding polyenes exhibit non-zero $\langle \hat{S}^2 \rangle$ values, indicating the open-shell electronic states. Therefore, the quantum interference effects in the molecular parallel circuits are related on the open-shell properties. When the quantum interference occurs between the two single-molecule components with the open-shell systems, the molecular parallel circuit exhibits the closed-shell electronic state. In contrast, the quantum interference does not occur between them, the molecular circuit retains the open-shell electronic state.

Table III.3. Total spin angular momentum $\langle \widehat{S}^2 \rangle$ of each extended molecule.

	$\langle \widehat{S}^2 \rangle$		
	[18]annulene	Polyene A	Polyene B
NS	0.000	0.147	0.147
1-OCH_3	0.000	0.163	0.163
1-OH	0.000	0.156	0.156
1-CN	0.462	0.222	0.222
1-NO_2	0.438	0.193	0.193
2-OCH_3	0.000	0.0162	0.0163
2-OH	0.000	0.0123	0.0123
2-CN	0.230	0.0406	0.0406

From Table III.3, the intensity of the $\langle \widehat{S}^2 \rangle$ values of the polyenes is not considered to be directly related to the quantum interference in the molecular parallel circuits. To further understand the electron conduction property of the molecular parallel circuit, the coupling constants $\gamma_{L1,\sigma}, \gamma_{MR,\sigma}$ and the total of site-overlaps of each orbital were analyzed, as summarized in Table III.4. As well as the case of the NS form, the [18]annulenes introduced electron-donating groups exhibit the symmetrical parameters between the α and β orbitals because of their closed-shell electronic states. On the other hand, in the molecules exhibiting the open-shell electronic structures, these parameters show the asymmetrical values between the α and β orbitals, indicating the spin polarization. As explained in Part II, the introduction of electron-donating groups weakens the spin polarization in single-molecule components, whereas the introducing electron-withdrawing groups enhances the spin polarization. Thus, the electron conduction properties of molecular parallel circuits composed of the open-shell single-molecule components can be explained that:

(i) When single-molecule components exhibit weak spin polarization, the quantum interference occurs between them, resulting in the molecular parallel circuit adopting the closed-shell electronic state. In this case, Ohm's law fails because of the quantum interference effects ($I_{\text{annulene}} \neq I_{\text{A+B}}$). Moreover, the existing conductivity equation in molecular parallel circuits, as shown in Equation (III.3), also does not hold ($I_{\text{annulene}} \neq I_{\text{A+B+Q}}$).

(ii) When the spin polarization in single-molecule components is strong, the quantum interference effect is suppressed, resulting in the molecular parallel circuit remaining in the open-shell electronic state. In this case, the current value of the molecular circuit is approximately equal to the simple sum of the current values of the single-molecule components, similar to Ohm's law in classical parallel circuits ($I_{\text{annulene}} \fallingdotseq I_{\text{A+B}}$).

Table III.4. Summary of the coupling constants and total of site-overlap of (a) **1**-OCH_3, (b) **1**-OH, (c) **1**-CN, (d) **1**-NO_2, (e) **2**-OCH_3, (f) **2**-OH and (g) **2**-CN models. The small differences in site-overlap between Polyenes A and B are considered to originate from the convergence accuracy of the molecular orbitals (here, 10^{-7} a.u. in electron density).

(a)	**1**-OCH_3					
	[18]annulene		Polyene A		Polyene B	
	α	β	α	β	α	β
$\gamma_{L1,\sigma}$ /eV	0.847	0.847	0.474	0.880	0.983	1.283
$\gamma_{MR,\sigma}$/eV	0.847	0.847	1.283	0.983	0.880	0.474
$\gamma_{L1,\sigma}{}^2 \times \gamma_{MR,\sigma}{}^2$ / eV^4	0.514	0.514	0.370	0.748	0.748	0.370
Site-overlap [(i)]	3.05	3.05	0.293	0.475	0.324	0.280
(b)	**1**-OH					
	[18]annulene		Polyene A		Polyene B	
	α	β	α	β	α	β
$\gamma_{L1,\sigma}$ /eV	0.832	0.832	0.448	0.828	1.287	1.001
$\gamma_{MR,\sigma}$/eV	0.832	0.832	1.287	1.001	0.448	0.828
$\gamma_{L1,\sigma}{}^2 \times \gamma_{MR,\sigma}{}^2$ / eV^4	0.479	0.479	0.333	0.687	0.333	0.687
Site-overlap [(i)]	3.07	3.07	0.174	0.386	0.204	0.288
(c)	**1**-CN					
	[18]annulene		Polyene A		Polyene B	
	α	β	α	β	α	β
$\gamma_{L1,\sigma}$ /eV	0.497	0.991	1.007	0.602	0.911	0.517
$\gamma_{MR,\sigma}$/eV	0.991	0.497	0.518	0.911	0.602	1.007
$\gamma_{L1,\sigma}{}^2 \times \gamma_{MR,\sigma}{}^2$ / eV^4	0.242	0.242	0.271	0.301	0.301	0.271
Site-overlap [(i)]	2.31	2.59	1.245	0.892	0.999	1.141
(d)	**1**-NO_2					
	[18]annulene		Polyene A		Polyene B	
	α	β	α	β	α	β
$\gamma_{L1,\sigma}$ /eV	0.890	0.481	1.070	0.632	0.710	0.441
$\gamma_{MR,\sigma}$/eV	0.481	0.890	0.441	0.711	0.632	1.070
$\gamma_{L1,\sigma}{}^2 \times \gamma_{MR,\sigma}{}^2$ / eV^4	0.183	0.183	0.222	0.201	0.201	0.222
Site-overlap [(i)]	1.04	0.896	0.380	0.523	0.558	0.296

(e)	**2**-OCH_3					
	[18]annulene		Polyene A		Polyene B	
	α	β	α	β	α	β
$\gamma_{L1,\sigma}$ /eV	0.859	0.859	1.074	1.219	0.620	0.527
$\gamma_{MR,\sigma}$/eV	0.859	0.859	0.620	0.527	1.074	1.219
${\gamma_{L1,\sigma}}^2 \times {\gamma_{MR,\sigma}}^2$ / eV^4	0.543	0.543	0.443	0.413	0.443	0.413
Site-overlap [(i)]	6.11	6.11	0.601	0.613	0.553	0.581
(f)	**2**-OH					
	[18]annulene		Polyene A		Polyene B	
	α	β	α	β	α	β
$\gamma_{L1,\sigma}$ /eV	0.861	0.861	1.084	1.198	0.523	0.609
$\gamma_{MR,\sigma}$/eV	0.861	0.861	0.609	0.523	1.198	1.084
${\gamma_{L1,\sigma}}^2 \times {\gamma_{MR,\sigma}}^2$ / eV^4	0.550	0.550	0.436	0.393	0.393	0.436
Site-overlap [(i)]	5.15	5.15	0.389	0.401	0.373	0.392
(g)	**2**-CN					
	[18]annulene		Polyene A		Polyene B	
	α	β	α	β	α	β
$\gamma_{L1,\sigma}$ /eV	0.622	0.955	0.584	0.767	0.871	0.997
$\gamma_{MR,\sigma}$/eV	0.955	0.622	0.997	0.871	0.767	0.584
${\gamma_{L1,\sigma}}^2 \times {\gamma_{MR,\sigma}}^2$ / eV^4	0.353	0.353	0.340	0.446	0.446	0.340
Site-overlap [(i)]	3.17	3.37	0.851	0.912	0.850	0.926

(i) Sum of HOMO−9 and LUMO+9.

Finally, the intensity of electron conductivity in annulenes is discussed. Fig. III.5 illustrates the product of the coupling constants, $\gamma_{L1,\sigma}^2 \gamma_{MR,\sigma}^2$, and the total site-overlaps for each orbital, in relation to the current values of the [18]annulene derivatives, separately for the α and β orbitals. From this figure, the electron conductivity of the [18]annulene derivatives exhibits positive correlations with the coupling constant and site-overlap. However, when comparing the model **1** and **2**, it is considered that the electron conductivity of the [18]annulene derivatives depends not only on the type of substituent but also on the substitution position. Therefore, the molecular orbitals were analyzed. Fig. III.6 illustrates the electron distributions in molecular orbitals that primarily contribute to electron conductivity, along with their site-overlap values and orbital energy levels. First, focusing on the model **1**, the total current of the annulene derivatives with the electron-withdrawing groups (**1**-CN and **1**-NO_2 shown in Fig. III.6 (d) and (e), respectively) decreases due to the spin polarization between the α and β orbitals. In contrast, a difference in the electron distributions in molecular orbitals, which contribute to the electron conductivity from the viewpoint of the site-overlap values, become important

for models with electron-donating groups. In the model **1**, **1**-OCH_3 and **1**-OH shown in Fig. III.6 (b) and (c), the introduction of the electron-donating groups suppresses a degree of delocalization of HOMO−4 and HOMO−5. This decrease is explained as follows: the π orbital energies of the annulene ring are shifted by the substitution effect, so that the energy difference between the π orbitals of the annulene ring and junction moieties becomes larger. As a result, the site-overlap values become small due to a decrease in conjugation between the ring and junction moieties. On the other hand, in the case of the model **2**, **2**-OCH_3, **2**-OH and **2**-CN shown in Fig. III.6 (f), (g) and (h), respectively, the π-orbitals of the annulenes, which are the primary contributors to electron conductivity, exhibit significant delocalization, leading to the large site-overlap value. Particularly, **2**-OCH_3 and **2**-OH do not exhibit spin-polarized distributions, indicating that they exhibit the larger site-overlap and higher electron conductivity compared to the NS form. These results indicate that the electron conductivity can be modulated based on the orbital distribution influenced by the substitution positions. This suggests that by strategically altering the substitution positions, it is possible to tailor the orbital interactions and, consequently, the electron conductivity of the annulene.

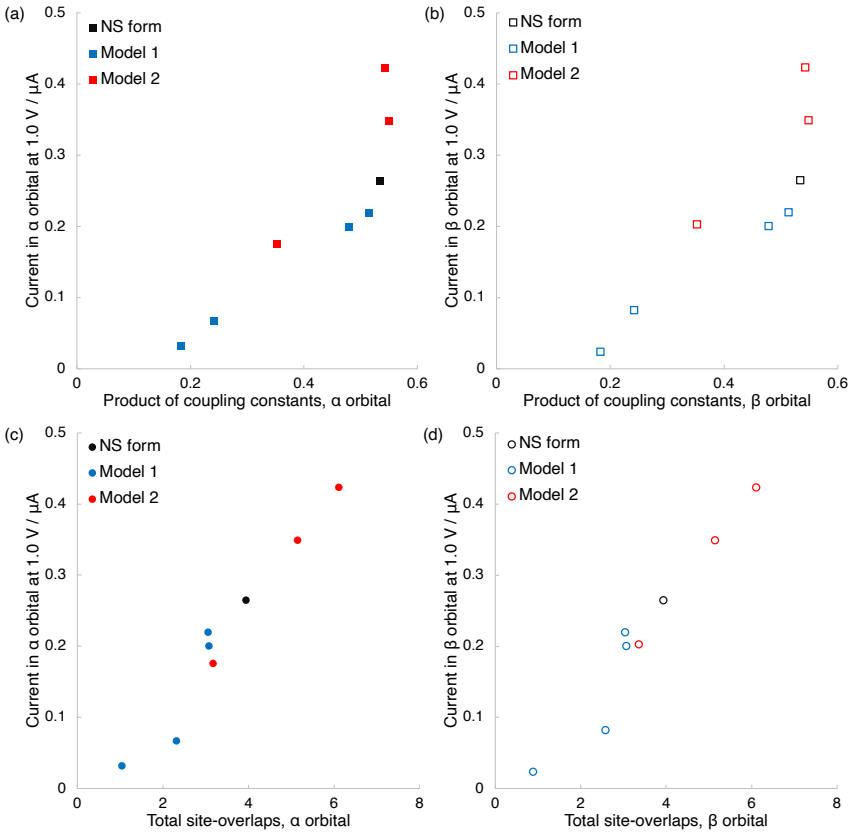

Fig. III.5. Current values at 1.0 V for the [18]annulene derivatives as a function of the product of the coupling constants, $\gamma_{L1,\sigma}^2\gamma_{MR,\sigma}^2$, in (a) α orbital and (b) β orbital, and as a function of the total site-overlaps for each orbital in (c) α orbital and (d) β orbital.

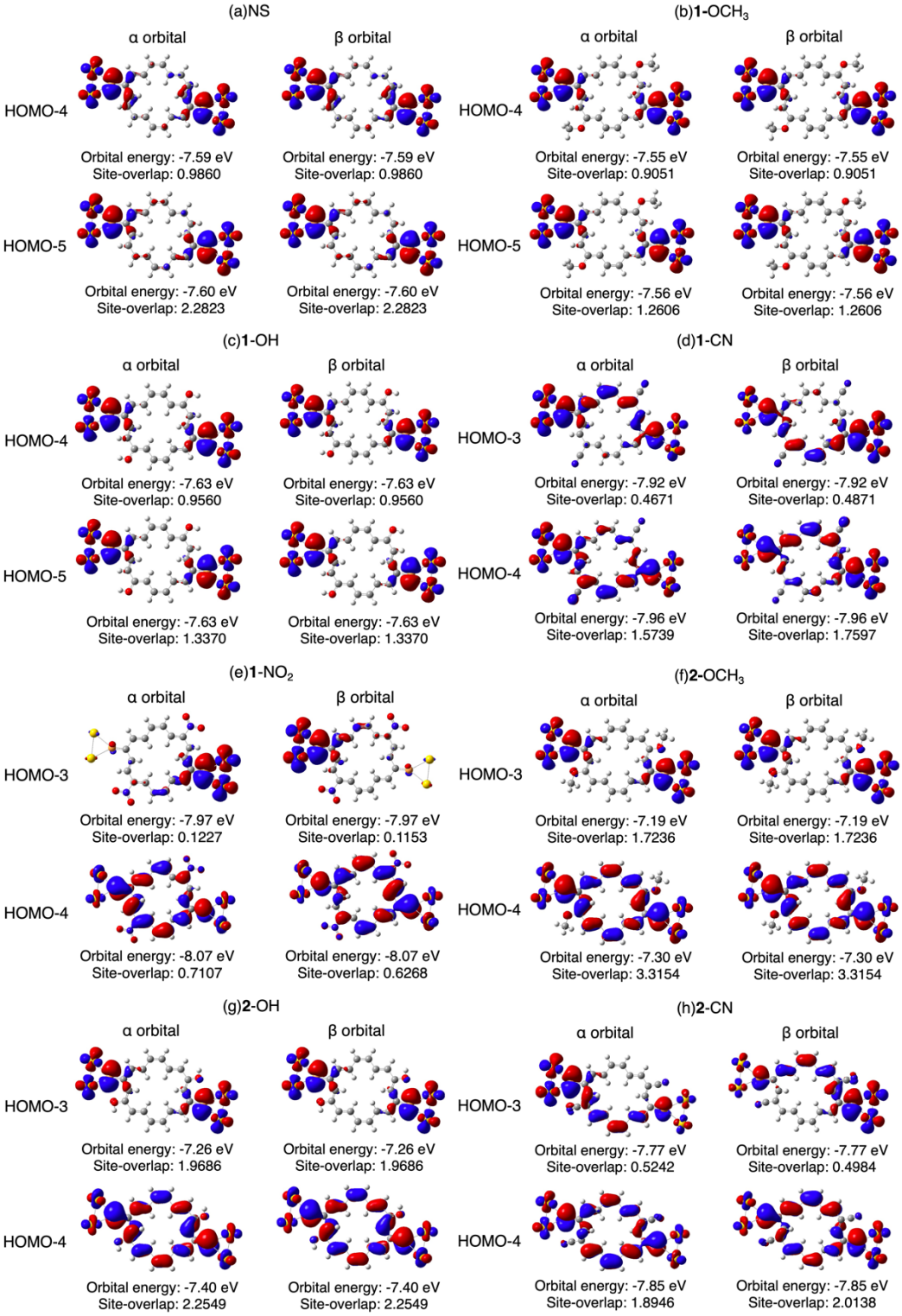

Fig. III.6. Electron distributions in contributed orbitals to electron conductivity of (a)NS, (b)**1**-OCH_3, (c)**1**-OH, (d)**1**-CN, (e)**1**-NO_2, (f)**2**-OCH_3, (g)**2**-OH and (h)**2**-CN models. Their isovalues are 0.02 electron/a.u.^{3}.

4. Conclusion

In this study, as the first step in the investigation of molecular integrated systems, the author examined the relationship between the electron conduction in single-molecule components with the open-shell electronic states and molecular parallel circuit composed of these components. As models for these investigation, the [18]annulene and its derivatives introduced the electron-donating/-withdrawing groups were examined as the molecular parallel circuit models composed of two linear polyenes. When the spin polarization of single-molecule components is small, such as in the NS form or electron-donating group derivatives, Ohm's law for classical parallel circuits does not hold due to the quantum interference effects in the molecular circuit. Additionally, in this case, the electronic structures of the molecular circuits, [18]annulenes, adopt a closed-shell systems. On the other hand, when the electron-withdrawing groups are introduced into the single-molecule components, the increased spin polarization suppresses the quantum interference between the components, allowing the molecular circuit to retain the open-shell electronic state. In this case, the current value of the molecular circuit becomes equal to the simple sum of the current values of the two components, similar to Ohm's law. Therefore, it is suggested that the quantum interference in molecular parallel circuits can be controlled by tuning the open-shell electronic state through substituent introductions.

References

1. X. Chen, M. Roemer, L. Yuan, W. Du, D. Thompson, E. del Barco, C. A. Nijhuis, *Nat. Nanotech.*, **2017**, *12*, 797.
2. G. D. Kong, H. Song, S. Yoon, H. Kang, R. Chang, H. J. Yoon, *Nano Lett.*, **2021**, *21*, 3162.
3. C. W. Fuller, P. S. Padayatti, H. Abderrahim, B. Merriman, et al., *Proc. Natl. Acad. Sci. U.S.A.*, **2022**, *119*, e2112812119.
4. Y. Hirano, Y. Segawa, T. Kawai, T. Matsumoto, *J. Phys. Chem. C*., **2013**, *117*, 140.
5. H. Tanaka, M. Akai-Kasaya, A. TermehYousefi, L. Hong, L. Fu, H. Tamukoh, D. Tanaka, T. Asai, T. Ogawa, *Nat. Commun.*, **2018**, *9*, 2693.
6. M. Magoga, C. Joachim, *Phys. Rev. B.*, **1999**, *59*, 16011.
7. H. Vazquez, R. Skouta, S. Schneebeil, M. Kamenetska, R. Breslow, L. Venkataraman, M. S. Hybertsen, *Nat. Nanotech.*, **2012**, *7*, 663.
8. K. Okazawa, Y. Tsuji, K. Yoshizawa, *J. Phys. Chem. C*., **2020**, *124*, 3322.
9. T. Sebechlebská, V. Kolivoška, J. Šebera, J. Fukal, D. Řeha, M. Buděšínský, I. Rosenberg, L. Bednárová, J. Gasior, G. Mészáros, M. Hromadová, V. Sychrovský, *J. Mater. Chem. C*., **2022**, *10*, 12022.
10. A. D. Becke, *J. Chem. Phys.,* **1993**, *98*, 1372.
11. W. J. Hehre, R. Ditchfield, J. A. Pople, *J. Chem. Phys.*, **1972**, *56*, 2257.
12. P. C. Hariharan, J. A. Pople, *Theoret. Chim. Acta,* **1973**, *28*, 213.

13. T. Clark, J. Chandrasekhar, G. W. Spitznagel, P. V. R. Schleyer, *J. Comput. Chem.*, **1983**, *4*, 294.
14. P. J. Hay, W. R. Wadt, *J. Chem. Phys*., **1985**, *82*, 299.
15. M. J. Frisch, G. W. Trucks, H. B. Schlegel, G. E. Scuseria, M. A. Robb, J. R. Cheeseman, G. Scalmani, V. Barone, B. Mennucci, G. A. Petersson, et al., Gaussian 09 Rev.D01; Gaussian Inc.: Wallingford, CT, USA, **2009**.
16. Y. Luo, C. -K. Wang, Y. Fu, *J. Chem. Phys*., **2002**, *117*, 10283.
17. L. -L. Lin, J. -C. Leng, X. -N. Song, Z. -L. Li, Y. Luo, C. -K. Wang, *J. Phys. Chem. C*., **2009**, *113*, 14474.

Part IV

Investigation of inter-molecular open-shell property and electrical conductivity in molecular integrated system

1.Introduction

To further expand molecular integrated systems, molecular crystals consisting of an infinite number of molecules were considered as model systems. Among these, particular attention was given to metal-organic frameworks (MOFs), which are porous crystals composed of metal ions/complexes and organic linkers [1]. MOFs stem from a combination of inorganic and organic moieties, and have design flexibility [2-4]. In 1995, Yaghi and Li synthesized a compound with unique channels and named it the metal-organic framework [5]. Kitagawa et al. reported that applying high pressure enables the adsorption of gas molecules into the pores of MOFs [6]. Subsequently, Yaghi and co-workers demonstrated that gas adsorption into MOFs is possible even under low temperature and low-pressure conditions, indicating that the pores of MOFs are permanent [7]. Furthermore, the proposal to use metal clusters, known as Secondary Building Units (SBUs), instead of metal ions as starting materials for synthesis has facilitated easier design [8]. Additionally, the establishment of solvothermal synthesis, which remains the predominant method, has enabled the production of robustly structured MOFs [9]. Today, various MOFs have been proposed with multifunctionality, including molecular storage, separation and catalysis due to their large surface areas and tunable pore sizes [10-12]. Furthermore, MOFs have been attracting attention for their properties in luminescence [13,14], electronics [15], and magnetism due to their ability to incorporate properties derived from metal complexes and organic linkers, as well as their high design flexibility through various combinations of these components. This makes them promising candidates for next-generation sensing materials, molecular devices, and data storage applications [17-20] (Fig. IV.1).

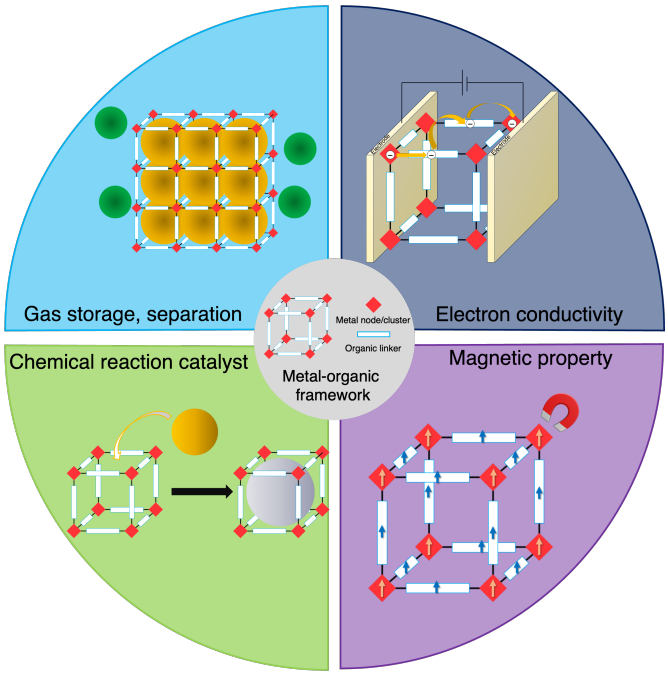

Fig. IV.1. Overview of the functionalities of MOFs.

The application of MOFs to electronic devices has garnered significant attention in recent years, and they are called MOF-based electronics or MOFtronics [15]. In general, the electron conductivity of MOFs is typically low due to their wide band gaps and the weak d-p orbital hybridization between metal ions and organic linkers. To synthesize electrically conductive MOFs, various strategies have been proposed: the main strategies include introducing redox-active molecules [21,22], polar solvent molecules [23], or conductive polymers [24,25] as guest molecules; incorporating mixed-valence complexes to induce polarity within the MOF [26]; and controlling π-π stacking interactions [27]. Furthermore, applications such as switching devices that modulate conductivity through external fields like electric fields or light [28,29], as well as diodes that control the direction of electron flow [30,31], have also been proposed. Additionally, MOFs exhibiting characteristics of memristors, which store the charge passed through them and change resistance in an analog manner [32], have garnered attention as potential hardware components for neuromorphic computing systems [33].

In this study, the author considered MOFs that incorporate single-molecule components with open-shell electronic states, similar to the paddlewheel-type dichromium complex in Part II. Therefore, Ru_2-TCNQ MOFs, composed of paddlewheel-type diruthenium complexes ([Ru_2] units) and tetracyano-*p*-quinodimethane derivatives (TCNQ linkers), were selected as models for the molecular integrated systems. In the Ru_2-TCNQ MOFs, the [Ru_2] units exhibit the open-shell electronic states due to their localized spins in π*- and δ*-orbitals as shown in Fig. IV.2. In addition, they can exhibit various charge transfer (CT) states. In Ru_2-TCNQ MOFs, the [Ru_2] unit is classified as an electron-donor (D), while the TCNQ linker acts an electron-acceptor (A) [34,35]. Therefore, multiple CT states can be considered: a neutral state (D^0-A^0-D^0), one-electron transferred states (D^+-A^--D^0 and D^0-A^--D^+, which are degenerate), and a two-electron transferred state (D^+-A^{2-}-D^+) [36-38]. Recently, some Ru_2-TCNQ MOFs have been reported to exhibit switchable magnetic properties triggered by gas absorption and desorption [39-42]. This characteristic arises from the charge transfer induced by gas molecule interactions, leading to the changing intrinsic spin states in the [Ru_2] units and TCNQ radicals, and it has been suggested that the potential application of the Ru_2-TCNQ MOFs in gas sensors and memory devices.

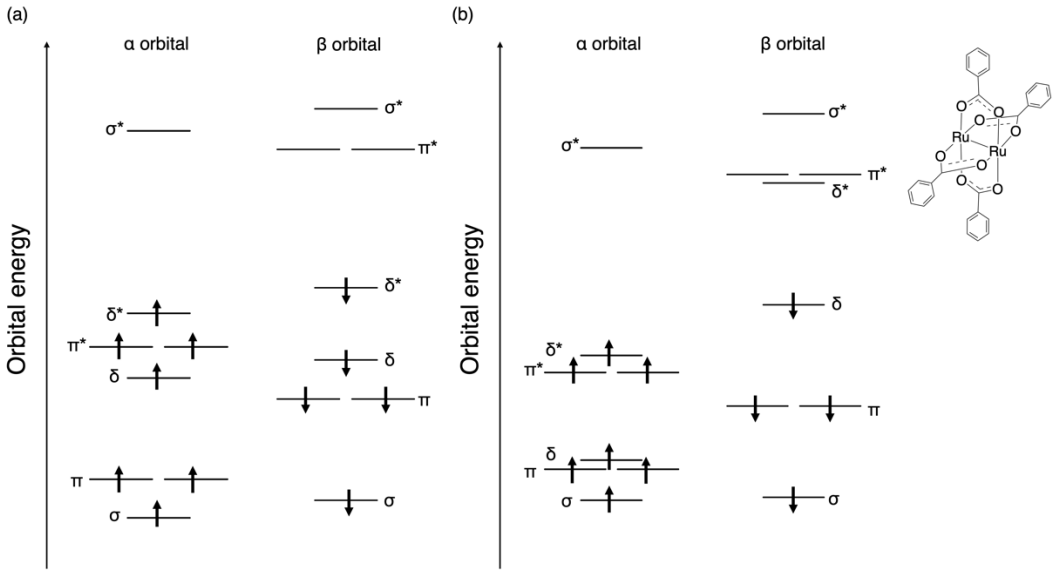

Fig. IV.2. Calculated molecular orbitals of paddlewheel-type diruthenium benzoate complex. Ru ions in the complex exhibit two CT states, i.e. (a) $[Ru_2^{II,II}]$ and (b) $[Ru_2^{II,III}]^+$. The electronic structures were calculated using DFT with the Broken-Symmetry (BS) method at B3LYP/LANL08f (Ru), 6-31G* (others) level of theory.

As described in Part I, Chapter 1, the electronic states of crystals can be determined using band calculations. However, handling localized spins is challenging with plane-wave basis sets. To address this issue, until now, the analysis of the electronic structures and magnetic properties of Ru_2-TCNQ MOFs has been conducted using DFT calculations with Gaussian basis (Gaussian DFT) [36, 39-41]. This approach utilizes a D_2-A unit cluster model, which is extracted from the X-ray structure of Ru_2-TCNQ MOF based on the stoichiometric ratio, consisting of two $[Ru_2]$ units and one TCNQ linker. The investigations using the D_2-A unit cluster models with Gaussian DFT have revealed the magnetism of Ru_2-TCNQ MOFs from the viewpoint of the molecular orbital interaction and inter-molecular magnetic interactions.

However, in the study of the molecular integrated systems, it is crucial to use a model that does not rely on structural extraction to elucidate its electronic states and magnetic interactions. In this case, investigations based on the band calculations with periodic boundary conditions are required. It has been proposed that the DFT calculations with open-shell systems under periodic conditions can be also calculated by using plane-wave basis sets (DFT/plane-wave) with hybrid exchange-correlation functionals or the on-site Coulomb parameter *U*. In Gaussian DFT calculations, the hybrid exchange-correlation functionals are often used for the open-shell electronic state calculations because they can predict spin-polarized electronic states with high accuracy [43-45]. However, the computational cost of hybrid-DFT is high for the band calculations using the plane-wave basis. Therefore, the DFT+*U* method [46-48], which uses the on-site Coulomb parameter *U* to obtain the spin-polarized electronic

structures, is employed in the DFT/plane-wave calculations because the computational costs of the DFT+*U* and pure-DFT methods are comparable [49-52]. Despite this, the Ru_2-TCNQ MOFs has not been considered using DFT+*U*/plane-wave methods. Therefore, there are no In the DFT+*U* method, the parameter *U* varies depending on the target system and must be determined through parameter fitting. However, the electronic structure calculations using the DFT+*U*/plane-wave method have not been performed for the Ru_2-TCNQ MOFs. Therefore, in the study of the molecular integrated systems based on the Ru_2-TCNQ MOFs, it is necessary to first determine the optimal *U* value.

In this study, as the models of the molecular integrated systems composed of single-molecule components with the open-shell electronic states, the author investigated the electronic structures and spin states of Ru_2-TCNQ MOFs using periodic systems with DFT+*U*/plane-wave method. For this calculations, the author first determined the on-site Coulomb parameter *U* in the periodic system calculations of the Ru_2-TCNQ MOFs. After determining the appropriate parameter, the author performed the band calculations using the DFT+*U*/plane-wave method to investigate the relationship between spin states and electron conductivity in the molecular integrated systems.

2. Computational Details

Fig. IV.3 shows the calculation models for the Gaussian DFT and DFT+*U*/plane-wave calculations. All models were constructed based on SCXRD data for $[\{Ru_2(o\text{-}ClPhCO_2)_4\}_2\{TCNQ(OMe)_2\}]$ (*o*-$ClPhCO_2^-$=ortho-chlorobenzoate; $TNCQ(OMe)_2$=2,5-dimethoxy-7,7,8,8-tetracyanoquinodimethane) [42]. Fig. IV.3(a) represents the D_2-A unit cluster model for the Gaussian DFT calculations, following the same as previous works. Fig. IV.3(b) shows the isolated system for the DFT+*U*/plane-wave calculations, with the same structure as the unit cluster model. Fig. IV.3(c) shows the periodic system for the DFT+*U*/plane-wave calculations without the structural extraction from the SCXRD data. The charge state is set to $[Ru_2^{II,III}]^+$-$TCNQ(OMe)_2^{2-}$-$[Ru_2^{II,III}]^+$ (D^+-A^{2-}-D^+) since the Ru_2-TCNQ MOF has been proposed to exhibit this charge state prior to CO_2 adsorption [42]. In the D^+-A^{2-}-D^+ charge state, two $[Ru_2^{II,III}]^+$ units magnetically interact, exhibiting both the anti-ferromagnetic interaction (AFM) state and the ferromagnetic interaction (FM) state, as shown in Fig. IV.4.

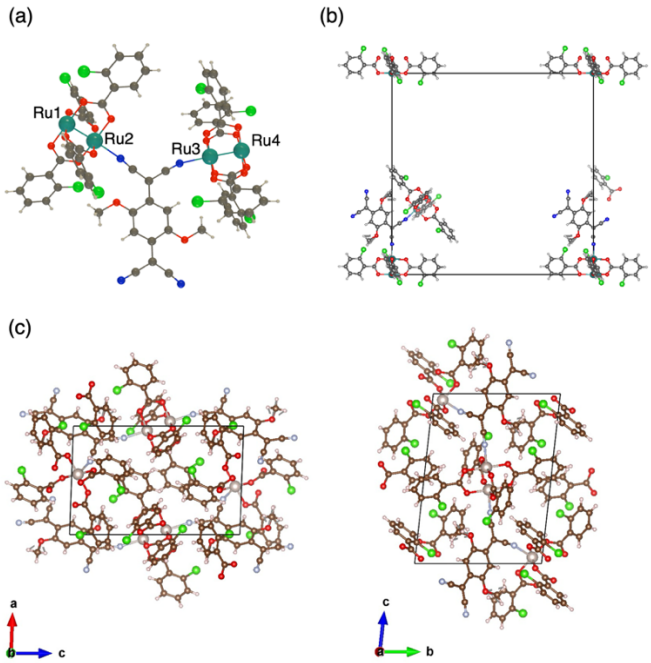

Fig. IV.3. The calculation models. (a) D_2-A unit cluster model for the Gaussian DFT calculations. (b)Isolated system and (c) periodic system along the ac-plane (left) and bc-plane (right) for the DFT+*U*/plane-wave calculations.

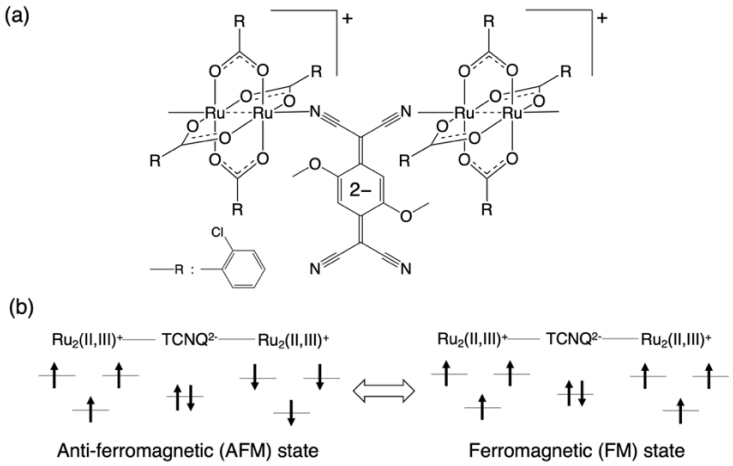

Fig. IV.4. (a) Illustration of the charge state of $[Ru_2^{II,III}]^+$-$TCNQ(OMe)_2^{2-}$-$[Ru_2^{II,III}]^+$ (D^+-A^{2-}-D^+), and (b) the spin states due to the magnetic interaction between two $[Ru_2]$ units, anti-ferromagnetic interaction (AFM) and ferromagnetic interaction (FM) states.

The Gaussian 09 [53] was used for the Gaussian DFT calculations. the hybrid DFT calculations were performed at PBE0 [54]/LANL08(f) (Ru) [55] and 6-31G* (others) [56,57] level of theory. The BS method was employed to handle the open-shell electronic staes. The total charge was set to neutral and the spin multiplicities of the AFM and FM states were singlet and septet, respectively.

For the DFT+*U*/plane-wave calculations, the Vienna Ab initio Simulation Package (VASP) [58-61] was performed at PBE functional [62]. The wavefunction was expanded using a plane-wave basis, and the cut-off energy was set to 400 eV. The PAW method was applied to the core region (see Part I, Chapter 1) [63,64]. The valence electrons for H, C, N, O, Cl, and Ru atoms were set to one ($1s^1$), four ($2s^22p^2$), five ($2s^22p^3$), six ($2s^22p^4$), seven ($3s^23p^5$) and eight ($5s^14d^7$), respectively. A supercell with a vacuum region was used for the isolated system calculations, with the specific cell size of 30.00 × 30.00 × 30.00 $Å^3$, and the Γ-point was sampled.

3. Results and Discussion

3.1 Fitting the on-site Coulomb parameter U in DFT+U/plane-wave calculations

To obtain appropriate *U* value for the Ru_2-TCNQ MOF, the author first determined the on-site Coulomb parameter *U*. From the perspective of the investigation for spin-polarized states, an approach was considered in which the spin densities of ruthenium ions in the band calculations were adjusted to match the spin densities of the Ru ions in the D_2-A unit cluster model obtained from the Gaussian DFT calculations. Therefore, the spin densities of Ru ions in AFM state in the isolated system, where the D_2-A unit cluster model was placed within the supercell, were calculated for *U* values ranging from 0.0 to 5.0 eV, as shown in Table IV.1. From Table IV.1, When *U* exceeds 3.5 eV, asymmetric spin densities between the two [Ru_2] units were obtained. The *U* adjusts the degree of the open-shell character, and as *U* increases, the open-shell nature becomes more pronounced. Thus, when *U* exceeds 3.5 eV, the open-shell character becomes too strong, leading to a different state from the considered D^+-A^{2-}-D^+ configuration. For further investigation of the parameter *U* determination, the author investigated parameter fitting using the effective exchange integral (*J* value) for *U* values ranging from 0.0 to 3.0 eV. The *J* values are useful for investigating the strength of the magnetic coupling [39-41,50-52]. To apply the Yamaguchi equation for the DFT/plane-wave calculations, the total spin angular momentum is expressed using the electron density as explained in Part I, Chapter 3. For this work, since the spin multiplicities of the AFM and FM states are singlet and septet, respectively, the Yamaguchi equation with the electron density is written as

$$J = \frac{E^{\mathrm{AFM}} - E^{\mathrm{FM}}}{12 + \int \rho_{\mathrm{AFM}}{}^{-}(r)dr - \int \rho_{\mathrm{FM}}{}^{-}(r)dr}, \qquad \text{(IV.1)}$$

where E_Y, $\rho_Y{}^{\alpha}(r)$ and $\rho_Y{}^{\beta}(r)$ are the total energy and the electron density of the major and minor spins for the spin states Y (Y: AFM or FM), respectively. Fig. IV. 5 indicates that the *J* values of the isolated system are too large in the range of *U* = 0.0 to 3.0 eV than that of the D_2-A unit cluster model calculated by Gaussian DFT. From the third-order polynomial approximation curve which was created from the *J* values for *U* ranging from 0.0 to 3.0 eV, estimating that the *U* value, which gives the same *J* value as the D_2-A unit cluster model, was approximately 3.5 eV. Therefore, in this work, *U* = 3.0 eV, where no asymmetricity of the spin densities between the [Ru_2] units was observed, and *U* = 3.5 eV,

predicted from the approximation curve, were adopted in the DFT+*U*/plane-wave method for the periodic systems.

Table IV.1. Spin densities of Ru ions in the isolated systems. The Ru numbers correspond to Fig. IV.3(a), and the column for Gaussian DFT represents the spin density of the D_2-A unit cluster model.

	Spin density					
U / eV	0.0	0.5	1.0	1.5	2.0	2.5
Ru1	1.15	1.17	1.17	1.22	1.25	1.30
Ru2	1.00	1.00	0.96	0.97	0.95	0.90
Ru3	−0.97	−0.96	−1.00	−0.93	−0.90	−0.85
Ru4	−1.13	−1.15	−1.20	−1.20	−1.23	−1.27
U / eV	3.0	3.5	4.0	4.5	5.0	Gaussian DFT
Ru1	1.37	1.37	1.27	1.26	1.25	1.27
Ru2	0.84	0.87	1.02	1.06	1.06	1.00
Ru3	−0.78	−0.66	−0.50	−0.35	−0.27	−0.96
Ru4	−1.34	−1.42	−1.52	−1.63	−1.74	−1.25

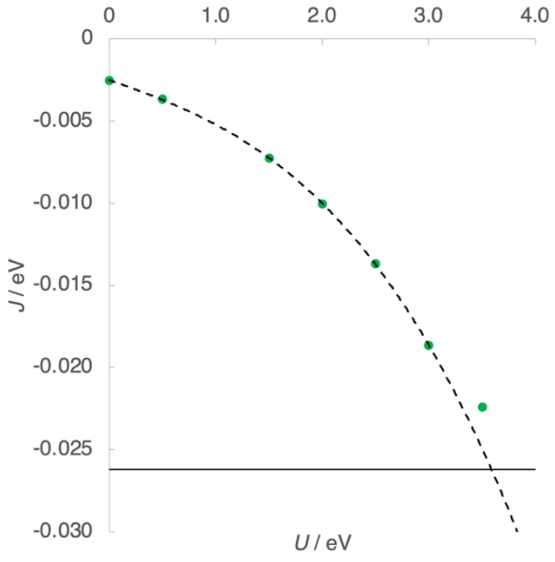

Fig. IV.5. *U* versus effective exchange integrals *J* values for *U* ranging from 0.0 to 3.5 eV. The black line represents the *J* value calculated by Gaussian DFT ($J = -0.0262$ eV). The black dashed curve represents the third-order polynomial approximation curve fitted for *U* values ranging from 0.0 to 3.0 eV, and the equation is $J = -0.00029U^3 - 0.00017U^2 - 0.00225U - 0.00250$ ($\boldsymbol{R}^2 = 0.99997$). *U*=3.5 eV deviates from the approximation curve due to the spin asymmetry.

3.2 Investigation of Electrical Conductivity Changes Induced by Magnetic Transition

First, the spin densities of Ru ions in the periodic system were compared for two U values, U = 3.0 eV and 3.5 eV, determined through the parameter fitting. The calculated spin densities are shown in Table IV.2. As shown in this table, the spin densities of the Ru ions were almost same between the two U values. In the isolated systems, it is considered that the asymmetricity appeared as U increases because the two [Ru_2] units receive the different potentials, resulting from the structural extraction and absence of surrounding components. Since such potential differences do not exist in the periodic systems, the results for U = 3.0 eV and 3.5 eV remained unchanged. Hereafter, the author discusses the results for U = 3.0 eV.

Table IV.2. Spin density of Ru ions for U = 3.0 and 3.5 eV in the periodic systems. The Ru numbers correspond to Fig. IV.3(a).

	Spin density			
	U = 3.0 eV		U = 3.5 eV	
	AFM	FM	AFM	FM
Ru1	1.23	1.29	1.24	1.30
Ru2	1.23	1.29	1.24	1.30
Ru3	−1.26	1.33	−1.27	1.34
Ru4	−1.26	1.33	−1.27	1.34

The electron conduction mechanism in MOFs are primarily categorized into two types: band conduction, where electrons propagate as waves delocalized across the crystal, and hopping conduction, where electrons are localized on individual molecules or atoms and propagate by intermittently hopping between them [15]. Therefore, to evaluate the potential for electron conductivity switching induced by the spin state transitions, similar to that of the single molecules as described in Part II, the author analyzed the band structures and spin density distributions of the periodic systems for each spin state. As an analysis of the band structures, density of state (DOS) plots are presented in Fig. IV.6. From the DOS analysis, changes in the band structure between the AFM and FM states were observed. However, they exhibit the multiple isolated peaks rather than continuous bands, suggesting that the band conduction is unlikely to occur in the Ru_2-TCNQ MOF.

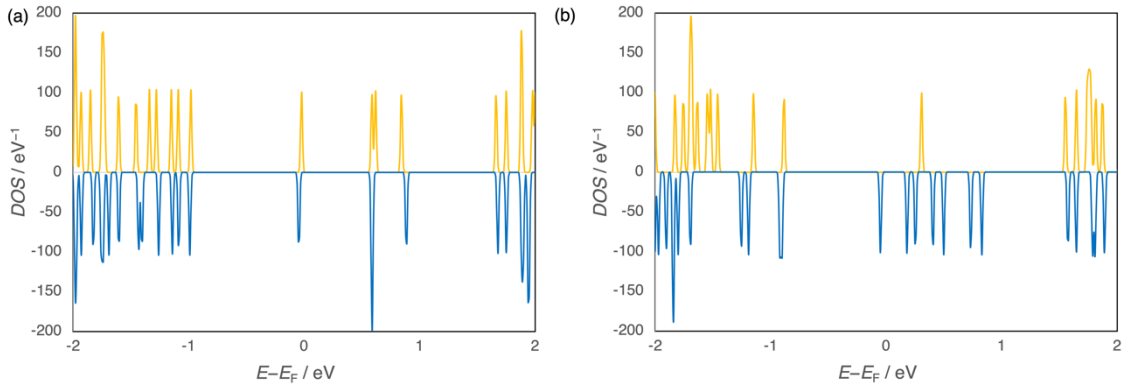

Fig. IV.6. DOS plots of the periodic systems in (a) the AFM and (b) FM states for $U = 3.0$ eV. The positive (yellow) and negative (blue) DOS values represent the major and minor spins, respectively.

As another analysis for the electron conduction in the Ru_2-TCNQ MOF, the partial spin density corresponding to each peak near the Fermi energy in DOS plots was calculated for each spin state. Fig. IV.7 and Fig. IV.8 show the partial spin density distribution for each DOS peak in the AFM and FM states, respectively. In the AFM state, the spin density was distributed only the [Ru_2] units in any DOS peaks. Consequently, even the hopping conduction does not occur in the AFM state because the localization of electrons at the [Ru_2] units. On the other hand, in the FM state, the spin density was distributed not only the [Ru_2] units but also the TCNQ linkers. Thus, the hopping conduction from the [Ru_2] units to the TCNQ linkers may be occurred in the FM state. As a result, the Ru_2-TCNQ MOF can be switched the electron conductivity by changing the spin states.

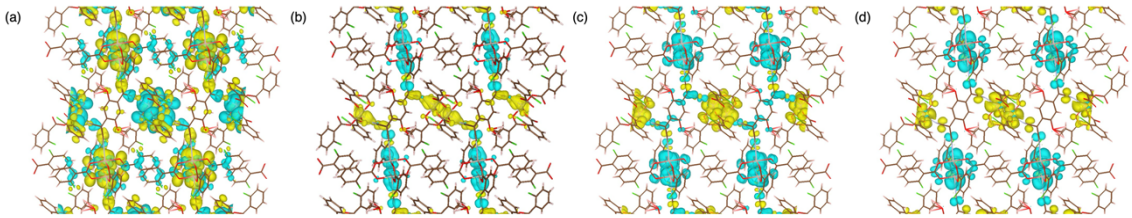

Fig. IV.7. Partial spin density distribution of the periodic system in the AFM state at (a) −1.5 to −1.0 eV, (b) −0.1 to 0.1 eV, (c) 0.4 to 0.7 eV and (d) 0.8 to 1.0 eV for $U = 3.0$ eV. The yellow and blue distributions represents positive and negative spin, respectively. All illustrations are viewed along the a-axis, and the threshold of the spin density distributions is 0.0005 e^- $Bohr^{-3}$.

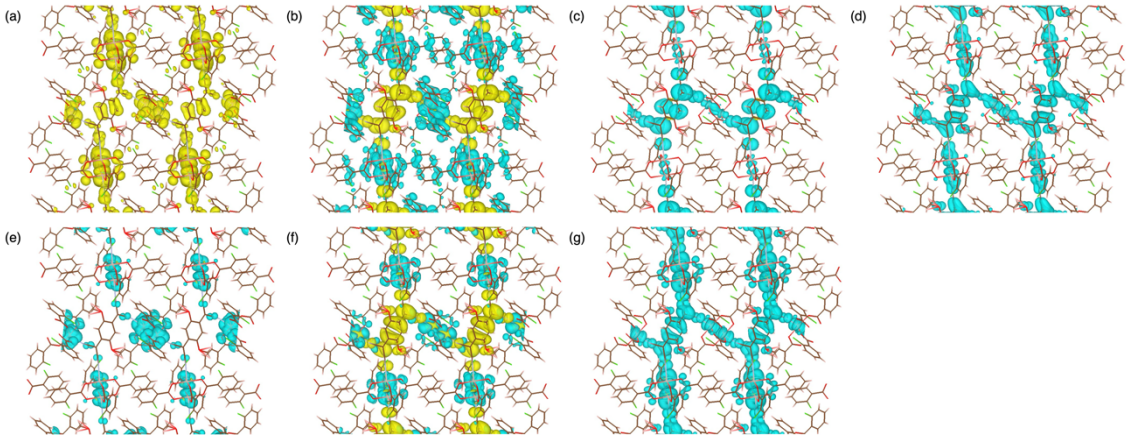

Fig. IV.8. Partial spin density distribution of the periodic system in the FM state at (a) −1.6 to −1.3 eV, (b) −1.3 to −1.1 eV, (c) −1.0 to −0.8 eV, (d) −0.1 to 0.1 eV, (e) 0.1 to 0.3 eV, (f) 0.3 to 0.5 eV and (g) 0.5 to 1.0 eV for U = 3.0 eV. The yellow and blue distributions represents positive and negative spin, respectively All illustrations are viewed along the a-axis, and the threshold of the spin density distributions is 0.0005 e^{-} $Bohr^{-3}$.

Fig. IV.9 presents the integrated partial spin density distribution within the range of $E-E_F$ = −1.0 to 0.5 eV, combining all the peaks near the Fermi energy shown in Fig. IV.7 and Fig. IV.8. From Fig. IV.9, the following insights can be drawn regarding functional design in molecular integrated systems:

AFM state: The spin distributions are localized at the [Ru_2] units. Therefore, the electronic states of each unit are independent, and unit-specific designs can be applied. That is, following the design guidelines for single-molecule components of paddlewheel-type complexes shown in Part II, it is possible to design the characteristics of the units within the molecular integrated systems.

FM state: The spin distributions are delocalized from the [Ru_2] units to the TCNQ linkers. This suggests that the wavefunctions of the [Ru_2] units overlap, including the TCNQ linkers, indicating the presence of quantum interference effect between the [Ru_2] units. Therefore, since the electronic states of each unit interfere with each other, new theories and design guidelines for molecular integrated systems are required.

The quantum interference effect in the FM state is essentially the same as that in the molecular parallel circuit discussed in Part III. That is, by introducing substituents into the [Ru_2] unit to enhance the spin polarization, the quantum interference can be suppressed, potentially allowing the system to be controlled into an independent state similar to the AFM state. Conversely, if substituents that weaken the spin polarization in the single-molecule components are introduced into the [Ru_2] units, the quantum interference effects may appear even in the AFM state, potentially making it impossible to design the system as independent units, as seen in the FM state. As described above, the

investigation of the electronic states of the Ru_2-TCNQ MOFs in the periodic systems has provided new insights into the electron conductivity and design principles of molecular integrated systems incorporating open-shell components.

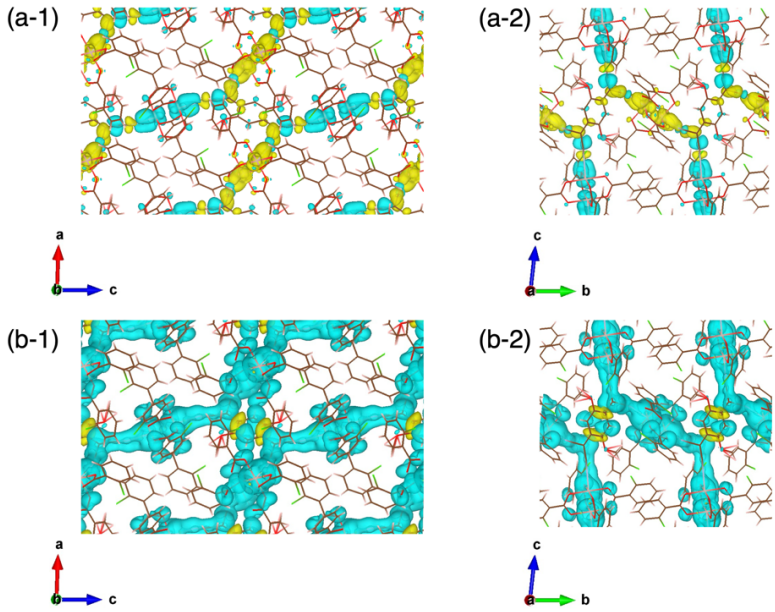

Fig. IV.9. Integrated partial spin density distribution of the periodic system in the AFM and FM states for U = 3.0 eV. The energy range $E-E_F$ is from −1.0 to 0.5 eV. (a-1) The AFM state along the ac-plane, (a-2) bc-plane, (b-1) the FM state along the ac-plane and (b-2) the bc-plane. The yellow and blue distributions represents positive and negative spin, respectively The threshold of the spin density distributions is 0.0005 e^- $Bohr^{-3}$.

4. Conclusion

In this study, the author investigated the electronic structures of the Ru_2-TCNQ MOFs as the model of molecular integrated systems. For this investigation, the determination of the on-site Coulomb parameter U in the DFT+U/plane-wave method for Ru_2-TCNQ MOF was conducted first. Using the determined U, the electronic structure calculations for the periodic system suggested that spin state transitions could also induce changes in the electron conductivity in the molecular integrated systems similar to the single-molecule components. Furthermore, the analysis of the partial spin density distribution revealed that in the AFM state, the spin distribution is localized on the [Ru_2] unit. This indicates that the design of individual units, i.e., single-molecule components, can also be applied to the design of the molecular integrated systems. On the other hand, in the FM state, the quantum interference between the [Ru_2] units leads to the spin distribution extending to the TCNQ linkers, suggesting the necessity of a design guideline specific to the molecular integrated systems.

From these results, it is suggested that in molecular integrated systems containing single-molecule

components with the open-shell electronic states, the electron conductivity can be switched through the spin states change induced by the magnetic interactions between open-shell units. On the other hand, it has been clarified that the electron transport properties and design guidelines differ significantly depending on the spin states. Therefore, further detailed investigations focusing on the design of molecular integrated systems are necessary in the future.

References

1. H. Furukawa, K. E. Cordova, M. O'Keeffe, O. M. Yaghi, *Science*, **2013**, *341*,1230444.
2. A. E. Baumann, D. A. Burns, B. Liu, V. S. Thoi, *Commun. Chem*., **2019**, *2*, 86.
3. V. F. Yusuf, N. I. Malek, S. K. Kailasa, *ACS Omega* **2022**, *7*, 44507.
4. M. Shahnawaz Khan, Y. Li, D.-S. Li, J. Qiu, X. Xu, H. Y. Yang, *Nanoscale Adv*., **2023**, *5*, 6318.
5. O. M. Yaghi, H. Li, *J. Am. Chem. Soc.*, **1995**, *117*, 10401.
6. M. Kondo, T. Yoshitomi, K. Seki, H. Matsuzaka, S. Kitagawa, *Angew. Chem. Int. Ed.*, **1997**, *36*, 1725.
7. H. Li, M. Eddaoudi, T. L. Groy, O. M. Yaghi, *J. Am. Chem. Soc.*, **1998**, *120*, 8571.
8. H. Li, M. Eddaoudi, M. O'Keeffe, O. M. Yaghi, *Nature*, **1999**, *402*, 276.
9. S. S. Chui, S. M.-F. Lo, J. P. H. Charmant, A. G. Orpen, I. D. Williams, *Science*, **1999**, *283*, 1148.
10. K. Adil, Y. Belmabkhout, R. S. Pillai, A. Cadiau, P. M. Bhatt, A. H. Assen, G. Maurin, M. Eddaoudi, *Chem. Soc. Rev.*, **2017**, *46*, 3402.
11. V. Pascanu, G. G. Miera, A. K. Inge, B. Martín-Matute, *J. Am. Chem. Soc.*, **2019**, *141*, 7223.
12. X. Zhang, R.-B. Lin, J. Wang, B. Wang, B. Liang, T. Yildirim, J. Zhang, W. Zhou, B. Chen, *Adv. Mater.*, **2020**, *32*, 1907995.
13. Y. Cui, Y. Yue, G. Qian, B. Chen, *Chem. Rev.*, **2012**, *112*, 1126.
14. R. Haldar, L. Heinke, C. Wöll, *Adv. Mater.*, **2020**, *32*, 1905227.
15. R. K. Parashar, P. Jash, M. Zharnikov, P. C. Mondal, *Angew. Chem. Int. Ed.*, **2024**, *63*, e202317413.
16. A. E. Thorarinsdottir, T. D. Harris, *Chem. Rev.*, **2020**, *120*, 8716.
17. P. Müller, F. M. Wisser, P. Freund, V. Bon, I. Senkovska, S. Kaskel, *Inorg. Chem.*, **2017**, *56*, 14164.
18. I. Stassen, N. Burtch, A. Talin, P. Falcaro, M. Allendorf, R. Ameloot, *Chem. Soc. Rev.*, **2017**, *46*, 3185.
19. G. M. Espallargas, E. Coronado, *Chem. Soc. Rev.*, **2018**, *47*, 533.
20. N. Kulachenkov, Q. Haar, S. Shipilovskikh, A. Yankin, J.-F. Pierson, A. Nominé, V. A. Milichko, *Adv. Funct. Mater.*, **2022**, *32*, 2107949.
21. A. A. Talin, A. Centrone, A. C. Ford, M. E. Foster, V. Stavila, P. Haney, R. A. Kinney, V. Szalai, F. El Gabaly, H. P. Yoon, F. Léonard, M. D. Allendorf, *Science,* **2014**, *343*, 66.

22. S. Gupta, H. Tanaka, T. Sato, S. Ye, B. K. Breedlove, H. Iguchi, S. Takaishi, *Inorg. Chem.*, **2022**, *61*, 4414.
23. L. Sun, C. H. Hendon, M. Dincă, *Dalton Trans.*, **2018**, *47*, 11739.
24. B. Dhara, S. S. Nagarkar, J. Kumar, V. Kumar, P. K. Jha, S. K. Ghosh, S. Nair, N. Ballav, *J. Phys. Chem. Lett.*, **2016**, *7*, 2945.
25. A. Jadhav, K. Gupta, P. Ninawe, N. Ballav, *Angew. Chem. Int. Ed.*, **2020**, *59*, 2215.
26. S. Takaishi, M. Hosoda, T. Kajiwara, H. Miyasaka, M. Yamashita, Y. Nakanishi, Y. Kitagawa, K. Yamaguchi, *Inorg. Chem.*, **2009**, *48*, 9048.
27. L. S. Xie, E. V. Alexandrov, G. Skorupskii, D. M. Proserpio, M. Dincă, *Chem. Sci.*, **2019**, *10*, 8558.
28. C. A. Fernandez, P. C. Martin, T. Schaef, M. E. Bowden, P. K. Thallapally, L. Dang, W. Xu, X. Chen, B. P. McGrail, *Sci. Rep.*, **2014**, *4*, 6114.
29. E. A. Dolgopolova, V. A. Galitskiy, C. R. Martin, H. N. Gregory, B. J. Yarbrough, A. M. Rice, A. A. Berseneva, O. A. Ejegbavwo, K. S. Stephenson, P. Kittikhunnatham, S. G. Karakalos, M. D. Smith, A. B. Greytak, S. Garashchuk, N. B. Shustova, *J. Am. Chem. Soc.*, **2019**, *141*, 13, 5350.
30. A. Prasoon, B. Dhara, D. Roy, S. Rana, S. Bhand, N. Ballav, *Chem. Sci.*, **2019**, *10*, 10040.
31. P. Sindhu, N. Ballav, *Inorg. Chem.*, **2023**, *62*, 10887.
32. L. O. Chua, *IEEE Trans. Circuit Theory,* **1971**, *18*, 507.
33. S. M. Yoon, S. C. Warren, B. A. Grzybowski, *Angew. Chem. Int. Ed.*, **2014**, *53*, 4437.
34. H. Miyasaka, *Acc. Chem. Res.*, **2013**, *46*, 2, 248.
35. H. Miyasaka, *Bull. Chem. Soc. Jpn.*, **2021**, *94*, 2929.
36. J. Zhang, W. Kosaka, Y. Kitagawa, H. Miyasaka, *Angew. Chem. Int. Ed.*, **2019**, *58*, 7351.
37. J. Zhang, W. Kosaka, H. Sato, H. Miyasaka, *J. Am. Chem. Soc.*, **2021**, *143*, 7021.
38. W. Kosaka, Z. Liu, J. Zhang, Y. Sato, A. Hori, R. Matsuda, S. Kitagawa, H. Miyasaka, *Nat. Commun.*, **2018**, *9*, 5420.
39. J. Zhang, W. Kosaka, Y. Kitagawa, H. Miyasaka, *Nat. Chem.*, **2021**, *13*, 191.
40. J. Zhang, W. Kosaka, Y. Kitagawa, H. Miyasaka, *Angew. Chem. Int. Ed.*, **2022**, *61*, e202115976.
41. J. Zhang, W. Kosaka, Q. Liu, N. Amamizu, Y. Kitagawa, H. Miyasaka, *J. Am. Chem. Soc.*, **2023**, *145*, 26179.
42. W. Kosaka, Y. Hiwatashi, N. Amamizu, Y. Kitagawa, J. Zhang, H. Miyasaka, *Angew. Chem. Int. Ed.*, **2023**, *62*, e202312205.
43. T. Soda, Y. Kitagawa, T. Onishi, Y. Takano, Y. Shigeta, H. Nagao, Y. Yoshioka, K. Yamaguchi, *Chem. Phys. Lett*., **2000**, *319*, 223.
44. Y. Kitagawa, T. Kawakami, Y. Yoshioka, K. Yamaguchi, *Polyhedron*, **2001**, *20*, 1189.
45. Y. Kitagawa, T. Soda, Y. Shigeta, S. Yamanaka, Y. Yoshioka, K. Yamaguchi, *Int. J. Quant. Chem.*, **2001**, *84*, 592.
46. V. I. Anisimov, J. Zaanen, O. K. Andersen, *Phys. Rev. B*, **1991**, *44*, 943.

47. V. I. Anisimov, F. Aryasetiawan, A. I. Lichtenstein, *J. Phys. Condens. Matter.*, **1997**, *9*, 767.
48. S. L. Dudarev,G. A. Botton, S. Y. Savrasov, C. J. Humphreys, A. P. Sutton, *Phys. Rev. B*, **1998**, *57*, 1505.
49. A. Urban, D.-H. Seo, G. Ceder, *npj Comput. Mater.*, **2016**, *2*, 16002.
50. K. Tada, S. Tanaka, T. Kawakami, Y. Kitagawa, M. Okumura, K. Yamaguchi, *Appl. Phys. Express*, **2019**, *12*, 115506.
51. K. Tada, Y. Kitagawa, T. Kawakami, M. Okumura, S. Tanaka, *Chem. Lett.*, **2021**, *50*, 392.
52. K. Tada, Y. Kitagawa, *Phys. Chem. Chem. Phys.*, **2023**, *25*, 32110.
53. M. J. Frisch, G. W. Trucks, H. B. Schlegel, G. E. Scuseria, M. A. Robb, J. R. Cheeseman, G. Scalmani, V. Barone, B. Mennucci, G. A. Petersson, et al., Gaussian 09 Rev.D01; Gaussian Inc.: Wallingford, CT, USA, **2009**.
54. C. Adamo, V. Barone, *J. Chem. Phys*., **1999**, *110*, 6158.
55. L. E. Roy, P. J. Hay, R. L. Martin, *J. Chem. Theory Comput.* **2008**, *4*, 1029.
56. W. J. Hehre, R. Ditchfield, J. A. Pople, *J. Chem. Phys.*, **1972**, *56*, 2257.
57. P. C. Hariharan, J. A. Pople, *Theoret. Chim. Acta*, **1973**, *28*, 213.
58. G. Kresse, J. Hafner, *Phys. Rev. B*, **1993**, *47*, 558.
59. G. Kresse, J. Hafner, *Phys. Rev. B*, **1994**, *49*, 14251.V
60. G. Kresse, J. Furthmuller, *Phys. Rev. B*, **1996**, *54*, 11169.
61. G. Kresse, J. Furthmuller, *Comput. Mater. Sci.*, **1996**, *6*, 15.
62. J. P. Perdew, K. Burke, M. Ernzerhof, *Phys. Rev. Lett.*, **1996**, *77*, 3865.
63. P. E. Blöchl, *Phys. Rev. B*, **1994**, *50*, 17953.
64. G. Kresse, D. Joubert, Joubert, *Phys. Rev. B*, **1999**, *59*, 1758.

General Conclusion

In this dissertation work, the author has investigated relationships between open-shell electronic states and electron conductivities of single molecules and their aggregates, such as molecular parallel circuit models and molecular crystal models, through simulations based on the quantum chemical theory and condensed matter physics theory. In Part II, the author has demonstrated relationships between spin states and electron conductivity in open-shell single molecules, aiming to establish design guidelines for single-molecule transistors. In Part III, the author has examined molecular parallel circuit models composed of two single-molecule components. By clarifying the relationship between structure, electronic states, and electron conductivity, the author has established guidelines for quantum interference control utilizing open-shell characters. In Part IV, as an investigation into aggregates of the single molecules, the author has focused on crystalline materials with periodic structures. Using first-principles band calculations, the author has clarified the relationship between spin states and electron conductivity, and have proposed a method for controlling electron conductivity through spin states. In the following, the author summarizes the results of each part.

Part II: Relationship between open-shell electronic state and single-molecule electron conductivity

In Part II, the relationship between the structure, spin states, and single-molecule electron conductivity of open-shell molecules was elucidated. Specifically, paddlewheel-type dichromium(II,II) benzoate complexes with various substituents on the bridging ligands were examined. By clarifying the relationship between spin states and electron conductivity, design guidelines for single-molecule transistors using spin state changes were proposed. Metal-metal bonds involving d-orbitals in these complexes exhibit a ground state of open-shell singlet (antiferromagnetic, AFM) that causes electrons to localize on each metal ion due to the quasi-degenerate of the frontier orbitals. However, it was revealed that introducing electron-donating/withdrawing substituents on the bridging ligands shortens/elongates the metal-metal distance that increases/decreases orbital overlap. As a result, the electron conductivity is controlled by the substituents. Furthermore, these metal complexes exhibit a ferromagnetic (FM) state as an excited state, where electron delocalization increases the electrical conductivity compared to the AFM state. In addition, it was found that the conductivity ratio between the AFM and FM states can also be controlled by the substituents. Through Part II, the author has clarified the relationship between the open-shell electronic state and the single-molecule electron conductivity of the paddlewheel-type dichromium(II) benzoate complex, and proposed the design guidelines for single-molecule transistors utilizing changes in single-molecule electron conductivity driven by switching the spin states in open-shell metal complexes.

Part III: Comparison of open-shell electronic state and electron conductivity in single molecule and two-molecule system

In Part III, the author has constructed a molecular parallel circuit model by considering a [18]annulene as two linear polyenes connected in parallel. And the author has successfully obtained fundamental insights into molecular circuits. Specifically, I have elucidated the effects of quantum interference within the circuit by investigating the relationship between the electronic states and electrical conductivity of [18]annulene with electron-donating/withdrawing substituents. In contrast to classical parallel circuits, where the total current equals the sum of the currents through individual components (i.e. Ohm's law), the molecular parallel circuit model is strongly affected by quantum interference that causes deviations from Ohm's law. It was shown that the current through the annulene circuit exceeds the sum of the currents through the two linear polyenes. Furthermore, the author has revealed that the introduction of electron-withdrawing substituents suppresses this quantum interference. Through Part III, the author has demonstrated that the quantum interference in the molecular parallel circuit models composed of the single-molecule components violates Ohm's law, and show unique current behaviors. In addition, introducing the substituents into the molecular circuits can control the quantum interference and tune circuit properties.

Part IV: Investigation of inter-molecular open-shell property and electrical conductivity in molecular integrated system

In Part IV, the author has focused on metal-organic frameworks (MOFs) as the aggregate of the single-molecule components and have elucidated the relationship between their electronic states and electron conductivity. Especially, the author has investigated the relationship between electronic structure and electron conductivity of the magnetic MOF composed of paddlewheel-type diruthenium complexes and TCNQ linkers by using density functional theory calculations with periodic boundary conditions (DFT+*U*/plane-wave method). In this system, the paddlewheel-type diruthenium units can exhibit the spin-polarized states, and there is the magnetic interaction between them. In the model complex, the AFM and FM states are the ground and excited states, respectively. From the spin density distributions near the Fermi level, the author found that the electrons are localized on the diruthenium complexes in the AFM state, whereas the electrons delocalize and spread to the TCNQ linkers in the FM state. This result demonstrated that the FM state shows higher electron conductivity. Consequently, it was shown that the electron conductivity can also be controlled by changes in the magnetic state in periodic systems, similar to the case of the single-molecules. In addition, these spin distributions suggested that the design of single-molecule components can be effective in the AFM state, whereas an alternative design approach incorporating the quantum interference effects may be necessary in the FM state. Through Part IV, the author has proposed that the electron conductivity can be achieved even in molecular crystalline materials with open-shell electronic structures by changing their spin

states, and provided fundamental insights into the design of functional materials for the realization of molecular devices.

In summary, the author has investigated the relationship between open-shell electronic states and electron conductivity, focusing on the single-molecule transistors, the molecular parallel circuits consisting of two molecules, and the periodic systems utilizing MOFs. As a result, the author has clarified the control of electron conductivity through spin states induced by open-shell electronic structures from single molecules to their aggregates. The findings in this dissertation are expected to contribute to the field of the molecular electronics by providing design guidelines for single-molecule components utilizing open-shell electronic states. Furthermore, they will offer theoretical insights and material design strategies for molecular devices leveraging open-shell electronic states, and pave the way for advancements in the development of functional molecular materials.

Future Prospects

This dissertation has investigated the relationship between open-shell electronic states, spin states and electron conductivities from single-molecule components to their aggregates. And then, this dissertation works clarified the utilization of open-shell properties in single-molecule transistors and provided guidelines for controlling open-shell properties in molecular circuits. Furthermore, it uncovered fundamental insights into electrical conductivity switching induced by spin-state changes in molecular crystals. On the other hand, there remain numerous issues to be addressed in molecular electronics and molecular devices, and attention must also be directed toward their realization and future trends. The major challenges can be outlined as below.

1. Molecular wiring

As discussed in Part II, treating single-molecule components as integrated circuits requires precise molecular wiring and connection techniques. Molecular wiring primarily employs two methods: arranging molecules on a substrate using self-assembled monolayers (SAMs) or connecting them between electrodes [1-4]. SAMs allow for large-scale and uniform arrangements; however, because they rely on molecular self-assembly, precise control over intermolecular distances and orientations remains challenging. In electrode connections, the characteristics of single molecules are more likely to be reflected. However, the instability of the molecule-electrode junction poses a significant challenge.

2. Integration and arrangement of single-molecule components

Similar to the challenges with wiring, the techniques for integration and arrangement are still in a developmental stage [4-8]. Currently proposed methods include patterning the substrate surface with lithography to selectively position molecules, adsorbing molecules onto templates like carbon nanotubes, floating molecules in a solution and transferring them onto a substrate (Langmuir-Blodgett (LB) films), coating the substrate with techniques such as drop casting or spin coating, and assembling molecular films layer-by-layer. All these methods rely on leveraging the characteristics of molecules, such as selective binding through chemical modification, chemical adsorption, or electrostatic interactions, to achieve integration and arrangement. Lithography allows for the regular arrangement of molecules, but it faces challenges such as the technological resolution limits inherent in lithographic techniques, similar to those encountered in semiconductors. Additionally, the complexity of the required techniques for single-molecule devices makes mass production difficult. Methods utilizing nanomaterial templates such as carbon nanotubes or graphene face challenges in application to molecules with low affinity for carbon-based materials. Techniques like Langmuir-Blodgett (LB) films,

drop casting, and spin coating offer simple manufacturing processes and enable relatively large-scale arrangements of materials; however, these methods are limited in terms of uniformity and the number of layers that can be achieved. Layer-by-layer integration offers the advantage of precise thickness control; however, scaling up this technique remains technically challenging. For the integration and arrangement of single-molecule devices, it is essential not only to advance each individual method but also to strategically combine techniques in a way that utilizes their strengths appropriately for specific applications.

3. External field control of single-molecule devices

To achieve the switching of electrical conductivity through spin state changes as discussed in Part II and Part IV, it is necessary to alter the spin state by applying an external field, such as optical, electric field, magnetic field, and so on [3,5]. Regarding single-molecule transistors, in principle, individual control of each molecule is required. However, considering the size of the apparatus needed to apply an external field and the range of its influence, achieving this presents significant technical challenges. On the other hand, for molecular devices, it is sufficient to classify characteristics based on the overall state of the molecule and control multiple states for proper functionality. For instance, as discussed in Part IV, the Ru_2-TCNQ MOF exhibits changes in overall magnetism upon gas adsorption. This property can be leveraged for applications such as memory devices or gas sensors [39,10].

4. Establishment of calculation method for electron conductivity of molecular device

Finally, from the perspective of theoretical calculations, establishing reliable methods for calculating electron transport is crucial. In addition to the ESGF method discussed in this thesis, other advanced computational approaches, such as the nonequilibrium Green's function (NEGF) method with periodic boundary conditions applied to electrodes, have been proposed. Moreover, there are multiple modes of electron conduction in single-molecule components and molecular integrated systems such as MOFs. For example, in single-molecule components, it has been revealed that tunneling conduction predominantly contributes in the short-chain length region, whereas hopping conduction becomes the main contribution as the chain length increases [11]. Additionally, as described in Part IV, MOFs can exhibit both band conduction, resulting from the delocalization of wavefunctions within the crystal, and hopping conduction between units [12]. If a theoretical framework is developed that adapts these different conduction mechanisms depending on the system's state, theoretical research on electron conduction in both single-molecule components and molecular integrated systems is expected to advance further. In fact, theoretical calculations have been proposed that enable the transition from the tunneling regime to the hopping regime in single-molecule conduction [13]. It is also necessary to propose a theoretical framework that enables the switching of

electrical conduction mechanisms in molecular integrated systems. In addition, it is desirable to establish a theoretical formulation for electrical conduction in molecular circuits that takes quantum interference into account. With the advancement of these theoretical computational methods, it is expected that simulations capable of evaluating the electron conduction properties of molecular devices will be established.

References

1. V. Burtman, A. S. Ndobe, Z. V. Vardeny, *J. Appl. Phys.*, **2005**, *98*, 034314.
2. Y. Okawa, S. K. Mandal, C. Hu, Y. Tateyama, S. Goedecker, S. Tsukamoto, T. Hasegawa, J. K. Gimzewski, M. Aono, *J. Am. Chem. Soc*., **2011**, *133*, 8227.
3. H, Song, M. A. Reed, T. Lee, *Adv. Mater.*, **2011**, *23*, 1583.
4. T. Li, V. K. Bandari, O. G. Schmidt, *Adv. Mater.*, **2023**, *35*, 2209088.
5. D. Xiang, X. Wang, C. Jia, T. Lee, X. Guo, *Chem. Rev.*, **2016**, *116*, 4318.
6. C. Engelbrekt, R. R. Nazmutdinov, S. Shermukhamedov, J. Ulstrup, T. T. Zinkicheva, X. Xiao, *Electrochem. Sci. Adv.*, **2022**, *2*, e2100157.
7. L. Chen, Z. Yang, Q. Lin, X. Li, J. Bai, W. Hong, *Langmuir*, **2024**, *40*, 1988.
8. K. Ariga, *Bull. Chem. Soc. Jpn.*, **2024**, *97*, uoad001.
9. J. Zhang, W. Kosaka, Y. Kitagawa, H. Miyasaka, *Nat. Chem.*, **2021**, *13*, 191.
10. J. Zhang, W. Kosaka, Q. Liu, N. Amamizu, Y. Kitagawa, H. Miyasaka, *J. Am. Chem. Soc.*, **2023**, *145*, 26179.
11. C. Joachim, M. A. Ratner, *Proc. Natl. Acad. Sci. USA*., **2005**, *102*, 8801.
12. R. K. Parashar, P. Jash, M. Zharnikov, P. C. Mondal, *Angew. Chem. Int. Ed.*, **2024**, *63*, e202317413.
13. L. -Y. Hsu, N. Wu, H. Rabitz, *J. Phys. Chem. Lett.*, **2014**, *5*, 1831.

List of Publications

Main Papers

[1] N. Amamizu, K. Sasaki, M. Nishida, K. Masuda, R. Inoue, K. Taka, K. Tada, R. Kishi, Y. Kitagawa, “Theoretical study on single-molecule electron conductivity of paddlewheel-type dichromium(II,II) tetraacetate complexes”, *Bull. Chem. Soc. Jpn.*, **2024**, *97*, uoae130 (9 pages).

[2] N. Amamizu, M. Nishida, K. Sasaki, R. Kishi, Y. Kitagawa, “Theoretical study on the open-shell electronic structure and electron conductivity of [18]annulene as a molecular parallel circuit model”, *Nanomaterials*, **2024**, *14*, 98 (14 pages).

[3] N. Amamizu, K. Tada, R. Kishi, W. Kosaka, H. Miyasaka, Y. Kitagawa, “Difference in spin structure of magnetic metal-organic frameworks between cluster model and periodic system”, *Chem. Lett.*, **2024**, *53*, upae230 (5 pages).

Related Papers

[1] Y. Miyazawa, Z. Wang, S. Hatano, R. Takagi, H. Matsuoka, N. Amamizu, Y. Kitagawa, E. Kayahara, S. Yamago, M. Abe, "Generation and Characterization of a Tetraradical Embedded in a Curved Cyclic Paraphenylene Unit", *Chem. Eur. J.*, **2023**, *29*, e202301009 (9 pages).

[2] W. Kosaka, Y. Hiwatashi, N. Amamizu, Y. Kitagawa, J. Zhang, H. Miyasaka, "Densely Packed CO2 Aids Charge, Spin, and Lattice Ordering Partially Fluctuated in a Porous Metal-Organic Framework Magnet", *Angew. Chem. Int. Ed.*, **2023**, *62*, e202312205 (7 pages).

[3] J. Zhang, W. Kosaka, Q. Liu, N. Amamizu, Y. Kitagawa, H. Miyasaka, "CO2-Sensitive Porous Magnet: Antiferromagnet Creation from a Paramagnetic Charge-Transfer Layered Metal-Organic Framework", *J. Am. Chem. Soc.* **2023**, *145*, 26179-26189.

Presentations at International Conference

[1] N. Amamizu, H. Sato, K. Cho, Y. Kitagawa, M. Nakano, "Theoretical study on the difference in single-molecule electron conductivity of paddlewheel-type binuclear Cr(II) complexes between antiferromagnetic and ferromagnetic states", 17th International Conference on Molecule Based Magnets (ICMM), Online, June 14-18, 2021. (**Poster**)

[2] N. Amamizu, H. Sato, K. Cho, Y. Kitagawa, M. Nakano, "Theoretical study on electron conductivity of cyclic π-conjugated systems for molecular circuit design", 8th International Chemical Congress of Pacific Basin Societies (Pacifichem), Online, December 16-21, 2021. (**Poster**)

[3] N. Amamizu, K. Sasaki, K. Cho, T. Kamimura, K. Tokuyama, Y. Hayashi, M. Tsuda, M. Nakano, R. Kishi, Y. Kitagawa, "Theoretical Study on Single-Molecule Electron Conductivity of Annulene as Molecular Parallel Circuit Models", 25th IUPAC Conference on Physical Organic Chemistry

(ICPOC25), Hiroshima, Japan, July 10–15, 2022. **(Poster)**

[4] N. Amamizu, K. Sasaki, K. Cho, T. Kamimura, K. Tokuyama, Y. Hayashi, M. Tsuda, R. Kishi, M. Nakano, Y. Kitagawa, "Theoretical Study on Electron Conductivity of Paddle-Wheel Type Binuclear Complexes for Design Guideline of Single-Molecule Transistors", 8th Asian Conference on Coordination Chemistry(ACCC8), Online, August 7-11, 2022. (**Poster**)

[5] N. Amamizu, K. Sasaki, K. Cho, T. Kamimura, K. Tokuyama, Y. Hayashi, M. Tsuda, R. Kishi, Y. Kitagawa, "Theoretical design for single-molecule transistors based on electron conductivity of paddle-wheel type binuclear complexes in two spin states", The 73rd Yamada Conference & IMR International Symposium, Sendai, Japan, October 8-11, 2022. (**Poster**)

[6] N. Amamizu, M. Nishida, K. Sasaki, R. Kishi, Y. Kitagawa, "Theoretical study on electronic structure and electron conductivity of annulene as molecular parallel circuit models", The 5th conference of Theory and Applications of Computational Chemistry(TACC2023), Sapporo, Japan, September 4-9, 2023. (**Poster**)

[7] N. Amamizu, M. Nishida, K. Sasaki, R. Kishi, Y. Kitagawa, "Theoretical study on design guideline for single-molecule electronics based on d-π conjugated compounds", The 1st bilateral symposium of scientific exchange between OU and NTUT, Taipei, Taiwan, November 3, 2023. (**Oral**)

[8] N. Amamizu, K. Tada, R. Kishi, W. Kosaka, H. Miyasaka, Y. Kitagawa, "Difference in Spin Structure of Metal-Organic Frameworks between Cluster Model and Periodic System", The 8th Japan-Czech-Slovakia (JCS) International Symposium on Theoretical Chemistry, Sapporo, Japan, June 17-21, 2024. (**Poster**)

[9] N. Amamizu, K. Tada, R. Kishi, W. Kosaka, H. Miyasaka, Y. Kitagawa, "Theoretical study on relationship between inter-molecular magnetic exchange interaction and local molecular structure in metal-organic frameworks", 3rd Asian Conference on Molecular Magnetism (ACMMIII), Busan, Republic of Korea, September 1-4, 2024. (**Poster**)

Acknowledgement

This dissertation study was carried out under the supervision of Prof. Dr. Masayoshi Nakano, , Prof. Dr. Norikazu Nishiyama, and Prof. Dr. Yasutaka Kitagawa at Division of Chemical Engineering, Department of Materials Engineering Science, Graduate School of Engineering Science, Osaka University. I am profoundly thankful to Prof. Dr. Nakano not only for providing fundamental insights into quantum chemistry but also for offering research advice from perspectives different from my own. Although I belongs to a different laboratory, Prof. Dr. Nishiyama has provided tremendous support, for which I am truly grateful. And, I am sincerely thankful to Prof. Dr. Kitagawa for his exceptional guidance and support during the course of this dissertation works. His continuous advice and readiness to listen to my concerns have been invaluable, providing me with great confidence in pursuing this study.

I am deeply grateful to Prof. Dr. Nobuyuki Matubayasi, Prof. Dr. Tomoo Mizugaki, Prof. Dr. Yasutaka Kitagawa (Graduate School of Engineering Science, Osaka University) and Prof. Dr. Mitsutaka Okumura (Graduate School of Science, Osaka University) for kindly accepting the referee of this dissertation.

I would like to express gratitude to Dr. Ryohei Kishi and Dr. Kohei Tada (Graduate School of Engineering Science, Osaka University) for their insightful comments on my study and for the instructions of quantum chemistry and condensed matter physics. I would like to express my sincere gratitude to Prof. Dr. Hitoshi Miyasaka and Dr. Wataru Kosaka (Institute for Materials Research, Tohoku University) for their invaluable advice and insights regarding the research on Ru_2-TCNQ MOF. I am also deeply thankful for their dedicated support and contributions to the studies presented in Part IV.

I am deeply grateful to Prof. Manabu Abe (Department of Chemistry, Hiroshima University) for allowing me to contribute to the research on fascinating tetraradical molecules through theoretical calculations. I sincerely appreciate the valuable insights and inspiration regarding open-shell systems that I have gained through this collaboration. I would like to express my heartfelt gratitude to Prof. Dr. Mitsutaka Okumura (Graduate School of Science, Osaka University) for serving as a mentor and providing invaluable advice during our discussions on research. Your guidance has been an incredibly valuable experience, greatly aiding me in advancing my work.

I would like to thank all the members I have met in Kitagawa lab. (old Nakano lab.) for sharing the wonderful days during 2019-2025. I was happy to witness their achievements and to discuss a lot of things day and night. Dr. Takanori Nagami, Dr. Takayoshi Tonami, Dr. Wataru Yoshida and Mr. Kenji Okada have inspired me a lot because of their outstanding abilities and deep insights on study etc. Especially, I would like to express my sincere gratitude to Dr. Takayoshi Tonami for his invaluable

advice and guidance on this research.

This dissertation stud was financially supported by JST, the establishment of university fellowships towards the creation of science technology innovation, Grant Number JPMJFS2125.

Finally, I would like to thank my family, Hiroshi, Ritsue, Tomoya, Choco, Kinako and Koume for their kind supports and encouragements.

Naoka Amamizu

March 2025